AFTERGLOW LIGHT CURVES OF THE NON-RELATIVISTIC EJECTA MASS
IN A STRATIFIED CIRCUMSTELLAR MEDIUM

N. Fraija[1†], B. Betancourt Kamenetskaia[1,2,3], M.G. Dainotti[4,5,6], R. Barniol Duran[7], A. Gálvan Gámez[1],
S. Dichiara[8,9] and Pedreira, A. C. Caligula do E. S.[1]

[1]Instituto de Astronomía, Universidad Nacional Autónoma de México, Circuito Exterior, C.U., A. Postal 70-264, 04510 México City, México
[2]LMU Physics Department, Ludwig Maxmillians University,Theresienstr. 37, 80333 Munich, Germany
[3]TUM Physics Department, Technical University of Munich, James-Franck-Str, 85748 Garching, Germany
[4]Physics Department, Stanford University, 382 Via Pueblo Mall, Stanford, USA
[5]Space Science Institute, Boulder, Colorado
[6]Obserwatorium Astronomiczne, Uniwersytet Jagielloński, ul. Orla 171, 31-501 Kraków, Poland.
[7]Department of Physics and Astronomy, California State University, Sacramento, 6000 J Street, Sacramento, CA 95819-6041, USA
[8] Department of Astronomy, University of Maryland, College Park, MD 20742-4111, USA and
[9] Astrophysics Science Division, NASA Goddard Space Flight Center, 8800 Greenbelt Rd, Greenbelt, MD 20771, USA
Draft version November 18, 2020

ABSTRACT

We present the afterglow light curves produced by the deceleration of the non-relativistic ejecta mass in a stratified circumstellar medium with a density profile $n(r) \propto r^{-k}$ with $k = 0$, 1, 1.5, 2 and 2.5. Once the ejecta mass is launched with equivalent kinetic energy parametrized by $E(>\beta) \propto \beta^{-\alpha}$ (where beta is the ejecta velocity) and propagates into the surrounding circumstellar medium, it first moves with constant velocity (the free-coasting phase), and later it decelerates (the Sedov-Taylor expansion). We present the predicted synchrotron and synchrotron-self Compton light curves during the free-coasting phase, and the subsequent Sedov-Taylor expansion. In particular cases, we show the corresponding light curves generated by the deceleration of several ejecta masses with different velocities launched during the coalescence of binary compact objects and the core-collapse of dying massive stars which will contribute at distinct timescales, frequencies, and intensities. We find that before the radiation escapes from the kilonova (KN) and produces a peak in the light curve, the KN afterglow ejecta is very weak and the corresponding ejecta velocity moves as $\propto t^{-\frac{2}{\alpha+1}}$. Finally, using the multi-wavelength observations and upper limits collected by a large campaign of orbiting satellites and ground telescopes, we constrain the parameter space of both the KN afterglow in GW170817 and the possibly generated KN afterglow in S190814bv. Further observations on timescales of years post-merger are needed to derive tighter constraints.

Subject headings: Gravitational waves - merger: black holes, neutron stars — Physical data and processes: radiation mechanism: nonthermal — ISM: general — Gamma-rays bursts: individual (GRB 170817A)

1. INTRODUCTION

Long-duration gamma-ray bursts (lGRBs; $T_{90} \gtrsim 2$ s; Kouveliotou et al. 1993) are connected with the core-collapse (CC) of dying massive stars (Woosley 1993; Galama et al. 1998) that lead to supernovae (SNe; Bloom et al. 1999; Woosley and Bloom 2006). Short-duration GRBs (sGRBs; $T_{90} \lesssim 2$ s) are associated with the coalescence of binary compact objects (NS-NS or BH-NS)[1] that lead to kilonovae[2] (KNe; Li and Paczyński 1998; Rosswog 2005; Metzger et al. 2010; Kasen et al. 2013; Metzger 2017). The dying massive stars and the coalescence of binary compact objects are believed to launch considerable amounts of materials with broad ranges of velocities. In the framework of the coalescence of NS-NS mergers, non-relativistic ejecta masses with velocities in the range $0.03 \lesssim \beta \lesssim 0.8$ (expressed, hereafter, in units of the speed of light) such as the dynamical ejecta, the cocoon material, the shock breakout material and the wind ejecta are launched (e.g., see Dessart et al. 2009; Metzger and Fernández 2014; Fernández et al.

2015; Kyutoku et al. 2014; Metzger et al. 2015; Nagakura et al. 2014; Murguia-Berthier et al. 2014; Lazzati et al. 2017, 2018; Goriely et al. 2011; Hotokezaka et al. 2013; Bauswein et al. 2013; Wanajo et al. 2014). In the framework of CC-SNe (depending on the type of SN association), several ejecta masses with non-relativistic velocities less than $\beta \lesssim 0.3$ have been reported (e.g., see Modjaz et al. 2020; Izzo et al. 2020; Nicholl et al. 2020; Izzo et al. 2019; Gal-Yam 2017; Valenti et al. 2008; Kulkarni et al. 1998; Bloom et al. 1999; Woosley and Bloom 2006). While the inferred mass of the ejecta for the first GRB/SN association (GRB 980425/SN1998bw; Kulkarni et al. 1998) was $10^{-5} M_\odot$ with a velocity of $\beta \sim 0.2 - 0.3$, the inferred mass for the first GRB/KN association (GRB 170817A/AT2017gfo; Coulter et al. 2017) was $10^{-4} - 10^{-2} M_\odot$, ejected with a velocity of $\beta \sim 0.1 - 0.3$ (Arcavi et al. 2017; Cowperthwaite et al. 2017; Nicholl et al. 2017; Metzger 2019).
Chevalier (1982) studied the interaction of an adiabatic flow in a circumstellar density profile for type II SNe of the form $n(r) \propto r^{-2}$. Such a power law has since been the usual convention and it has been used in following papers for different types of SNe, such as those by Kotak et al. (2004), Chevalier (1984), Soderberg et al. (2006) and Blondin et al. (1996), amongst others. Nevertheless, in a more recent study, Moriya

---

[1] NS corresponds to neutron star and BH to black hole.
[2] A fairly isotropic thermal transient powered by the radioactive decay of rapid neutron capture process nuclei and isotopes

and Tominaga (2012) showed that the spectral diversity of type II luminous SNe may be explained by the diversity in the density slope of the surrounding dense wind. To this effect, they proposed a wind density structure with a profile $\propto r^{-k}$ and noticed that the ratio of the diffusion timescale in the optically thick region of the wind and the shock propagation timescale after the shock breakout have a strong dependence on the stratification parameter k which led to differences in the SN spectral evolution.

The interaction of the ejecta mass with the surrounding circumburst medium in the non-relativistic regime has been proposed to describe the multi-wavelength afterglow observations in timescales from days to several years (e.g., see Wijers et al. 1997; Dai and Lu 1999; Huang et al. 1999; Livio and Waxman 2000; Huang and Cheng 2003; Sironi and Giannios 2013; Barniol Duran and Giannios 2015). Several authors, (e.g see Metzger and Bower 2014; Fong et al. 2016; Liu et al. 2020; Schroeder et al. 2020), considered the material launched during the coalescence of binary compact objects and computed the synchrotron emission in the radio bands. The authors assumed a free-coasting phase, and the subsequent Sedov-Taylor expansion. Tan et al. (2001) considered that the kinetic energy of the shock wave could be described in terms of a power-law (PL) velocity distribution. Henceforth, several authors have considered that the material launched during the coalescence of binary compact objects and the CC-SNe may be described by a PL velocity distribution (e.g., see Bauswein et al. 2013; Kyutoku et al. 2014; Hotokezaka and Piran 2015; Barniol Duran et al. 2015; Metzger 2017; Mooley et al. 2018b; Fraija et al. 2019e; Kathirgamaraju et al. 2019; Metzger 2019; Lazzati et al. 2012; Horesh et al. 2013; Margutti et al. 2013, 2014). In the context of the coalescence of a NS binary, for instance, Fraija et al. (2019e) and Kathirgamaraju et al. (2019) assumed a PL distribution for the energy of the shock breakout (the outermost matter) and the kilonova material in GW170817, and calculated the non-thermal emission generated by the interaction of these materials with the uniform-density medium. In the case of dying massive stars, for example, Lazzati et al. (2012) presented a set of numerical simulations of stellar explosions induced by outflows and compared the results with observational properties of type Ibc SNe as a function of the equivalent kinetic energy and velocity of the ejecta.

In this paper, we present, based on analytic arguments, a theoretical model that predicts the multi-wavelength afterglow emission generated by the deceleration of the non-relativistic ejecta mass in a circumstellar medium with profile $n(r) \propto r^{-k}$. Once the ejecta mass propagates into the circumstellar medium, it first moves with a constant velocity, and later, when the swept up quantity of material is similar to the ejected mass, it begins to decelerate. During these stages, electrons are accelerated in the forward shocks, and are cooled down by synchrotron and synchrotron-self Compton (SSC) processes. We present the predicted synchrotron and SSC light curves for k = 0, 1, 1.5, 2 and 2.5 that cover several ejecta masses launched during the coalescence of binary compact objects and the CC-SNe. Particularly, with the multi-wavelength observations and upper limits collected by a large campaign of orbiting satellites and ground telescopes, we constrain the parameter space of both the KN afterglow in GW170817 and the possibly generated KN afterglow produced by the coalescence of a BH-NS system in S190814bv. The paper is organized as follows: In Section 2, we introduce the theoretical model

that predicts the multi-wavelength afterglow emission generated by the deceleration of the non-relativistic ejecta mass. In Section 3, we show the predicted synchrotron and SSC light curves for a density profile with k = 0, 1, 1.5, 2 and 2.5. In Section 4, we show the synchrotron and SSC light curves from material launched during the coalescence of a NS binary. In section 5, we discuss the non-relativistic ejected mass around the KN emission. In Section 6, we apply our model to two particular cases, to GW170817 and S190814bv and finally in Section 7, we present the discussion and summary. We adopt the convention $Q_x = \frac{Q}{10^x}$ in c.g.s. units and assume for the cosmological constants a spatially flat universe ΛCDM model with $H_0 = 69.6 \, \mathrm{km \, s^{-1} \, Mpc^{-1}}$, $\Omega_M = 0.286$ and $\Omega_\Lambda = 0.714$ (Planck Collaboration et al. 2016). Prime and unprimed quantities are used for the comoving and observer frames, respectively.

2. AFTERGLOW LIGHT CURVES OF A NON-RELATIVISTIC EJECTA MASS

In this section, we show the dynamics of the forward shocks given by the deceleration of the ejecta mass in a density profile $n(r) = A_k \, r^{-k}$ with A_k the density parameter and $0 \leq k < 3$. We use analytical arguments in order to compute the synchrotron and SSC light curves expected in the non-relativistic regime. The synchrotron and SSC radiation is derived in the fully adiabatic regime during the free-coasting and the deceleration phase assuming an electron distribution described by $dN/d\gamma_e \propto \gamma_e^{-p}$, for $\gamma_e \geq \gamma_m$, where γ_m is the Lorentz factors of the lowest-energy electrons and p is the index of the electron distribution. We only consider the dynamics of the forward shocks instead of reverse shocks because electrons accelerated in the reverse shocks generate short-lived emissions and we are interested in describing emissions extended in timescales from days to years.

Irrespective of the progenitor, non-relativistic materials with a wide range of masses and velocities are launched into the circumstellar medium. After a time t following the coalescence or collapse, a generic ejecta mass moves with a constant velocity β and expands with a mean radius $r \approx \beta t$ (e.g., see Kulkarni et al. 1998; Metzger 2019). The initial expansion phase is not affected by the circumstellar medium, but once the swept up quantity of material is as large as the ejected mass, the ejecta begins to be decelerated (Rosswog et al. 2014). During the deceleration phase, numerical simulations indicate that the velocity of matter in the front the ejecta is faster than the one that moves in the back, so that the ejecta acquires a velocity structure (e.g., see Rosswog et al. 2014; Tan et al. 2001).

2.1. The free-coasting phase

During the initial expansion, the ejecta mass is not affected by the circumstellar medium (Rosswog et al. 2014), so the velocity is constant $\beta \propto t^0$ and the radius evolves as $r \propto (1+z)^{-1} t$.

2.1.1. Synchrotron emission

During the coasting phase, the post-shock magnetic field evolves as, $B' \propto \epsilon_B^{\frac{1}{2}} A_k^{\frac{1}{2}} \beta^{\frac{2-k}{2}} t^{-\frac{k}{2}}$ where ϵ_B is the microphysical parameter associated to the magnetic density. The Lorentz factors of the lowest-energy electrons and of the higher energy electrons, which are efficiently cooled by synchrotron emission are

$$\gamma_m = \gamma_m^0 \, g(p) \epsilon_{e,-1} \, \beta_{-0.5}^2$$

$$\gamma_c = \gamma_c^0 \left(\frac{1+z}{1.022}\right)^{1-k} (1+Y)^{-1} \epsilon_{B,-2}^{-1} A_k^{-1} \beta_{-0.5}^{k-2} t_6^{k-1}, \quad (1)$$

where Y is the Compton parameter (Sari and Esin 2001), $g(p) = \frac{p-2}{p-1}$, ϵ_e is the microphysical parameter associated to the electron density and z is the redshift of a generic observer located at 100 Mpc. Given the evolution of the synchrotron frequencies as a function of the electron Lorentz factors $\nu_i^{\mathrm{syn}} \propto \gamma_i^2$ for i = m and c, using eq. (1) the corresponding synchrotron break frequencies can be written as

$$\nu_m^{\mathrm{syn}} = \nu_m^{\mathrm{syn},0} g^2(p) \left(\frac{1+z}{1.022}\right)^{\frac{k-2}{2}} \epsilon_{e,-1}^2 \epsilon_{B,-1}^{\frac{1}{2}} A_k^{\frac{1}{2}} \beta_{-0.5}^{\frac{10-k}{2}} t_6^{-\frac{k}{2}}$$

$$\nu_c^{\mathrm{syn}} = \nu_c^{\mathrm{syn},0} \left(\frac{1+z}{1.022}\right)^{\frac{2-3k}{2}} (1+Y)^{-2} \epsilon_{B,-2}^{-\frac{3}{2}} A_k^{-\frac{3}{2}} \beta_{-0.5}^{\frac{3k-6}{2}} t_6^{\frac{3k-4}{2}} . (2)$$

In the self-absorption regime, the synchrotron break frequencies are (Panaitescu and Kumar 2000; Gao et al. 2015)

$$\nu_{a,1}^{\mathrm{syn}} = \nu_{a,1}^{\mathrm{syn},0} \left(\frac{1+z}{1.022}\right)^{\frac{4(k-2)}{5}} g(p)^{-1} \epsilon_{e,-1}^{-1} \epsilon_{B,-2}^{\frac{1}{5}} A_k^{\frac{4}{5}} \beta_{-0.5}^{-\frac{4k+5}{5}} t_6^{\frac{3-4k}{5}},$$

$$\nu_{a,2}^{\mathrm{syn}} = \nu_{a,2}^{\mathrm{syn},0} \left(\frac{1+z}{1.022}\right)^{\frac{(k-2)(p+6)}{2(p+4)}} g(p)^{\frac{2(p-1)}{p+4}} \epsilon_{e,-1}^{\frac{2(p-1)}{p+4}} \epsilon_{B,-2}^{\frac{p+2}{2(p+4)}}$$

$$\times A_k^{\frac{p+6}{2(p+4)}} \beta_{-0.5}^{\frac{10p-kp-6k}{2(p+4)}} t_6^{\frac{4-kp-6k}{2(p+4)}},$$

$$\nu_{a,3}^{\mathrm{syn}} = \nu_{a,3}^{\mathrm{syn},0} \left(\frac{1+z}{1.022}\right)^{\frac{9k-13}{5}} (1+Y) \epsilon_{B,-2}^{\frac{6}{5}} A_k^{\frac{9}{5}} \beta_{-0.5}^{\frac{15-9k}{5}} t_6^{\frac{8-9k}{5}}, \quad (3)$$

where $\nu_{a,l}^{\mathrm{syn}}$ for l=1, 2 and 3 are defined in the range of $\nu_{a,1}^{\mathrm{syn}} \leq \nu_m^{\mathrm{syn}} \leq \nu_c^{\mathrm{syn}}$, $\nu_m^{\mathrm{syn}} \leq \nu_{a,2}^{\mathrm{syn}} \leq \nu_c^{\mathrm{syn}}$ and $\nu_{a,3}^{\mathrm{syn}} \leq \nu_c^{\mathrm{syn}} \leq \nu_m^{\mathrm{syn}}$, respectively. Taking into account that the peak spectral power evolves as $P_{\nu,\mathrm{max}} \propto (1+z)^{\frac{k-2}{2}} \epsilon_B^{\frac{1}{2}} A_k^{\frac{1}{2}} \beta^{\frac{2-k}{2}} t^{-\frac{k}{2}}$ and that the number of swept-up electrons in the post-shock is $N_e \propto (1+z)^{k-3} A_k \beta^{3-k} t^{3-k}$, the spectral peak flux density is given by

$$F_{\nu,\mathrm{max}}^{\mathrm{syn}} = F_{\nu,\mathrm{max}}^{\mathrm{syn},0} \left(\frac{1+z}{1.022}\right)^{\frac{3k-4}{2}} \epsilon_{B,-2}^{\frac{1}{2}} d_{z,26.5}^{-2} A_k^{\frac{3}{2}} \beta_{-0.5}^{\frac{8-3k}{2}} t_6^{\frac{3(2-k)}{2}},$$

$$\quad (4)$$

where $d_z = (1+z)\frac{c}{H_0} \int_0^z \frac{d\tilde{z}}{\sqrt{\Omega_M(1+\tilde{z})^3 + \Omega_\Lambda}}$ (Weinberg 1972) is the luminosity distance with c the speed of light. The terms $\gamma_m^0, \gamma_c^0, \nu_m^{\mathrm{syn},0}, \nu_c^{\mathrm{syn},0}$ and $F_{\nu,\mathrm{max}}^{\mathrm{syn},0}$ are given in Table 1 for k = 0, 1, 1.5, 2 and 2.5.

Using the synchrotron break frequencies (eqs. 2 and 3) and the spectral peak flux density (eq. 4), the synchrotron light curves in the fast- and the slow-cooling regime evolve as

$$F_\nu^{\mathrm{syn}} \propto \begin{cases} t^{1+k} \nu^2, & \nu < \nu_{a,3}^{\mathrm{syn}}, \\ t^{\frac{11-6k}{3}} \nu^{\frac{1}{3}}, & \nu_{a,3}^{\mathrm{syn}} < \nu < \nu_c^{\mathrm{syn}}, \\ t^{\frac{8-3k}{4}} \nu^{-\frac{1}{2}}, & \nu_c^{\mathrm{syn}} < \nu < \nu_m^{\mathrm{syn}}, \\ t^{\frac{8-k(p+2)}{4}} \nu^{-\frac{p}{2}}, & \nu_m^{\mathrm{syn}} < \nu, \end{cases} \quad (5)$$

$$F_\nu^{\mathrm{syn}} \propto \begin{cases} t^2 \nu^2, & \nu < \nu_{a,1}^{\mathrm{syn}}, \\ t^{\frac{9-4k}{3}} \nu^{\frac{1}{3}}, & \nu_{a,1}^{\mathrm{syn}} < \nu < \nu_m^{\mathrm{syn}}, \\ t^{\frac{12-k(p+5)}{4}} \nu^{-\frac{p-1}{2}}, & \nu_m^{\mathrm{syn}} < \nu < \nu_c^{\mathrm{syn}}, \\ t^{\frac{8-k(p+2)}{4}} \nu^{-\frac{p}{2}}, & \nu_c^{\mathrm{syn}} < \nu, \end{cases} \quad (6)$$

and

$$F_\nu^{\mathrm{syn}} \propto \begin{cases} t^2 \nu^2, & \nu < \nu_m^{\mathrm{syn}}, \\ t^{\frac{8+k}{4}} \nu^{\frac{5}{2}}, & \nu_m^{\mathrm{syn}} < \nu < \nu_{a,2}^{\mathrm{syn}}, \\ t^{\frac{12-k(p+5)}{4}} \nu^{-\frac{p-1}{2}}, & \nu_{a,2}^{\mathrm{syn}} < \nu < \nu_c^{\mathrm{syn}}, \\ t^{\frac{8-k(p+2)}{4}} \nu^{-\frac{p}{2}}, & \nu_c^{\mathrm{syn}} < \nu, \end{cases} \quad (7)$$

respectively. It is worth noting that the synchrotron light curves in the fast-cooling regime are derived for completeness, since they are not relevant for the problems investigated here.

2.1.2. SSC emission

The electron distribution accelerated during the forward shock up-scatters synchrotron photons, yielding the SSC spectrum which is characterized by the break frequencies $\nu_{ij}^{\mathrm{ssc}} = 4\gamma_i^2 \nu_j^{\mathrm{syn}} x_0$ with i, j = a, m and c where x_0 is a parameter that assures energy conservation (e.g., see Sari and Esin 2001; Zhang and Mészáros 2001; Gao et al. 2013b). The SSC break frequencies, the corresponding spectral peak flux density and the light curves in the fast- and slow-cooling regime are shown in appendix.

2.2. The deceleration phase

During the deceleration phase, the ejecta acquires a velocity structure, the velocity of matter in the front of the ejecta is faster than the one that moves in the back (Sari and Mészáros 2000). Tan et al. (2001) studied the acceleration of the ejecta mass with relativistic and sub-relativistic velocities. They found that the equivalent kinetic energy in the non- and ultra-relativistic limit can be expressed as a PL velocity distribution given by $E_k(\geq \beta) \propto \beta^{-5.2}$ for $\beta \ll 1$ and $E_k(\geq \beta\Gamma) \propto (\beta\Gamma)^{-1.1}$ for $\beta\Gamma \gg 1$ (with $\Gamma = \sqrt{1/1-\beta^2}$), respectively.[3] Here, we consider the non-relativistic regime, so the equivalent kinetic energy distribution given by $E_k(\geq \beta) = \tilde{E}\beta^{-\alpha}$ with $\tilde{E}$ the fiducial energy and the values $3 \leq \alpha \leq 5.2$ are used. We adopt this range of values motivated by the numerical simulations presented in Tan et al. (2001).

During this phase the dynamics of the non-relativistic ejecta mass is described by the Sedov-Taylor solution. Then, the velocity and the blast wave radius can be written as

$$\beta = \beta^0 \left(\frac{1+z}{1.022}\right)^{\frac{3-k}{\alpha+5-k}} A_k^{-\frac{1}{\alpha+5-k}} \tilde{E}_{51}^{\frac{1}{\alpha+5-k}} t_7^{\frac{k-3}{\alpha+5-k}}, \quad (8)$$

and

$$r = r^0 \left(\frac{1+z}{1.022}\right)^{-\frac{\alpha+2}{\alpha+5-k}} A_k^{-\frac{1}{\alpha+5-k}} \tilde{E}_{51}^{\frac{1}{\alpha+5-k}} t_7^{\frac{\alpha+2}{\alpha+5-k}}, \quad (9)$$

respectively, where the fiducial energy ($\tilde{E}$) can be estimated by calculating the term $\propto \beta^2 r^3$. From eq. (8) it can be noticed that the deceleration time evolves as

$$t_{\mathrm{dec}} = t_{\mathrm{dec}}^0 \left(\frac{1+z}{1.022}\right) A_k^{\frac{1}{k-3}} \tilde{E}_{51}^{\frac{1}{3-k}} \beta_{-0.5}^{\frac{k+5-k}{k-3}}. \quad (10)$$

The terms r^0 and t_{dec}^0 are given in Table 1 for k = 0, 1, 1.5, 2 and 2.5. It is worth noting that for a uniform-density medium (k=0) and $\alpha = 0$, the velocity and blast wave radius derived in Sironi and Giannios (2013) are recovered.

2.2.1. Synchrotron emission

During the deceleration phase, the post-shock magnetic field evolves as, $B' \propto t^{-\frac{6+k\alpha}{2(\alpha+5-k)}}$. The Lorentz factors of the lowest-energy electrons and of the higher energy electrons, which are efficiently cooled by synchrotron emission are

$$\gamma_m = \gamma_m^0 \left(\frac{1+z}{1.022}\right)^{\frac{2(3-k)}{\alpha+5-k}} g(p) \epsilon_{e,-1} A_k^{-\frac{2}{\alpha+5-k}} \tilde{E}_{51}^{\frac{2}{\alpha+5-k}} t_7^{\frac{2(k-3)}{\alpha+5-k}}$$

$$\gamma_c = \gamma_c^0 \left(\frac{1+z}{1.022}\right)^{-\frac{k+1+\alpha(k-1)}{\alpha+5-k}} (1+Y)^{-1} \epsilon_{B,-2}^{-1} A_k^{-\frac{\alpha+3}{\alpha+5-k}}$$

$$\times \tilde{E}_{51}^{\frac{k-2}{\alpha+5-k}} t_7^{\frac{k+1+\alpha(k-1)}{\alpha+5-k}}. \quad (11)$$

---

[3] The polytropic index $n_p = 3$ is used.

The corresponding synchrotron break frequencies are given by

$$\nu_{\rm m}^{\rm syn} = \nu_{\rm m}^{\rm syn,0} \left(\frac{1+z}{1.022}\right)^{\frac{20+k(\alpha-6)-2\alpha}{2(\alpha+5-k)}} g(p)^2 \epsilon_{\rm e,-1}^2 \epsilon_{\rm B,-2}^{\frac{1}{2}} A_{\rm k}^{\frac{\alpha-5}{2(\alpha+5-k)}}$$
$$\times \tilde{E}_{51}^{\frac{10-k}{2(\alpha+5-k)}} t_7^{-\frac{30+k(\alpha-8)}{2(\alpha+5-k)}}$$

$$\nu_{\rm c}^{\rm syn} = \nu_{\rm c}^{\rm syn,0} \left(\frac{1+z}{1.022}\right)^{-\frac{8-2\alpha+k(3\alpha+2)}{2(\alpha+5-k)}} \epsilon_{\rm B,-2}^{-\frac{3}{2}} (1+Y)^{-2}$$
$$\times A_{\rm k}^{-\frac{3(\alpha+3)}{2(\alpha+5-k)}} \tilde{E}_{51}^{\frac{3(k-2)}{2(\alpha+5-k)}} t_7^{\frac{k(4+3\alpha)-4\alpha-2}{2(\alpha+5-k)}} . \quad (12)$$

In the self-absorption regime, the synchrotron break frequencies are

$$\nu_{\rm a,1}^{\rm syn} = \nu_{\rm a,1}^{\rm syn,0} \left(\frac{1+z}{1.022}\right)^{m_{11}} g(p)^{-1} \epsilon_{\rm e,-1}^{-1} \epsilon_{\rm B,-2}^{\frac{1}{5}} A_{\rm k}^{\frac{25+4\alpha}{5(\alpha+5-k)}}$$
$$\times \tilde{E}_{51}^{-\frac{4k+5}{5(\alpha+5-k)}} t_6^{m_{21}}$$

$$\nu_{\rm a,2}^{\rm syn} = \nu_{\rm a,2}^{\rm syn,0} \left(\frac{1+z}{1.022}\right)^{m_{12}} g(p)^{\frac{2(p-1)}{p+4}} \epsilon_{\rm e,-1}^{\frac{2(p-1)}{p+4}} A_{\rm k}^{\frac{\alpha p+6\alpha-5p+30}{2(p+4)(\alpha+5-k)}}$$
$$\times \epsilon_{\rm B,-2}^{\frac{p+2}{2(p+4)}} \tilde{E}_{51}^{\frac{10p-kp-6k}{2(p+4)(\alpha+5-k)}} t_6^{m_{22}},$$

$$\nu_{\rm a,3}^{\rm syn} = \nu_{\rm a,3}^{\rm syn,0} \left(\frac{1+z}{1.022}\right)^{m_{13}} (1+Y)^{\frac{6}{5}} \epsilon_{\rm B,-2}^{\frac{6}{5}} A_{\rm k}^{\frac{3(3\alpha+10)}{5(\alpha+5-k)}}$$
$$\times \tilde{E}_{51}^{\frac{15-9k}{5(\alpha+5-k)}} t_6^{m_{23}}, \quad (13)$$

where the PL indices $m_{\rm ij}$ for $i, j =$ 1, 2 and 3 are explicitly shown in the appendix.

Taking into account that the peak spectral power evolves as $P_{\nu,\max} \propto t^{-\frac{6+k\alpha}{2(\alpha+5-k)}}$ and the number of swept-up electrons in the post-shock develops as $N_{\rm e} \propto t^{\frac{6-2k+\alpha(3-k)}{\alpha+5-k}}$, the spectral peak flux density becomes

$$F_{\nu,\max}^{\rm syn} = F_{\nu,\max}^{\rm syn,0} \left(\frac{1+z}{1.022}\right)^{\frac{4+2k-4\alpha+3k\alpha}{2(\alpha+5-k)}} \epsilon_{\rm B,-2}^{\frac{1}{2}} d_{\rm z,26.5}^{-2} A_{\rm k}^{\frac{3\alpha+7}{2(\alpha+5-k)}}$$
$$\times \tilde{E}_{51}^{\frac{8-3k}{2(\alpha+5-k)}} t_7^{\frac{6-4k+6\alpha-3k\alpha}{2(\alpha+5-k)}} . \quad (14)$$

The terms $\gamma_{\rm m}^0$, $\gamma_{\rm c}^0$, $\nu_{\rm m}^{\rm syn,0}$, $\nu_{\rm c}^{\rm syn,0}$ and $F_{\nu,\max}^{\rm syn,0}$ are given in Table 1 for k = 0, 1, 1.5, 2 and 2.5.

Using the synchrotron break frequencies (eq. 12) and the spectral peak flux density (eq. 14), the synchrotron light curves in the fast- and the slow-cooling regime are

$$F_\nu^{\rm syn} \propto \begin{cases} t^{\frac{5+k+\alpha+k\alpha}{\alpha+5-k}} \nu^2, & \nu < \nu_{\rm a,3}^{\rm syn}, \\ t^{\frac{10-8k+11\alpha-6k\alpha}{3(\alpha+5-k)}} \nu^{\frac{1}{3}}, & \nu_{\rm a,3}^{\rm syn} < \nu < \nu_{\rm c}^{\rm syn} \\ t^{\frac{10-4k+8\alpha-3k\alpha}{4(\alpha+5-k)}} \nu^{-\frac{1}{2}}, & \nu_{\rm c}^{\rm syn} < \nu < \nu_{\rm m}^{\rm syn}, \\ t^{-\frac{30p+kp(\alpha-8)-8(\alpha+5)+2k(\alpha+6)}{4(\alpha+5-k)}} \nu^{-\frac{p}{2}}, & \nu_{\rm m}^{\rm syn} < \nu, \end{cases} \quad (15)$$

$$F_\nu^{\rm syn} \propto \begin{cases} t^{\frac{2(\alpha+k-1)}{\alpha+5-k}} \nu^2, & \nu < \nu_{\rm a,1}^{\rm syn}, \\ t^{\frac{24+9\alpha-2k(2\alpha+5)}{3(\alpha+5-k)}} \nu^{\frac{1}{3}}, & \nu_{\rm a,1}^{\rm syn} < \nu < \nu_{\rm m}^{\rm syn} \\ t^{-\frac{6(5p-2\alpha-7)+k(16+p(\alpha-8)+5\alpha)}{4(\alpha+5-k)}} \nu^{-\frac{p-1}{2}}, & \nu_{\rm m}^{\rm syn} < \nu < \nu_{\rm c}^{\rm syn}, \\ t^{-\frac{30p+kp(\alpha-8)-8(\alpha+5)+2k(\alpha+6)}{4(\alpha+5-k)}} \nu^{-\frac{p}{2}}, & \nu_{\rm c}^{\rm syn} < \nu, \end{cases} \quad (16)$$

and

$$F_\nu^{\rm syn} \propto \begin{cases} t^{\frac{2(\alpha+k-1)}{\alpha+5-k}} \nu^2, & \nu < \nu_{\rm m}^{\rm syn}, \\ t^{\frac{22+\alpha(k+8)}{4(\alpha+5-k)}} \nu^{\frac{5}{2}}, & \nu_{\rm m}^{\rm syn} < \nu < \nu_{\rm a,2}^{\rm syn}, \\ t^{-\frac{6(5p-2\alpha-7)+k(16+p(\alpha-8)+5\alpha)}{4(\alpha+5-k)}} \nu^{-\frac{p-1}{2}}, & \nu_{\rm a,2}^{\rm syn} < \nu < \nu_{\rm c}^{\rm syn}, \\ t^{-\frac{30p+kp(\alpha-8)-8(\alpha+5)+2k(\alpha+6)}{4(\alpha+5-k)}} \nu^{-\frac{p}{2}}, & \nu_{\rm c}^{\rm syn} < \nu, \end{cases} \quad (17)$$

respectively.

2.2.2. *SSC emission*

The SSC break frequencies, the corresponding spectral peak flux density and the light curves in the fast- and slow-cooling regime are shown in Appendix.

3. ANALYSIS OF THE MULTI-WAVELENGTH LIGHT CURVES

3.1. *Analysis of synchrotron light curves*

Figures 1 - 5 show the predicted synchrotron light curves produced by the deceleration of the non-relativistic ejecta in a circumstellar medium described by a density profile $A_{\rm k} r^{-\rm k}$ with k = 0, 1, 1.5, 2 and 2.5, respectively. Panels from top to bottom correspond to the electromagnetic bands in radio at 6 GHz, optical at 1 eV and X-rays at 1 keV for $\tilde{E} = 10^{51}$ erg, $\epsilon_{\rm B} = 10^{-2}$, $\epsilon_{\rm e} = 10^{-1}$ and $d_z = 100$ Mpc. The left-hand panels show the light curves for $p = 2.6$ with $\alpha = 3, 4$ and 5, and the right-hand panels show the light curves for $\alpha = 3$ with $p = 2.2, 2.8$ and 3.4. All the figures lie in the slow-cooling regime and exhibit a deceleration timescale from several months to a few years due to the set of parameter values considered. Similar timescales have been observed in the light curves from radio to hard X-rays in some SNe (e.g., SN2014C and SN2016aps; Margutti et al. 2017; Nicholl et al. 2020, respectively). If we had chosen another set of parameters such as a fiducial energy $\tilde{E} \simeq 10^{52}$ erg, a uniform-density medium $A_0 \simeq 10 \, {\rm cm}^{-3}$ and equipartition parameters $\epsilon_{\rm e} \simeq 0.5$ and $\epsilon_{\rm B} \simeq 0.1$, the synchrotron light curves would lie in the fast-cooling regime. Consequently, using a set of parameters such as $\tilde{E} \simeq 10^{47}$ erg, $A_2 \simeq 3 \times 10^{35} \, {\rm cm}^{-1}$ and $\beta = 0.5$ for k = 2, and $\tilde{E} \sim 10^{47}$ erg, $A_0 \simeq 1 \, {\rm cm}^{-3}$ and $\beta = 0.5$ for k = 0, deceleration timescales from hours to months would have been obtained. This is also the case, for instance, where the ejecta mass is decelerated in a very dense medium (for discussion, see Chevalier and Irwin 2011; Nicholl et al. 2020).

The density profile of $n(r) = A_{\rm k} r^{-\rm k}$ with k = 0, 1, 1.5, 2 and 2.5 for the circumstellar medium that covers short and long GRB progenitors is used. While the uniform-density medium (k = 0) is expected to be connected with binary compact objects and CC-SNe, the stratified medium ($1 \leq$ k ≤ 2.5) is only expected to be associated to dying massive stars with different mass-loss evolution. For instance, Yi et al. (2013) and Liang et al. (2013) studied the dynamics of synchrotron external-shock emission in a sample of 19 and 146 GRBs and found that they were successfully described when the outflow was decelerated in an external environment with $0.4 \leq$ k ≤ 1.4 and k ≈ 1, respectively. Izzo et al. (2020) presented multi-wavelength observations of the nearby SN 2020bvc. The authors found that the X-ray observations were consistent with the afterglow emission generated by an off-axis jet with viewing angle of $23°$ when it was decelerated in a circumburst medium with a density profile with k = 1.5. Figure 1 exhibits that during the coasting phase, the flux increases gradually, and during the deceleration phase, depending on the values of α and p, a flattening or decrease in the light curve is expected. Figures 2 - 5 show that for a density profile with $1 <$ k ≤ 2.5 the rebrightening in the light curves is not so evident. Therefore, a flattening or rebrightening at timescales from months to years in the light curves together with GW detection would be associated with the deceleration of a non-relativistic ejecta launched during the coalescence of binary compact objects or a CC-SN. Even a flattening or rebrightening at timescales of days could be detected with extreme values of circumstellar density or fiducial energy. Additionally, it can be concluded that an observed flux that decreases early would be associated with the deceleration of a non-relativistic ejecta launched by dying massive stars with different mass-loss evolution (the mass loss rate $\dot{M}$ and/or the wind velocity $v_{\rm w}$) at the end of their life (Ramirez-Ruiz et al. 2005; van Marle et al. 2006).

The synchrotron light curve in the slow-cooling regime as a function

of the density parameter during the deceleration phase is given by

$$F_\nu^{\rm syn} \propto \begin{cases} A_{\rm k}^{-\frac{4}{\alpha+5-k}}, & \nu < \nu_{\rm a,1}^{\rm syn}, \\ A_{\rm k}^{\frac{4\alpha+13}{3(\alpha+5-k)}}, & \nu_{\rm a,1}^{\rm syn} < \nu_{\rm m}^{\rm syn}, \\ A_{\rm k}^{\frac{19+p(\alpha-5)+5\alpha}{4(\alpha+5-k)}}, & \nu_{\rm m}^{\rm syn} < \nu < \nu_{\rm c}^{\rm syn}, \\ A_{\rm k}^{\frac{p(\alpha-5)+2(\alpha+5)}{4(\alpha+5-k)}}, & \nu_{\rm c}^{\rm syn} < \nu. \end{cases} \quad (18)$$

The predicted flux is less sensitive to the density parameter for higher frequencies than for the lower ones (e.g., the radio light curve is more sensitive to variations of the density parameter than the X-ray light curve). It can also be noticed that the predicted flux is more sensitive to the density parameter for larger values of k and α. It is worth noting that a transition phase from stellar-wind (k=2) to uniform-density (k=0) medium would be more evident in lower-frequency fluxes (e.g., this transition is more noticeable in radio or optical than in X-ray bands). A similar signature was useful to describe the type of the progenitor, the mass-loss evolution, the afterglow emission by the deceleration of the relativistic jet, and also to estimate the transition radius at $\sim (0.1-1)$ pc of some bursts (e.g. see GRB 050319, 080109A, 160625B and 190114C; Kamble et al. 2007; Jin et al. 2009; Fraija et al. 2017, 2019c).
Figures 1 - 5 show the synchrotron light curves for distinct values of p and α, and the same values of the microphysical parameters $\epsilon_{\rm B} = 10^{-2}$ and $\epsilon_{\rm e} = 10^{-1}$. However, any variation of the microphysical parameters will increase or decrease the predicted fluxes. For example, the synchrotron light curve in the slow-cooling regime as a function of these parameters evolves as $F_\nu^{\rm syn} : \propto \epsilon_{\rm e}^{-\frac{2}{3}} \epsilon_{\rm B}^{\frac{1}{3}}$ for $\nu < \nu_{\rm m}^{\rm syn}$, $\propto \epsilon_{\rm e}^{p-1} \epsilon_{\rm B}^{\frac{p+1}{4}}$ for $\nu_{\rm m}^{\rm syn} < \nu < \nu_{\rm c}^{\rm syn}$ and $\propto \epsilon_{\rm e}^{p-1} \epsilon_{\rm B}^{\frac{p-2}{4}}$ for $\nu_{\rm c}^{\rm syn} < \nu$. The expected flux is more sensitive to the parameter $\epsilon_{\rm B}$ for lower frequencies than for higher ones, and the parameter $\epsilon_{\rm e}$ for higher frequencies than for lower ones.
The synchrotron spectral breaks during the non-relativistic regime evolve as $\nu_{\rm m}^{\rm syn} \propto t^{-\frac{k}{2}}$ and $\nu_{\rm c}^{\rm syn} \propto t^{\frac{3k-4}{2}}$ in the coasting phase, and $\nu_{\rm m}^{\rm syn} \propto t^{-\frac{30+k(\alpha-8)}{2(\alpha+5-k)}}$ and $\nu_{\rm c}^{\rm syn} \propto t^{\frac{k(4+3\alpha)-4\alpha-2}{2(\alpha+5-k)}}$ in the deceleration phase. For instance, these breaks evolve as $\nu_{\rm m}^{\rm syn} \propto t^0$ and $\nu_{\rm c}^{\rm syn} \propto t^{-2}$ in the coasting phase and $\nu_{\rm m}^{\rm syn} \propto t^{-3}$ and $\nu_{\rm c}^{\rm syn} \propto t^{-\frac{1}{5}}$ in the deceleration phase for a uniform-density medium, and $\nu_{\rm m}^{\rm syn} \propto t^{-1}$ and $\nu_{\rm c}^{\rm syn} \propto t$ in the coasting phase and $\nu_{\rm m}^{\rm syn} \propto t^{-\frac{7}{3}}$ and $\nu_{\rm c}^{\rm syn} \propto t$ in the deceleration phase for a stellar-wind medium. Here, we present a valuable tool to pinpoint the emission from the non-relativistic ejecta as previously done by Giblin et al. (1999) in the case of the relativistic regime. Giblin et al. (1999) analyzed the prompt gamma-ray emission in the BATSE[4] detected burst GRB 980923. The light curve exhibited a main prompt episode lasting $\sim 40\,{\rm s}$ followed by a smooth emission tail that lasted $\sim 400\,{\rm s}$. The authors found that the spectrum in the smooth tail evolved as the synchrotron cooling break $\propto t^{-0.52\pm0.12}$, concluding that the afterglow began during the prompt gamma-ray emission. Afterward, spectra analysis of GRB tails were done in order to identify early afterglows (e.g., see Barthelmy et al. 2005; Yamazaki et al. 2006).

3.2. *Analysis of SSC light curves*

Figure 6 shows the predicted SSC light curves at 100 keV (upper), 10 GeV (medium) and 100 GeV (lower) for the deceleration of the non-relativistic ejecta mass in a circumstellar medium with a density profile $A_{\rm k} r^{-k}$ with k = 0, 1, 1.5, 2 and 2.5, respectively. The left-hand panels show the light curves for $p = 2.4$ and $\alpha = 3$, and the right-hand panels for $p = 2.8$ and $\alpha = 5$. In order to obtain the SSC light curves, we use the same typical values that are used for the synchrotron light curves. The effect of the extragalactic

[4] Burst and Transient Source Experiment

background light (EBL) absorption modelled in Franceschini and Rodighiero (2017) is used.

The purple solid line (k = 0) in Figure 6 shows that a flattening or rebrightening in the light curve is expected, but not in a density profile with k > 1. This feature at timescales from months to years together with GW detection would be associated with the deceleration of a non-relativistic ejecta launched during the coalescence of a binary compact object or a CC-SN. On the contrary, it is expected that an observed flux that decreases early would be associated with the deceleration of a non-relativistic ejecta launched in the collapse of massive stars with different mass-loss evolution at the end of their life (Ramirez-Ruiz et al. 2005; van Marle et al. 2006).
The SSC light curve in the slow-cooling regime as a function of the density parameter during the deceleration phase can be written as

$$F_\nu^{\rm ssc} \propto \begin{cases} A_{\rm k}^{\frac{9(\alpha+5)}{5(\alpha+5-k)}}, & \nu < \nu_{\rm a,1}^{\rm ssc}, \\ A_{\rm k}^{\frac{29+7\alpha}{3(\alpha+5-k)}}, & \nu_{\rm a,1}^{\rm ssc} < \nu_{\rm m}^{\rm ssc}, \\ A_{\rm k}^{\frac{43+p(\alpha-13)+9\alpha}{4(\alpha+5-k)}} \left(C_1 + C_2 \ln A_{\rm k}^{-\frac{7(\alpha+3)}{2(\alpha+5-k)}} \right), & \nu_{\rm m}^{\rm ssc} < \nu < \nu_{\rm c}^{\rm ssc}, \\ A_{\rm k}^{\frac{22-13p+2\alpha+\alpha p}{4(\alpha+5-k)}} \left(C_3 + C_4 \ln A_{\rm k}^{\frac{7(\alpha+3)}{2(\alpha+5-k)}} \right), & \nu_{\rm c}^{\rm ssc} < \nu. \end{cases} \quad (19)$$

The parameters $C_{\rm s}$ do not evolve with the density parameter. Considering that the contribution from the logarithm function is small, this light curve has a similar behavior to the synchrotron light curves.
Inverse Compton (IC) scattering between an electron distribution accelerated during the shock wave and the photon field from SNe has been explored in order to explain the X-ray emission observed in timescales of days after the explosion (Björnsson and Fransson 2004; Chevalier and Fransson 2006; Chevalier et al. 2006; Margutti et al. 2013). Björnsson and Fransson (2004) studied the X-ray and radio emission from SN 2002ap. The authors proposed that IC scattering could explain the X-ray excess observed at late times. They computed that the IC spectrum six days after the explosion peaks at energies of some MeV. Chevalier and Fransson (2006) found that although the IC emission could reproduce the X-ray flux observed in SN2002ap for a spectral index of $p = 3$, this process is not promising for other SNe unless the electron energy density is much larger than the magnetic energy density. On the other hand, Margutti et al. (2012) introduced an analytic formalism for the IC scattering in the X-ray energy range and in the SN scenario with compact progenitors. They showed that the IC luminosity evolves as $\propto t^{1.29-0.58p}$ for a uniform-density medium and $\propto t^{-(0.24p+0.64)}$ for a wind medium. In this paper, we propose that in addition to the external IC scattering process, the SSC mechanism could be present. Figure 6 shows that in a density profile with $k > 1$, the SSC flux could be detected in timescales of days with the evolution given by eqs. (A14) and (A15). For instance, the SSC fluxes in the slow-cooling regime evolve as $\propto t^{\frac{4\alpha+14}{\alpha+5}}$ for $\nu < \nu_{\rm m}^{\rm ssc}$, $\propto t^{\frac{37-27p+8\alpha}{2(\alpha+5)}}$ for $\nu_{\rm m}^{\rm ssc} < \nu < \nu_{\rm c}^{\rm ssc}$ and $\propto t^{\frac{38-27p+4\alpha}{2(\alpha+5)}}$ for $\nu_{\rm c}^{\rm ssc} < \nu$ for a uniform-density medium, and as $\propto t^{\frac{2(1-\alpha)}{3(\alpha+3)}}$ for $\nu < \nu_{\rm m}^{\rm ssc}$, $\propto t^{\frac{5-\alpha-p(\alpha+11)}{2(\alpha+3)}}$ for $\nu_{\rm m}^{\rm ssc} < \nu < \nu_{\rm c}^{\rm ssc}$ and $\propto t^{\frac{14-11p+\alpha(2-p)}{2(\alpha+3)}}$ for $\nu_{\rm c}^{\rm ssc} < \nu$ for a stellar-wind medium, which have a different evolution to the IC scattering model derived in Margutti et al. (2012).

4. THE NON-RELATIVISTIC MASSES EJECTED FROM THE COALESCENCE OF A NS BINARY

The coalescence of NS mergers is widely accepted to launch significant masses with different velocities which will contribute at distinct timescales, frequencies and intensities. Once these ejecta masses move into the circumstellar medium, the initial expansion

phase is not affected until the swept up quantity of material is equal to the ejected masses. In this moment, the ejecta masses start to be decelerated. The non-relativistic masses ejected from the coalescence of the NS merger are the dynamical ejecta, the cocoon material, the shock breakout material and the wind ejecta. As follows we give a brief introduction of each of these ejecta masses.

4.1. *The dynamical ejecta*

The dynamical ejecta is formed during the coalescence due to hydrodynamical and gravitational interactions (Davies et al. 1994; Ruffert et al. 1997; Rosswog et al. 1999). Based on numerical simulations, the ejecta mass liberated, the kinetic energy and the velocities lie in the ranges of $10^{-4} \lesssim M_{\rm ej} \lesssim 10^{-2}\,{\rm M_\odot}$, $10^{49} \lesssim E \lesssim 10^{51}$ erg and $0.1 \lesssim \beta\Gamma \lesssim 0.3$, respectively (e.g., see Goriely et al. 2011; Hotokezaka et al. 2013; Bauswein et al. 2013; Piran et al. 2013; Wanajo et al. 2014; Grossman et al. 2014).

4.2. *The cocoon material*

As the GRB jet makes its way through the neutrino-driven or magnetically driven wind (previously ejected during the coalescence of the NS merger), it will deposit energy around its way. The energy deposited laterally will form a cocoon which may have an energy comparable to the electromagnetic emission created by the jet. Murguia-Berthier et al. (2014) studied the necessary conditions for a cocoon production as a function of the jet luminosity. The authors found that when the jet has a low or a high luminosity, a weak cocoon emission is expected. Nagakura et al. (2014) numerically showed that when a low-luminosity jet is considered, a hot cocoon confining the jet is formed. As soon as the relativistic jet reaches the shock-breakout material, the cocoon breakouts and expands along the jet's axis. Beyond the breakout material, the external pressure decreases abruptly, so the cocoon can accelerate and expand relativistically until it becomes transparent. Accelerated material from the cocoon fireball will continue moving in the jet's axis. It is worth mentioning that the significance of the cocoon also depends on the delay time between the merger and jet launching (Geng et al. 2019). The ejecta mass liberated in the cocoon, the kinetic energy and the velocities lie in the ranges of $10^{-6} \lesssim M_{\rm ej} \lesssim 10^{-4}\,{\rm M_\odot}$, $10^{47} \lesssim E \lesssim 10^{50.5}$ erg and $0.2 \lesssim \beta\Gamma \lesssim 10$, respectively (e.g., see Nagakura et al. 2014; Murguia-Berthier et al. 2014; Lazzati et al. 2017, 2018; Nakar and Piran 2017; Gottlieb et al. 2018).

4.3. *The shock breakout material*

The shock breakout material properties depend on the mass, radius and velocity of the merger remnant. Immediately after the coalescence occurs, a shock formed at the interface between the two NSs is initially ejected from the NS core to the NS crust at sub-relativistic velocities ($\beta_{\rm in} \simeq 0.25$ e.g., see Kyutoku et al. 2014; Metzger et al. 2015). Once the shock reaches half of the escape velocity, a fraction of the thermal energy is converted into kinetic energy and it can leave the merger (for details see Kyutoku et al. 2014; Fraija et al. 2019e). Numerical simulations indicate that the ejecta mass, the kinetic energy and the velocities lie in the ranges of $10^{-6} \lesssim M_{\rm ej} \lesssim 10^{-4}\,{\rm M_\odot}$, $10^{47} \lesssim E \lesssim 10^{50.5}$ erg and $\beta\Gamma \gtrsim 0.8$, respectively (e.g., see Kyutoku et al. 2014; Metzger et al. 2015).

4.4. *The disk wind ejecta*

The coalescence of the NS binary will finish in a tidal disruption, resulting in the formation of an accretion disk around the central remnant. The accretion disk will have a mass in the range of $10^{-3} \lesssim M_{\rm ej} \lesssim 0.3\,{\rm M_\odot}$ (Shibata and Taniguchi 2006; Hotokezaka et al. 2013), and due to a large source of thermal neutrinos (Popham et al. 1999), it could generate an outflow driven by neutrino heating similar to neutrino driven proto-NS winds in CC-SNe (Surman et al. 2008; Metzger et al. 2008). It represents a significant source of ejecta mass that might even dominate over other ejecta masses as suggested by Siegel and Metzger (2017). The ejecta mass, the kinetic energy

and the velocities lie in the ranges of $10^{-4} \lesssim M_{\rm ej} \lesssim 10^{-1.3}\,{\rm M_\odot}$, $10^{47} \lesssim E \lesssim 10^{50}$ erg and $0.03 \lesssim \beta\Gamma \lesssim 0.1$, respectively (e.g., see Dessart et al. 2009; Metzger and Fernández 2014; Fernández et al. 2015).

4.5. *Analysis of the multi-wavelength light curves*

Figure 7 shows the synchrotron and SSC light curves generated by the non-relativistic masses ejected from the coalescence of a NS binary such as the dynamical ejecta, the cocoon material, the shock breakout material and the wind ejecta.[5] The electromagnetic emission from the non-relativistic masses is shown as a bump at a timescale of $\geq 10^3$ days. In addition, we consider the synchrotron and SSC emission from an on-axis and off-axis relativistic jet with viewing angles of $\theta = 15°$, $30°$ and $60°$.[6] The light curves correspondent to the off-axis jet are plotted in accordance with the afterglow model introduced in Fraija et al. (2019d). The left-hand panels show the synchrotron light curves which correspond to (from top to bottom) radio (1.6 GHz), optical (1 eV) and X-ray (1 keV) bands, respectively, and the right-hand panels show the SSC light curves which correspond to (from top to bottom) gamma-ray fluxes at 100 keV, 10 GeV and 100 GeV, respectively. The coalescence of the two NSs launches significant non-relativistic masses with different velocities which will contribute at distinct timescales, frequencies and intensities. These ejecta masses interact with the circumstellar medium generating non-thermal emission. The predicted synchrotron fluxes generated from: i) the shock breakout material peak at timescales from hours to days, ii) the cocoon material peak at timescales from weeks to months, iii) the dynamical ejecta peak at years and iv) the disk wind ejecta peak at centuries. Similar timescales with different intensities are shown in the SSC light curves.

This figure shows that the afterglow emission originated from the deceleration of the on-axis relativistic jet would have to decrease so that the electromagnetic emission from the non-relativistic masses could be observed. Murguia-Berthier et al. (2014); Nagakura et al. (2014) estimated the necessary conditions for sGRB production in the coalescence of the NS binary. In the case that such conditions are not satisfied, a relativistic jet is not expected and the electromagnetic emission from the non-relativistic masses could be observed since early times.

Because the shock breakout material is described with a velocity of $\beta = 0.8$ (Metzger et al. 2015), the trans-relativistic regime introduced in Huang et al. (1998) is used. In this regime, the kinetic energy of the shock in the uniform-density medium is given by $E_{\rm K} = \frac{4\pi}{3}\sigma m_p c^2 \beta^2 \Gamma^2 r^3 n$ (Blandford and McKee 1976) with $\sigma = 0.73 - 0.38\beta$ and $r \approx \beta t$ (Huang et al. 1998). Taking into account this regime, the equivalent kinetic energy distribution will be $E = \tilde{E}(\beta\Gamma)^{-\alpha}$, and the deceleration time becomes

$$t_{\rm dec} = \left(\frac{3}{4\pi\sigma m_p c^5}\right)^{\frac{1}{3}} (1+z) A_0^{-\frac{1}{3}} \tilde{E}^{\frac{1}{3}} \beta^{-\frac{\alpha+5}{3}} \Gamma^{-\frac{\alpha+2}{3}}. \quad (20)$$

In the trans-relativistic regime, the velocity obtained from eq. (20) is used to find the synchrotron and SSC quantities. It is worth noting that in the limit $\Gamma \to 1$, the equations (8) and (10) are recovered.

In the "deep Newtonian" regime the Lorentz factor of the lowest-energy electrons is $\gamma_{\rm m} \simeq 2$ (Sironi and Giannios 2013; Kathirgamaraju et al. 2016; Margalit and Piran 2020). Using eq. (11), the deceleration time in this regime becomes

$$t_{\rm DN} \simeq 2 \times 10^5\,{\rm days}\,\left(\frac{1+z}{1.022}\right)\epsilon_{\rm e,-1}^{\frac{\alpha+5}{6}} A_0^{-\frac{1}{3}} \tilde{E}_{51}^{\frac{1}{3}}, \quad (21)$$

---

[5] The pair of values ($\tilde{E} = 10^{50}$ erg; $\beta = 0.2$) is used for the dynamical ejecta, (10^{48} erg; 0.3) for the cocoon material, ($10^{48.5}$ erg; 0.8) for the shock breakout material and (10^{50} erg; 0.07) for the wind. All light curves are shown for $n = 1\,{\rm cm^{-3}}$, $\alpha = 3$, $\epsilon_{\rm B} = 10^{-2}$, $\epsilon_{\rm e} = 10^{-1}$, $p = 3.2$ and $d_z = 100\,{\rm Mpc}$.

[6] The values of $\tilde{E} = 10^{50}$ erg, $\epsilon_{\rm B} = 10^{-2}$, $\epsilon_{\rm e} = 10^{-1}$, $n = 10^{-2}\,{\rm cm^{-3}}$, $p = 2.2$ and $d_z = 100\,{\rm Mpc}$ are used for the relativistic jet.

and the velocity of the ejecta is $\beta \simeq 0.05$. In this case the characteristic break frequency evolves as $\nu_{\rm m}^{\rm syn} \propto t^{-\frac{3}{\alpha+5}}$, the spectral peak flux density as $F_{\nu,\max}^{\rm syn} \propto t^{\frac{3(\alpha-1)}{\alpha+5}}$ and the predicted flux evolves as $F_\nu = F_{\nu,max}^{\rm syn} \left(\frac{\nu}{\nu_{\rm m}}\right)^{-\frac{p-1}{2}} \propto t^{-\frac{3(1+p-\alpha)}{2(\alpha+5)}} \nu^{-\frac{p-1}{2}}$ for $\nu_{\rm m}^{\rm syn} < \nu < \nu_{\rm c}^{\rm syn}$. Therefore, it is worth noting that due to the range of velocities considered ($0.07 \leq \beta \leq 0.8$) and the deceleration time scales, the "deep Newtonian" regime is only required for the wind ejecta. The coalescence of the NS binaries launches significant non-relativistic masses with different velocities which will contribute at distinct timescales, frequencies and intensities. These non-relativistic masses interact with the circumstellar medium generating non-thermal electromagnetic emission. We calculated the expected gamma-ray, X-ray, optical and radio fluxes via SSC and synchrotron emission from electrons accelerated in the forward shocks. These electromagnetic signatures at different timescales and frequencies would be similar to those detected around SNe for a uniform density medium and also be present together with the GW detections.

5. THE NON-RELATIVISTIC MASSES EJECTED FROM THE CORE-COLLAPSES OF DYING MASSIVE STARS

The origin of lGRBs is widely accepted to be connected to the death of massive stars leading to SNe, where the afterglow emission from bursts is detected together with a type Ic SN with broad lines (e.g., see Woosley and Janka 2005; Cano et al. 2017). Sub-energetic GRBs are believed to be quasi-spherical explosions dominated by the non-relativistic ejecta mass. The non-relativistic material carries $\approx 99.9\%$ of the explosion energy, and the mildly relativistic ejecta only $\approx 0.1\%$. The energy carried by the non-relativistic ejecta is similar to that exhibited by the sub-energetic bursts and comparable to the most energetic type Ib/c SNe. Margutti et al. (2014) showed the equivalent kinetic energy profile as a function of ejecta mass velocity in the non-relativistic and relativistic regime of ordinary type Ibc SNe, engine-driven SNe (E-SNe), sub-E GRBs and relativistic SNe. The velocity of the ejecta mass was divided into the non-relativistic phase $0.02 \lesssim \beta \lesssim 0.3$, mildly relativistic $\Gamma\beta \approx 0.6 - 0.8$ and relativistic $2 \lesssim \beta \lesssim 20$. It is worth noting that broadened lines in their spectra, indicate that a diverse range of materials with distinct non-relativistic expansion velocities are present (e.g., $O_{\rm II}$, $N_{\rm II}$, $S_{\rm II}$, etc; Modjaz et al. 2020).
Depending on the range of values in the observables such as luminosity, duration and bulk Lorentz factor, lGRBs could be successful or choked (e.g., see MacFadyen et al. 2001; Mészáros and Waxman 2001; Fraija 2014; Sobacchi et al. 2017; Bromberg et al. 2011). For instance, choked GRBs might be more frequent than successful ones, only limited by the ratio of SNe (types Ib/c and II) to lGRB rates (Totani 2003; Ando and Beacom 2005). Some SN of type Ic-BL not connected with GRBs have been suggested to arise from events such as off-axis GRBs or failed jets (e.g., see Izzo et al. 2019, 2020; Beniamini et al. 2020). This is the case of the failed burst GRB 171205A, which besides being associated to SN 2017iuk, exhibited material with high expansion velocities $\beta \sim 0.4$ interpreted as mildly relativistic cocoon material (Izzo et al. 2019). Izzo et al. (2020) found that the X-ray observations from the nearby SN 2020bvc were consistent with the afterglow emission generated by an off-axis jet with viewing angle of 23° when it decelerated in a circumburst medium with a density profile with k = 1.5.

Figure 8 shows the synchrotron and SSC light curves when the non-relativistic ejecta mass decelerates in a stratified wind medium. The light curves correspondent to the off-axis jet are plotted in accordance with the afterglow model introduced in Fraija et al. (2019d). The left-hand panels show the synchrotron light curves which correspond to (from top to bottom) radio (1.6 GHz), optical (1 eV) and X-ray (1 keV) bands, respectively, and the right-hand panels show the SSC light curves which correspond to (from top to bottom) gamma-ray fluxes at 100 keV, 10 GeV and 100 GeV, respectively. This figure shows that the afterglow emission originated from deceleration of the on-axis relativistic jet would have to decrease so that the afterglow emission from the non-relativistic ejecta could be observed.
In our model, the afterglow emission from the non-relativistic ejecta in the radio band is observed as a flaring event while the afterglow from the optical and X-ray bands is seem as tails. This figure displays that, depending on the parameters and the viewing angle, the afterglow emission from the non-relativistic ejecta can be detected at early times. Similarly, when the jet is choked, the afterglow emission from the non-relativistic ejecta can be observed at early times.
The way to distinguish the electromagnetic emission between the non-relativistic ejecta and the relativistic jet, for example, could be done through the evolution of the synchrotron flux derived in eqs. (5) and (7) for the coasting phase and in eqs. (15) and (19) for deceleration phase.
In order to analyze the mildly relativistic SNe with velocities in the range of $\Gamma\beta \approx 0.6 - 0.8$ as SN 2012ap, the synchrotron process in the trans-relativistic regime as discussed in Section 4.5 for the shock breakout material through eq. (20) would be required.

6. THE NON-RELATIVISTIC EJECTA MASS AND THE KILONOVA AFTERGLOW IN GW170817 AND S190814bv

The coalescence of NS-NS and BH-NS binaries is the most natural candidate for the radiation of continuous GWs (e.g., see Metzger 2017). These coalescences are predicted to be accompanied by a kilonova (Li and Paczyński 1998; Rosswog 2005; Metzger et al. 2010; Kasen et al. 2013; Metzger 2017). This transient is expected to be observed in near-IR/optical/UV bands throughout a timescale from days to weeks.
All coalescence of NS-NS, and only a fraction of BH-NS binaries can unbind at least some extremely neutron-rich material which is able to form heavy r-process nuclei. This Lanthanide-bearing matter with high opacity is associated with the "red" kilonova which is located inside the tidal tail in the equatorial plane. The "blue" kilonova is associated with the low-opacity ejecta free of Lanthanide group elements which is located in the polar regions (Metzger and Fernández 2014; Perego et al. 2014; Wanajo et al. 2014; Miller et al. 2019). While the "red" kilonova is associated with a slow ejecta material $\beta \simeq 0.1$, the "blue" KN is characterized by being ejected with a faster velocity $\beta \simeq 0.3$.
In the following section, we give a brief introduction of multi-wavelength observations, and also constrain the parameter space of the faster "blue" kilonova afterglow in GW170817 and the KN afterglow possibly generated by the coalescence of a BH-NS system in S190814bv.

6.1. *Multi-wavelength observations*
6.1.1. *GW170817*

On 2017 August 17, a GW signal (GW170817; Abbott et al. 2017a,b) together with a faint gamma-ray counterpart (GRB 170817A; Goldstein et al. 2017; Savchenko et al. 2017) and kilonova emission were detected (Soares-Santos et al. 2017; Coulter et al. 2017; Cowperthwaite et al. 2017; Tanvir et al. 2017; Smartt et al. 2017; Gottlieb et al. 2018), for the first time, identifying the coalescence of a binary NS system. GRB 170817A exhibited observational evidence for extended emission in X-ray (Troja et al. 2017b; Margutti et al. 2018; D'Avanzo et al. 2018; Alexander et al. 2018), optical (Lyman et al. 2018; Margutti et al. 2018) and radio (Abbott et al. 2017b; Mooley et al. 2018b; Dobie et al. 2018; Troja et al. 2017a) bands. About 11 hours post-merger, the optical transient coincident with the quiescent galaxy NGC 4993 at a distance of 40 Mpc ($z \approx 0.01$) was associated with the kilonova (AT2017gfo; Soares-Santos et al. 2017; Coulter et al. 2017; Cowperthwaite et al. 2017;

Tanvir et al. 2017; Smartt et al. 2017; Gottlieb et al. 2018).
The temporarily extended X-ray and radio emission was fitted with a simple PL function which increased steadily as $\sim t^{0.8}$ (Margutti et al. 2018; Mooley et al. 2018b) to reach its maximum value around ~ 140 days post-merger, then decreased subsequently as t^{-p} with $p \approx 2.2$. A variety set of off-axis jet models (with an opening angle $\lesssim 5°$ and a viewing angle $\lesssim 28°$; Abbott et al. 2017a; Sobacchi et al. 2017; Evans et al. 2017; Haggard et al. 2017; Mandel 2018) such as top-hat jets (Troja et al. 2017b; Margutti et al. 2018; Alexander et al. 2018, 2017; Fraija et al. 2019a,b), radially stratified outflows (Mooley et al. 2018b; Fraija et al. 2019e; Hotokezaka et al. 2018) and structured outflows (Kasliwal et al. 2017b; Lamb and Kobayashi 2017; Lazzati et al. 2018; Mooley et al. 2018a; Fraija et al. 2019d; Gottlieb et al. 2018; Kathirgamaraju et al. 2018) were proposed to describe the temporarily extended electromagnetic emissions.

In order to constrain the KN afterglow, we use the data points displayed in Fraija et al. (2019d) and complemented with those presented by Fong et al. (2019) in the optical F606W filter, and by Hajela et al. (2019) and Troja et al. (2020b) in the energy range of 0.3 - 10 keV. Table 2 shows the latest Chandra afterglow observations in units of $\mathrm{erg\,cm^{-2}\,s^{-1}}$ (0.3 - 10 keV) and mJy normalized at 1 keV. The data points in $\mathrm{erg\,cm^{-2}\,s^{-1}}$ are taken from Hajela et al. (2019) and Troja et al. (2020b).

6.1.2. *S190814bv*

On 2019 August 14 the LIGO and Virgo interferometer detected a GW signal (S190814bv; LIGO Scientific Collaboration and Virgo Collaboration 2019a,b) associated with a NS-BH merger located at a distance of $267 \pm 52\,\mathrm{Mpc}$ (Gomez et al. 2019). Immediately, S190814bv was followed up by a large observational campaign that covered a large fraction of the electromagnetic spectrum (e.g., see Andreoni et al. 2020; Dobie et al. 2019; Watson et al. 2020; Ackley et al. 2020; Vieira et al. 2020). No counts were registered in any wavelengths and upper limits were reported.

Using the MegaCam instrument on the Canada-France-Hawaii Telescope (CFHT), Ackley et al. (2020) placed optical upper limits on the presence of any counterpart and discussed the implications for the KN possibly being generated by the coalescence of the BH-NS system. They excluded a KN with large ejecta mass $\gtrsim 0.1 M_\odot$, and, considering off-axis jet models, the authors ruled out circumstellar densities $\gtrsim 1\,\mathrm{cm^{-3}}$ for typical values of microphysical parameters. Vieira et al. (2020) reported observational constraints on the near-infrared (IR) and optical with the ElectromagNetic counterparts of GRAvitational wave sources at the VERy Large Telescope (ENGRAVE). They constrained the KN ejecta mass to be $\lesssim 1.5 \times 10^{-2}\,M_\odot$ for a "blue" KN, and $\lesssim 4 \times 10^{-2}\,M_\odot$ for a "red" KN. Gomez et al. (2019) reported a Galaxy-targeted search for the optical emission with the Magellan Baade 6.5 m telescope and ruled out the on-axis typical jet of sGRBs. Dobie et al. (2019) presented upper limits in the radio band with the Australian Square Kilometre Array Pathfinder (ASKAP) and constrained the circumstellar density and inclination angle of the system.

In order to constrain the KN afterglow, the upper limits on radio at 935 MHz (Dobie et al. 2019), near-IR and optical at the $\mathrm{K_s}$ and R filters (Ackley et al. 2020) and X-rays at 1 keV (Evans et al. 2019) are considered.

6.2. *Constraining the KN afterglow*

Figure 9 shows the multi-wavelength observations of GW170817 and S190814bv at the radio, optical and X-ray bands with the synchrotron light curves shown in Figure 1 which are generated by the deceleration of the non-relativistic ejecta in the homogeneous-density medium. Each colour of the synchrotron light curves corresponds to the set of parameter values reported in Section 3. In addition, we include the synchrotron light curves at 3 GHz. The data points with the upper limits in black correspond to the observations performed for GW170817 and the upper limits in gray correspond to S190814bv. Concerning GW170817, the upper panels show the

radio observations at 3 GHz (left) and 6 GHz (right), and the lower panels show the optical observations at the F606W filter and the X-ray observations at 1 keV (right). We include the upper limits collected from S190814bv on radio at 935 MHz (top left), near-IR and optical at $\mathrm{K_s}$ and R filters (bottom left), respectively, and X-rays at 1 keV (bottom right).

As indicated in Section 3, the synchrotron light curves are shown for different values of p and α, and the same values of A_0, ϵ_e and ϵ_B. Therefore, any variation of these parameters will increase or decrease the intensity of the observed flux in radio, optical and X-ray bands. Given the multiwavelength observations of GW170817 and S190814bv, we constrain the parameter space of A_0, α, ϵ_e and ϵ_B as a function of the velocity β. In order to compare the density parameter of the uniform density medium A_0 found in this model with others, hereafter we use the usual notation n for A_0.

6.2.1. *GW170817*

Figure 10 shows the multi-wavelength observations of GW170817 and the parameter space allowed with the synchrotron model presented in this work. The upper left-hand panel shows the multiwavelength data points of GW170817 with the best-fit curves obtained with the structured jet model presented in Fraija et al. (2019d) and a possible synchrotron contribution emitted by the deceleration of the non-relativistic ejecta. The light curves are exhibited in radio (3 and 6 GHz), optical (at the F606W filter) and X-ray (1 keV) bands. The upper right-hand panel and the lower panels show the allowed parameter space of the uniform density of the circumstellar medium (n), the velocity of the non-relativistic ejecta (β), the index of the PL distribution (α) and the microphysical parameters (ϵ_e and ϵ_B) for the fiducial energy $\tilde{E}_\mathrm{K} = 10^{49}$ erg (Hotokezaka and Piran 2015; Fraija et al. 2019d), and the spectral index $p = 2.15$ (Hajela et al. 2019; Lazzati et al. 2018). We use the value of the microphysical parameter $\epsilon_\mathrm{e} = 10^{-1}$ and $\alpha = 3.0$ in the upper left-hand panel, $\epsilon_\mathrm{B} = 10^{-3}$ and $\alpha = 3.0$ in the lower right-hand panel and $\epsilon_\mathrm{e} = 10^{-1}$ and $\epsilon_\mathrm{B} = 10^{-3}$ in the lower left-hand panel. The allowed parameter spaces are below the relevant colored contours and obtained using the data points in radio, optical and X-ray as upper limits. In order to illustrate the synchrotron light curves generated by the deceleration of the non-relativistic ejecta as shown in the upper left-hand panel, we consider a set of values from the parameter space.

Taking into account the velocity of $\beta = 0.3$ and $\alpha = 3$ which are the reported values for the "blue" KN (Metzger 2019), the ranges of parameters allowed in our model ($5 \times 10^{-2} \lesssim \epsilon_\mathrm{e} \lesssim 0.2$, $10^{-3} \lesssim \epsilon_\mathrm{B} \lesssim 10^{-2}$, $10^{-3} \lesssim n \lesssim 10^{-2}\,\mathrm{cm^{-3}}$) are similar to those reported from the description of the multi-wavelegth observations by deceleration of relativistic structured/top-hat outflows. For instance, the values $\epsilon_\mathrm{e} = 0.15$, $\epsilon_\mathrm{B} = 5 \times 10^{-3}$, and $n = 4 \times 10^{-3}\,\mathrm{cm^{-3}}$ for $\beta \approx 0.3$ strongly agree with the values reported in Hajela et al. (2019).

6.2.2. *S190814bv*

Figure 11 shows the multi-wavelength upper limits of S190814bv and the parameter space ruled out with the synchrotron model presented in this work. The upper left-hand panel shows the multi-wavelength upper limits and the light curves in X-ray, optical, near-IR and radio bands at 1 keV, R-band, $\mathrm{K_s}$-band and 943 MHz, respectively. In order to rule out the parameters n, α, β, ϵ_e and ϵ_B, these upper limits are considered. The ruled out regions are above the relevant colored contours. The upper right-hand and lower panels show the parameter spaces which are ruled out in our model for the fiducial energy $\tilde{E} = 10^{50}$ erg and the spectral index $p = 2.6$. We use the value of the microphysical parameters $\epsilon_\mathrm{e} = 10^{-1}$ and $\alpha = 3$ in the upper right-hand panel, $\epsilon_\mathrm{B} = 10^{-2}$ and $\alpha = 3$ in the lower left-hand panel and $\epsilon_\mathrm{e} = 10^{-1}$ and $\epsilon_\mathrm{B} = 10^{-2}$ in the lower right-hand panel. These panels display that a uniform-density $n \gtrsim 0.6\,\mathrm{cm^{-3}}$ is ruled out in our model for the parameters in the range of $3 \lesssim \alpha \lesssim 5.2$, $0.1 \lesssim \epsilon_e \lesssim 0.9$ and $10^{-2} \lesssim \epsilon_B \lesssim 0.1$ for $\beta > 0.33$. In order to

illustrate the synchrotron light curves in the X-ray, optical, near-IR and radio bands generated by the deceleration of the non-relativistic ejecta as shown in the upper panel, we consider a set of parameters selected from the lower panels ($\beta = 0.39$, $\alpha = 3$, $\epsilon_B = 0.1$, $\epsilon_e = 0.3$ and $n = 1\,\mathrm{cm}^{-3}$). In this panel it can be observed that the predicted radio flux is above the upper limit at $37\,\mathrm{days}$.

The value of the uniform-density medium ruled out in our model is consistent with the value of densities derived by Dobie et al. (2019); Ackley et al. (2020); Gomez et al. (2019) using distinct off-axis jet models. Further observations on timescales of years post-merger are needed to derive tighter constraints and therefore, to increase (decrease) the parameter space ruled out (allowed) in our model. The value allowed of the power index $\alpha = 3$ in our theoretical model agrees with the values found in numerical simulations (e.g., see Bauswein et al. 2013) and used for describing the KN emission (Metzger 2017, 2019).

6.3. *A diversity range of KN features*

Disentangling the properties of KNe is an important point especially given the association of sGRBs with the GWs. The detection of GRB 170817A, AT 2017gfo and GW170817 has paved the way on the nature of sGRBs as the coalescence of NS mergers. The evident KN signature in GW170817 provided the chance to estimate their detectability in sGRBs and the variability in their features. Since sGRBs are usually discovered via detection of the γ-ray prompt emission from the relativistic jet, they are typically observed where the afterglow is brighter and thus most probably obscure the KN. This emission with its more isotropic component is easier to be seen at angles far away from the sGRB jet (Metzger and Berger 2012). Despite this, it has been possible to determine only four claimed KNe with different features to AT 2017gfo. SGRBs associated to the claimed KNe are GRB 050709 (Jin et al. 2016), GRB 060614 (Yang et al. 2015), GRB 130603B (Tanvir et al. 2013; Berger et al. 2013) and GRB 160821B (Kasliwal et al. 2017a; Troja et al. 2019). For instance, while KN associated to GRB 060614 is much brighter (2 or 3 times) than the interpolated KN model fit at the time of the observations, KN associated to GRB 160821B is less bright than AT 2017gfo.

Gompertz et al. (2018) analyzed a sample of 23 short nearby ($z \leq 0.5$) GRBs to compare the optical and near-IR light curves with AT 2017gfo. They considered short bursts, following the historical classification, the ones with $T_{90} \leq 2$ s and also the class of the sGRBs with extended emission (Norris and Bonnell 2006; Dainotti et al. 2010, 2016, 2017a,b). This comparison enables to characterize their diversity in terms of their brightness distribution. Gompertz et al. (2018) found that for four sGRBs: 050509B, 051210, 061201, and 080905A, a KN of the same brightness of AT 2017gfo could have been observed. For these bursts, deep $3\,\sigma$ upper limits, two times or more dimmer than the detections of AT 2017gfo at comparable rest-frame times, seem to exclude the presence of a KN like AT 2017gfo. In each case, a KN like AT 2017gfo could have been detected if it had been present. The authors also found that the afterglows in GRBs 150424A, 140903A and 150101B were too bright for an AT 2017gfo-like KN to be detected. Finally, they reported that the host galaxies of sGRBs 061006, 071227 and 170428A were to bright, and in six bursts there was no sufficient constraining observations regarding the presence of KN.

Covering 14 years of operations with Swift, Dichiara et al. (2020) presented a systematic search for sGRBs in the local Universe. The authors found no events at a distance $\lesssim 100\,\mathrm{Mpc}$ and four candidates located at $\lesssim 200\,\mathrm{Mpc}$. They derived, in each case, constraining optical upper limits on the onset of a "blue" KN, implying low mass ejecta ($\lesssim 10^{-3}\,M_\odot$).

The bursts that exclude the evidence of a KN similar to AT 2017gfo by several magnitudes together with the properties of previously claimed KNe in sGRBs support the hypothesis that a significant diversity exist in the properties of KN drawn from the coalescence of compact object mergers. Therefore, a diversity range of KN features leads a wide parameter space of velocities, PL indices, masses, mi-

crophysical parameters and circumburst densities as discussed in this section.

Continuous energy injection by the central engine on the afterglow can produce a refreshed shock, and modifies the dynamics leading to rich radiation signatures. The problem of additional energy injection from the central engine has been studied by some authors (e.g. see Gao et al. 2013a; Troja et al. 2020b). Although this scenario is beyond the scope of the current paper, these signatures, in our model, would usually appear in timescales from weeks to hundred of days. In a forthcoming paper, we will present a detailed analysis of a refreshed shock in the energy injection scenario.

7. DISCUSSION AND SUMMARY

We derived, based on analytic arguments, the dynamics of deceleration of a non-relativistic ejecta in a circumstellar medium with a density profile $A_k r^{-k}$ with k $= 0$, 1, 1.5, 2 and 2.5 that covers short and long GRB progenitors. While the uniform-density medium ($k = 0$) is expected in the coalescence of binary compact objects and in CC-SNe, the stratified medium ($1 \leq k \leq 2.5$) is only connected with the death of massive stars with different mass-loss evolution at the end of their lives. Taking into account that electrons are accelerated during the forward shocks with a spectral index in the range $2.2 \leq p \leq 3.2$, we calculated the synchrotron and SSC light curves in the fast- and slow-cooling regime during the coasting and the deceleration phase. During the coasting phase we considered velocities in the range of $0.07 \leq \beta \leq 0.8$ and during the deceleration phase we assumed a PL velocity distribution $\propto \beta^{-\alpha}$ with $3 \leq \alpha \leq 5.2$ for a generic source located at $100\,\mathrm{Mpc}$.

We showed the predicted synchrotron light curves in radio at 6 GHz, optical at 1 eV and X-rays at 1 keV for typical values of GRB afterglows. All the light curves peak on timescales from several months to a few years, similar to those observed in some SNe such as SN2014C and SN2016aps. However, if the ejecta mass is extremely energetic or decelerates in a very dense medium, a peak in the light curve could be expected in weeks.

We showed that when the non-relativistic ejecta decelerates in a uniform density medium a flattening or rebrightening in the light curve is expected, and when this ejecta decelerates in a stratified medium the rebrightening in the light curves is not so evident. Therefore, a flattening or rebrightening at timescales from months to years in the light curve together with GW detection would be associated with the deceleration of a non-relativistic ejecta launched during the coalescence of a binary compact object. Otherwise, we showed that an observed flux that gradually decreases on timescales from months to years could be associated with the deceleration of a non-relativistic ejecta launched during the death of a massive star with different mass-loss evolution at the end of its life.

The coalescence of the NS binaries launches significant non-relativistic masses with different velocities which will contribute at distinct timescales, frequencies and intensities. These ejecta masses (the dynamical ejecta, the cocoon material, the shock breakout material and the wind ejecta) interact with the circumstellar medium generating non-thermal emission. The shock breakout material peaks at timescales from hours to days, the cocoon material peaks at timescales from weeks to months, the dynamical ejecta peaks at years and the disk wind ejecta peaks at centuries. We calculated the expected gamma-ray, X-ray, optical and radio fluxes via SSC and synchrotron emission from electrons accelerated in the forward shocks. These electromagnetic signatures at different timescales and frequencies would be similar to those detected around SNe for a uniform density medium and also be present together with the GW detections.

We showed that variations in the density parameter could be observed more easily i) in the radio than in the X-ray light curve, ii) in a stratified than in a uniform density medium and iii) for larger values of α. Therefore, a transition phase from stellar-wind to uniform-density medium is more noticeable in radio than X-ray bands.

We showed that, in the case of a failed or an off-axis GRB, the non-thermal emission generated by the deceleration of non-relativistic ejecta could be detected at early times. In the case of an on-axis GRB, the afterglow emission originated from deceleration of the relativistic jet would have to decrease substantially so that the afterglow emission from the non-relativistic ejecta could be observed. In addition, we gave an important tool to distinguish the afterglow emission among the non-relativistic ejecta from the relativistic jet through the evolution of the synchrotron flux derived in eqs. (5) and (7) for the coasting phase and in eqs. (15) and (19) for the deceleration phase.

We computed the predicted SSC light curves from the deceleration of the non-relativistic ejecta mass for a density profile with $k = 0, 1, 1.5, 2$ and 2.5. The effect of the extragalactic background light (EBL) absorption modelled in Franceschini and Rodighiero (2017) was assumed. We showed that, when the non-relativistic ejecta decelerates in a uniform density medium, a flattening or rebrightening in the light curve is expected, and when, this ejecta decelerates in a stratified medium, the rebrightening in the light curves is not so evident. Similarly, we showed that the SSC flux is less sensitive to changes in the density parameter for higher frequencies than for lower ones and is more sensitive to the density parameter for larger values of k and α.

In particular, using the multi-wavelength observations and upper limits of GW170817 and S190814bv, we constrained the parameter space of the uniform density of the circumstellar medium, the velocity of the non-relativistic ejecta, the index of the PL distribution and the microphysical parameters. In the case of GW170817, we found similar values to those reported from the description of the multi-wavelength observations by the deceleration of relativistic structured/top-hat outflows for typical values of KN ejecta mass $\beta \approx 0.3$ and $\alpha = 3$ (Metzger 2017, 2019). Therefore, we conclude that the KN afterglow scenario can be used to constrain the afterglow parameters of relativistic structured/top-hat outflows. In particular, the values of $\epsilon_e = 0.15$, $\epsilon_B = 5 \times 10^{-3}$, and $n = 4 \times 10^{-3}\,\mathrm{cm}^{-3}$ strongly agree with the values reported in Hajela et al. (2019). For the case of S190814bv, we found that the value of the uniform-density medium ruled out in our model is consistent with the value of density derived by Dobie et al. (2019); Ackley et al. (2020) and Gomez et al. (2019) using distinct off-axis jet models. Further observations on timescales of years post-merger are needed to derive tighter constraints and therefore, to increase (decrease) the parameter space ruled out (allowed) in our model. The value allowed of the power index $\alpha = 3$ in our theoretical model agrees with the values found in numerical simulations (e.g., see Bauswein et al. 2013) and used for describing the KN emission (Metzger 2017, 2019).

REFERENCES

Abbott, B. P., Abbott, R., Abbott, T. D., and et al. (2017a). Gw170817: Observation of gravitational waves from a binary neutron star inspiral. Phys. Rev. Lett., 119:161101.

Abbott, B. P., Abbott, R., Abbott, T. D., and et al. (2017b). Multi-messenger observations of a binary neutron star merger. The Astrophysical Journal Letters, 848(2):L12.

Ackley, K., Amati, L., Barbieri, C., Bauer, F. E., Benetti, S., Bernardini, M. G., and et al. (2020). Observational constraints on the optical and near-infrared emission from the neutron star-black hole binary merger S190814bv. arXiv e-prints, page arXiv:2002.01950.

Alexander, K. D., Berger, E., Fong, W., Williams, P. K. G., Guidorzi, C., Margutti, R., Metzger, B. D., Annis, J., Blanchard, P. K., Brout, D., Brown, D. A., Chen, H.-Y., Chornock, R., Cowperthwaite, P. S., Drout, M., Eftekhari, T., Frieman, J., Holz, D. E., Nicholl, M., Rest, A., Sako, M., Soares-Santos, M., and Villar, V. A. (2017). The Electromagnetic Counterpart of the Binary Neutron Star Merger LIGO/Virgo GW170817. VI. Radio Constraints on a Relativistic Jet and Predictions for Late-time Emission from the Kilonova Ejecta. ApJ, 848:L21.

Alexander, K. D., Margutti, R., Blanchard, P. K., Fong, W., Berger, E., Hajela, A., and et. (2018). A Decline in the X-Ray through Radio Emission from GW170817 Continues to Support an Off-axis Structured Jet. ApJ, 863(2):L18.

Ando, S. and Beacom, J. F. (2005). Revealing the Supernova Gamma-Ray Burst Connection with TeV Neutrinos. Phys. Rev. Lett., 95(6):061103.

Andreoni, I., Goldstein, D. A., Kasliwal, M. M., Nugent, P. E., Zhou, R., Newman, J. A., and et al. (2020). GROWTH on S190814bv: Deep Synoptic Limits on the Optical/Near-infrared Counterpart to a Neutron Star?Black Hole Merger. ApJ, 890(2):131.

Arcavi, I., Hosseinzadeh, G., Howell, D. A., McCully, C., Poznanski, D., Kasen, D., Barnes, J., Zaltzman, M., Vasylyev, S., Maoz, D., and Valenti, S. (2017). Optical emission from a kilonova following a gravitational-wave-detected neutron-star merger. Nature, 551(7678):64–66.

Barniol Duran, R. and Giannios, D. (2015). Radio rebrightening of the GRB afterglow by the accompanying supernova. MNRAS, 454(2):1711–1718.

Barniol Duran, R., Nakar, E., Piran, T., and Sari, R. (2015). The afterglow of a relativistic shock breakout and low-luminosity GRBs. MNRAS, 448(1):417–428.

Barthelmy, S. D., Cannizzo, J. K., Gehrels, N., Cusumano, G., Mangano, V., O'Brien, P. T., and et al. (2005). Discovery of an Afterglow Extension of the Prompt Phase of Two Gamma-Ray Bursts Observed by Swift. ApJ, 635:L133–L136.

Bauswein, A., Goriely, S., and Janka, H. T. (2013). Systematics of Dynamical Mass Ejection, Nucleosynthesis, and Radioactively Powered Electromagnetic Signals from Neutron-star Mergers. ApJ, 773(1):78.

Beniamini, P., Granot, J., and Gill, R. (2020). Afterglow light curves from misaligned structured jets. MNRAS, 493(3):3521–3534.

Berger, E., Fong, W., and Chornock, R. (2013). An r-process Kilonova Associated with the Short-hard GRB 130603B. ApJ, 774(2):L23.

Björnsson, C.-I. and Fransson, C. (2004). The X-Ray and Radio Emission from SN 2002ap: The Importance of Compton Scattering. ApJ, 605(2):823–829.

Blandford, R. D. and McKee, C. F. (1976). Fluid dynamics of relativistic blast waves. Physics of Fluids, 19:1130–1138.

Blondin, J. M., Lundqvist, P., and Chevalier, R. A. (1996). Axisymmetric circumstellar interaction in supernovae. ApJ, 472:257–266.

Bloom, J. S., Kulkarni, S. R., Djorgovski, S. G., Eichelberger, A. C., Côté, P., and et al. (1999). The unusual afterglow of the γ-ray burst of 26 March 1998 as evidence for a supernova connection. Nature, 401(6752):453–456.

Bromberg, O., Nakar, E., and Piran, T. (2011). Are Low-luminosity Gamma-Ray Bursts Generated by Relativistic Jets? ApJ, 739(2):L55.

Cano, Z., Wang, S.-Q., Dai, Z.-G., and Wu, X.-F. (2017). The Observer's Guide to the Gamma-Ray Burst Supernova Connection. Advances in Astronomy, 2017:8929054.

Chevalier, R. A. (1982). Self-similar solutions for the interaction of stellar ejecta with an external medium. ApJ, 258:790–797.

Chevalier, R. A. (1984). The circumstellar interaction model for the radio emission from a Type I supernova. ApJ, 285:L63–L66.

Chevalier, R. A. and Fransson, C. (2006). Circumstellar Emission from Type Ib and Ic Supernovae. ApJ, 651(1):381–391.

Chevalier, R. A., Fransson, C., and Nymark, T. K. (2006). Radio and X-Ray Emission as Probes of Type IIP Supernovae and Red Supergiant Mass Loss. ApJ, 641(2):1029–1038.

Chevalier, R. A. and Irwin, C. M. (2011). Shock Breakout in Dense Mass Loss: Luminous Supernovae. ApJ, 729(1):L6.

Coulter, D. A., Foley, R. J., Kilpatrick, C. D., Drout, M. R., Piro, A. L., Shappee, B. J., Siebert, M. R., Simon, J. D., Ulloa, N., Kasen, D., Madore, B. F., Murguia-Berthier, A., Pan, Y. C., Prochaska, J. X., Ramirez-Ruiz, E., Rest, A., and Rojas-Bravo, C. (2017). Swope Supernova Survey 2017a (SSS17a), the optical counterpart to a gravitational wave source. Science, 358(6370):1556–1558.

Cowperthwaite, P. S., Berger, E., Villar, V. A., Metzger, B. D., Nicholl, M., Chornock, R., and et al. (2017). The Electromagnetic Counterpart of the Binary Neutron Star Merger LIGO/Virgo GW170817. II. UV, Optical, and Near-infrared Light Curves and Comparison to Kilonova Models. ApJ, 848(2):L17.

Dai, Z. G. and Lu, T. (1999). The Afterglow of GRB 990123 and a Dense Medium. ApJ, 519:L155–L158.

Dainotti, M. G., Hernandez, X., Postnikov, S., Nagataki, S., O'brien, P., Willingale, R., and Striegel, S. (2017a). A Study of the Gamma-Ray Burst Fundamental Plane. ApJ, 848(2):88.

Dainotti, M. G., Nagataki, S., Maeda, K., Postnikov, S., and Pian, E. (2017b). A study of gamma ray bursts with afterglow plateau phases associated with supernovae. A&A, 600:A98.

Dainotti, M. G., Postnikov, S., Hernandez, X., and Ostrowski, M. (2016). A Fundamental Plane for Long Gamma-Ray Bursts with X-Ray Plateaus. ApJ, 825(2):L20.

Dainotti, M. G., Willingale, R., Capozziello, S., Fabrizio Cardone, V., and Ostrowski, M. (2010). Discovery of a Tight Correlation for Gamma-ray Burst Afterglows with "Canonical" Light Curves. ApJ, 722(2):L215–L219.

D'Avanzo, P., Campana, S., Salafia, O. S., Ghirland a, G., Ghisellini, G., Melandri, A., Bernardini, M. G., Branchesi, M., Chassande-Mottin, E., Covino, S., D'Elia, V., Nava, L., Salvaterra, R., Tagliaferri, G., and Vergani, S. D. (2018). The evolution of the X-ray afterglow emission of GW 170817/ GRB 170817A in XMM-Newton observations. A&A, 613:L1.

Davies, M. B., Benz, W., Piran, T., and Thielemann, F. K. (1994). Merging Neutron Stars. I. Initial Results for Coalescence of Noncorotating Systems. ApJ, 431:742.

Dessart, L., Ott, C. D., Burrows, A., Rosswog, S., and Livne, E. (2009). Neutrino Signatures and the Neutrino-Driven Wind in Binary Neutron Star Mergers. ApJ, 690(2):1681–1705.

Dichiara, S., Troja, E., O'Connor, B., Marshall, F. E., Beniamini, P., Cannizzo, J. K., Lien, A. Y., and Sakamoto, T. (2020). Short gamma-ray bursts within 200 Mpc. MNRAS, 492(4):5011–5022.

Dobie, D., Kaplan, D. L., Murphy, T., Lenc, E., Mooley, K. P., Lynch, C., Corsi, A., Frail, D., Kasliwal, M., and Hallinan, G. (2018). A Turnover in the Radio Light Curve of GW170817. ApJ, 858(2):L15.

Dobie, D., Stewart, A., Murphy, T., Lenc, E., Wang, Z., Kaplan, D. L., and et al. (2019). An ASKAP Search for a Radio Counterpart to the First High-significance Neutron Star?Black Hole Merger LIGO/Virgo S190814bv. ApJ, 887(1):L13.

Evans, P. A., Cenko, S. B., Kennea, J. A., Emery, S. W. K., Kuin, N. P. M., Korobkin, O., and et al. (2017). Swift and NuSTAR observations of GW170817: Detection of a blue kilonova. Science, 358(6370):1565–1570.

Evans, P. A., Kennea, J. A., Tohuvavohu, A., Barthelmy, S. D., Beardmore, A. P., Bernardini, M. G., and Swift Team (2019). LIGO/Virgo S190814bv: No strong counterpart candidates in Swift/XRT observations. GRB Coordinates Network, 25400:1.

Fernández, R., Kasen, D., Metzger, B. D., and Quataert, E. (2015). Outflows from accretion discs formed in neutron star mergers: effect of black hole spin. MNRAS, 446(1):750–758.

Fong, W., Blanchard, P. K., Alexander, K. D., Strader, J., Margutti, R., Hajela, A., Villar, V. A., Wu, Y., Ye, C. S., Berger, E., Chornock, R., Coppejans, D., Cowperthwaite, P. S., Eftekhari, T., Giannios, D., Guidorzi, C., Kathirgamaraju, A., Laskar, T., Macfadyen, A., Metzger, B. D., Nicholl, M., Paterson, K., Terreran, G., Sand, D. J., Sironi, L., Williams, P. K. G., Xie, X., and Zrake, J. (2019). The Optical Afterglow of GW170817: An Off-axis Structured Jet and Deep Constraints on a Globular Cluster Origin. ApJ, 883(1):L1.

Fong, W., Metzger, B. D., Berger, E., and Özel, F. (2016). Radio Constraints on Long-lived Magnetar Remnants in Short Gamma-Ray Bursts. ApJ, 831(2):141.

Fraija, N. (2014). GeV-PeV neutrino production and oscillation in hidden jets from gamma-ray bursts. MNRAS, 437:2187–2200.

Fraija, N., De Colle, F., Veres, P., Dichiara, S., Barniol Duran, R., Galvan-Gamez, A., and Pedreira, A. C. C. d. E. S. (2019a). The Short GRB 170817A: Modeling the Off-axis Emission and Implications on the Ejecta Magnetization. ApJ, 871:123.

Fraija, N., De Colle, F., Veres, P., Dichiara, S., Barniol Duran, R., Pedreira, A. C. C. d. E. S., Galvan-Gamez, A., and Betancourt Kamenetskaia, B. (2019b). Description of atypical bursts seen slightly off-axis. arXiv e-prints, page arXiv:1906.00502.

Fraija, N., Dichiara, S., Pedreira, A. C. C. d. E. S., Galvan-Gamez, A., Becerra, R. L., Barniol Duran, R., and Zhang, B. B. (2019c). Analysis and Modeling of the Multi-wavelength Observations of the Luminous GRB 190114C. ApJ, 879(2):L26.

Fraija, N., Lopez-Camara, D., Pedreira, A. C. C. d. E. S., Betancourt Kamenetskaia, B., Veres, P., and Dichiara, S. (2019d). Signatures from a Quasi-spherical Outflow and an Off-axis Top-hat Jet Launched in a Merger of Compact Objects: An Analytical Approach. ApJ, 884(1):71.

Fraija, N., Pedreira, A. C. C. d. E. S., and Veres, P. (2019e). Light Curves of a Shock-breakout Material and a Relativistic Off-axis Jet from a Binary Neutron Star System. ApJ, 871:200.

Fraija, N., Veres, P., Zhang, B. B., Barniol Duran, R., Becerra, R. L., Zhang, B., Lee, W. H., Watson, A. M., Ordaz-Salazar, C., and Galvan-Gamez, A. (2017). Theoretical Description of GRB 160625B with Wind-to-ISM Transition and Implications for a Magnetized Outflow. ApJ, 848:15.

Franceschini, A. and Rodighiero, G. (2017). The extragalactic background light revisited and the cosmic photon- photon opacity. A&A, 603:A34.

Gal-Yam, A. (2017). Observational and Physical Classification of Supernovae, page 195.

Galama, T. J., Vreeswijk, P. M., van Paradijs, J., Kouveliotou, C., Augusteijn, T., Böhnhardt, H., and et al. (1998). An unusual supernova in the error box of the γ-ray burst of 25 April 1998. Nature, 395:670–672.

Gao, H., Ding, X., Wu, X.-F., Zhang, B., and Dai, Z.-G. (2013a). Bright Broadband Afterglows of Gravitational Wave Bursts from Mergers of Binary Neutron Stars. ApJ, 771(2):86.

Gao, H., Lei, W.-H., Wu, X.-F., and Zhang, B. (2013b). Compton scattering of self-absorbed synchrotron emission. MNRAS, 435:2520–2531.

Gao, H., Wang, X.-G., Mészáros, P., and Zhang, B. (2015). A Morphological Analysis of Gamma-Ray Burst Early-optical Afterglows. ApJ, 810:160.

Geng, J.-J., Zhang, B., Kölligan, A., Kuiper, R., and Huang, Y.-F. (2019). Propagation of a Short GRB Jet in the Ejecta: Jet Launching Delay Time, Jet Structure, and GW170817/GRB 170817A. ApJ, 877(2):L40.

Giblin, T. W., van Paradijs, J., Kouveliotou, C., Connaughton, V., Wijers, R. A. M. J., Briggs, M. S., Preece, R. D., and Fishman, G. J. (1999). Evidence for an Early High-Energy Afterglow Observed with BATSE from GRB 980923. ApJ, 524:L47–L50.

Goldstein, A., Veres, P., Burns, E., Briggs, M. S., Hamburg, R., Kocevski, D., and et al. (2017). An Ordinary Short Gamma-Ray Burst with Extraordinary Implications: Fermi-GBM Detection of GRB 170817A. ApJ, 848:L14.

Gomez, S., Hosseinzadeh, G., Cowperthwaite, P. S., Villar, V. A., Berger, E., Gardner, T., and et al. (2019). A Galaxy-targeted Search for the Optical Counterpart of the Candidate NS-BH Merger S190814bv with Magellan. ApJ, 884(2):L55.

Gompertz, B. P., Levan, A. J., Tanvir, N. R., Hjorth, J., Covino, S., Evans, P. A., Fruchter, A. S., González-Fernández, C., Jin, Z. P., Lyman, J. D., Oates, S. R., O'Brien, P. T., and Wiersema, K. (2018). The Diversity of Kilonova Emission in Short Gamma-Ray Bursts. ApJ, 860(1):62.

Goriely, S., Bauswein, A., and Janka, H.-T. (2011). r-process Nucleosynthesis in Dynamically Ejected Matter of Neutron Star Mergers. ApJ, 738(2):L32.

Gottlieb, O., Nakar, E., and Piran, T. (2018). The cocoon emission - an electromagnetic counterpart to gravitational waves from neutron star mergers. MNRAS, 473(1):576–584.

Grossman, D., Korobkin, O., Rosswog, S., and Piran, T. (2014). The long-term evolution of neutron star merger remnants - II. Radioactively powered transients. MNRAS, 439(1):757–770.

Haggard, D., Nynka, M., Ruan, J. J., Kalogera, V., Cenko, S. B., Evans, P., and Kennea, J. A. (2017). A Deep Chandra X-Ray Study of Neutron Star Coalescence GW170817. ApJ, 848(2):L25.

Hajela, A., Margutti, R., Alexander, K. D., Kathirgamaraju, A., Baldeschi, A., Guidorzi, C., Giannios, D., Fong, W., Wu, Y., MacFadyen, A., Paggi, A., Berger, E., Blanchard, P. K., Chornock, R., Coppejans, D. L., Cowperthwaite, P. S., Eftekhari, T., Gomez, S., Hosseinzadeh, G., Laskar, T., Metzger, B. D., Nicholl, M., Paterson, K., Radice, D., Sironi, L., Terreran, G., Villar, V. A., Williams, P. K. G., Xie, X., and Zrake, J. (2019). Two Years of Nonthermal Emission from the Binary Neutron Star Merger GW170817: Rapid Fading of the Jet Afterglow and First Constraints on the Kilonova Fastest Ejecta. ApJ, 886(1):L17.

12

Horesh, A., Kulkarni, S. R., Corsi, A., Frail, D. A., Cenko, S. B., Ben-Ami, S., Gal-Yam, A., Yaron, O., Arcavi, I., Kasliwal, M. M., and Ofek, E. O. (2013). PTF 12gzk—A Rapidly Declining, High-velocity Type Ic Radio Supernova. ApJ, 778(1):63.

Hotokezaka, K., Kiuchi, K., Shibata, M., Nakar, E., and Piran, T. (2018). Synchrotron Radiation from the Fast Tail of Dynamical Ejecta of Neutron Star Mergers. ApJ, 867(2):95.

Hotokezaka, K., Kyutoku, K., Tanaka, M., Kiuchi, K., Sekiguchi, Y., Shibata, M., and Wanajo, S. (2013). Progenitor Models of the Electromagnetic Transient Associated with the Short Gamma Ray Burst 130603B. ApJ, 778:L16.

Hotokezaka, K. and Piran, T. (2015). Mass ejection from neutron star mergers: different components and expected radio signals. MNRAS, 450:1430–1440.

Huang, Y. F. and Cheng, K. S. (2003). Gamma-ray bursts: optical afterglows in the deep Newtonian phase. MNRAS, 341:263–269.

Huang, Y. F., Dai, Z. G., and Lu, T. (1998). GRB afterglows: from ultra-relativistic to non-relativistic phase. A&A, 336:L69–L72.

Huang, Y. F., Dai, Z. G., and Lu, T. (1999). A generic dynamical model of gamma-ray burst remnants. MNRAS, 309:513–516.

Izzo, L., Auchettl, K., Hjorth, J., De Colle, F., Gall, C., Angus, C. R., Raimundo, S. I., and Ramirez-Ruiz, E. (2020). The broad-line type Ic SN 2020bvc: signatures of an off-axis gamma-ray burst afterglow. arXiv e-prints, page arXiv:2004.05941.

Izzo, L., de Ugarte Postigo, A., Maeda, K., Thöne, C. C., Kann, D. A., Della Valle, M., Sagues Carracedo, A., Michałowski, M. J., Schady, P., Schmidl, S., Selsing, J., Starling, R. L. C., Suzuki, A., Bensch, K., Bolmer, J., Campana, S., Cano, Z., Covino, S., Fynbo, J. P. U., Hartmann, D. H., Heintz, K. E., Hjorth, J., Japelj, J., Kamiński, K., Kaper, L., Kouveliotou, C., KruŻyński, M., Kwiatkowski, T., Leloudas, G., Levan, A. J., Malesani, D. B., Michałowski, T., Piranomonte, S., Pugliese, G., Rossi, A., Sánchez-Ramírez, R., Schulze, S., Steeghs, D., Tanvir, N. R., Ulaczyk, K., Vergani, S. D., and Wiersema, K. (2019). Signatures of a jet cocoon in early spectra of a supernova associated with a γ-ray burst. Nature, 565(7739):324–327.

Jin, Z.-P., Hotokezaka, K., Li, X., Tanaka, M., D'Avanzo, P., Fan, Y.-Z., Covino, S., Wei, D.-M., and Piran, T. (2016). The Macronova in GRB 050709 and the GRB-macronova connection. Nature Communications, 7:12898.

Jin, Z. P., Xu, D., Covino, S., D'Avanzo, P., Antonelli, A., Fan, Y. Z., and Wei, D. M. (2009). The X-ray afterglow of GRB 081109A: clue to the wind bubble structure. MNRAS, 400:1829–1834.

Kamble, A., Resmi, L., and Misra, K. (2007). Observations of the Optical Afterglow of GRB 050319: The Wind-to-ISM Transition in View. ApJ, 664:L5–L8.

Kasen, D., Badnell, N. R., and Barnes, J. (2013). Opacities and Spectra of the r-process Ejecta from Neutron Star Mergers. ApJ, 774:25.

Kasliwal, M. M., Korobkin, O., Lau, R. M., Wollaeger, R., and Fryer, C. L. (2017a). Infrared Emission from Kilonovae: The Case of the Nearby Short Hard Burst GRB 160821B. ApJ, 843(2):L34.

Kasliwal, M. M., Nakar, E., Singer, L. P., Kaplan, D. L., Cook, D. O., Van Sistine, A., and et al. (2017b). Illuminating gravitational waves: A concordant picture of photons from a neutron star merger. Science, 358:1559–1565.

Kathirgamaraju, A., Barniol Duran, R., and Giannios, D. (2016). GRB off-axis afterglows and the emission from the accompanying supernovae. MNRAS, 461(2):1568–1575.

Kathirgamaraju, A., Barniol Duran, R., and Giannios, D. (2018). Off-axis short GRBs from structured jets as counterparts to GW events. MNRAS, 473(1):L121–L125.

Kathirgamaraju, A., Giannios, D., and Beniamini, P. (2019). Observable features of GW170817 kilonova afterglow. MNRAS, 487(3):3914–3921.

Kotak, R., Meikle, W. P. S., Adamson, A., and Leggett, S. K. (2004). On the nature of the circumstellar medium of the remarkable Type Ia/IIn supernova SN 2002ic. MNRAS, 354:L13–L17.

Kouveliotou, C., Meegan, C. A., Fishman, G. J., Bhat, N. P., Briggs, M. S., Koshut, T. M., Paciesas, W. S., and Pendleton, G. N. (1993). Identification of Two Classes of Gamma-Ray Bursts. ApJ, 413:L101.

Kulkarni, S. R., Frail, D. A., Wieringa, M. H., Ekers, R. D., Sadler, E. M., Wark, R. M., Higdon, J. L., Phinney, E. S., and Bloom, J. S. (1998). Radio emission from the unusual supernova 1998bw and its association with the γ-ray burst of 25 April 1998. Nature, 395(6703):663–669.

Kyutoku, K., Ioka, K., and Shibata, M. (2014). Ultrarelativistic electromagnetic counterpart to binary neutron star mergers. MNRAS, 437:L6–L10.

Lamb, G. P. and Kobayashi, S. (2017). Electromagnetic counterparts to structured jets from gravitational wave detected mergers. MNRAS, 472:4953–4964.

Lazzati, D., López-Cámara, D., Cantiello, M., Morsony, B. J., Perna, R., and Workman, J. C. (2017). Off-axis Prompt X-Ray Transients from the Cocoon of Short Gamma-Ray Bursts. ApJ, 848:L6.

Lazzati, D., Morsony, B. J., Blackwell, C. H., and Begelman, M. C. (2012). Unifying the Zoo of Jet-driven Stellar Explosions. ApJ, 750(1):68.

Lazzati, D., Perna, R., Morsony, B. J., Lopez-Camara, D., Cantiello, M., Ciolfi, R., Giacomazzo, B., and Workman, J. C. (2018). Late Time Afterglow Observations Reveal a Collimated Relativistic Jet in the Ejecta of the Binary Neutron Star Merger GW170817. Phys. Rev. Lett., 120(24):241103.

Li, L.-X. and Paczyński, B. (1998). Transient Events from Neutron Star Mergers. ApJ, 507:L59–L62.

Liang, E.-W., Li, L., Gao, H., Zhang, B., Liang, Y.-F., Wu, X.-F., Yi, S.-X., Dai, Z.-G., Tang, Q.-W., Chen, J.-M., Lü, H.-J., Zhang, J., Lu, R.-J., Lü, L.-Z., and Wei, J.-Y. (2013). A Comprehensive Study of Gamma-Ray Burst Optical Emission. II. Afterglow Onset and Late Re-brightening Components. ApJ, 774(1):13.

LIGO Scientific Collaboration and Virgo Collaboration (2019a). LIGO/Virgo S190814bv: Identification of a GW compact binary merger candidate. GRB Coordinates Network, 25324:1.

LIGO Scientific Collaboration and Virgo Collaboration (2019b). LIGO/Virgo S190814bv: Update on Sky-Localization and Source-Classification. GRB Coordinates Network, 25333:1.

Liu, L.-D., Gao, H., and Zhang, B. (2020). Constraining the Long-lived Magnetar Remnants in Short Gamma-Ray Bursts from Late-time Radio Observations. ApJ, 890(2):102.

Livio, M. and Waxman, E. (2000). Toward a Model for the Progenitors of Gamma-Ray Bursts. ApJ, 538:187–191.

Lyman, J. D., Lamb, G. P., Levan, A. J., Mandel, I., Tanvir, N. R., Kobayashi, S., and et al. (2018). The optical afterglow of the short gamma-ray burst associated with GW170817. Nature Astronomy, 2:751–754.

MacFadyen, A. I., Woosley, S. E., and Heger, A. (2001). Supernovae, Jets, and Collapsars. ApJ, 550(1):410–425.

Mandel, I. (2018). The Orbit of GW170817 Was Inclined by Less Than 28° to the Line of Sight. ApJ, 853(1):L12.

Margalit, B. and Piran, T. (2020). Shock within a shock: revisiting the radio flares of NS merger ejecta and GRB-supernovae. arXiv e-prints, page arXiv:2004.13028.

Margutti, R., Alexander, K. D., Xie, X., Sironi, L., Metzger, B. D., Kathirgamaraju, A., Fong, W., Blanchard, P. K., Berger, E., MacFadyen, A., Giannios, D., Guidorzi, C., Hajela, A., Chornock, R., Cowperthwaite, P. S., Eftekhari, T., Nicholl, M., Villar, V. A., Williams, P. K. G., and Zrake, J. (2018). The Binary Neutron Star Event LIGO/Virgo GW170817 160 Days after Merger: Synchrotron Emission across the Electromagnetic Spectrum. ApJ, 856(1):L18.

Margutti, R., Kamble, A., Milisavljevic, D., Zapartas, E., de Mink, S. E., Drout, M., Chornock, R., Risaliti, G., Zauderer, B. A., Bietenholz, M., Cantiello, M., Chakraborti, S., Chomiuk, L., Fong, W., Grefenstette, B., Guidorzi, C., Kirshner, R., Parrent, J. T., Patnaude, D., Soderberg, A. M., Gehrels, N. C., and Harrison, F. (2017). Ejection of the Massive Hydrogen-rich Envelope Timed with the Collapse of the Stripped SN 2014C. ApJ, 835(2):140.

Margutti, R., Milisavljevic, D., Soderberg, A. M., Guidorzi, C., Morsony, B. J., Sanders, N., Chakraborti, S., Ray, A., Kamble, A., Drout, M., Parrent, J., Zauderer, A., and Chomiuk, L. (2014). Relativistic Supernovae have Shorter-lived Central Engines or More Extended Progenitors: The Case of SN 2012ap. ApJ, 797(2):107.

Margutti, R., Soderberg, A. M., Chomiuk, L., Chevalier, R., Hurley, K., and et al. (2012). Inverse Compton X-Ray Emission from Supernovae with Compact Progenitors: Application to SN2011fe. ApJ, 751(2):134.

Margutti, R., Soderberg, A. M., Wieringa, M. H., Edwards, P. G., Chevalier, R. A., and et al. (2013). The Signature of the Central Engine in the Weakest Relativistic Explosions: GRB 100316D. ApJ, 778(1):18.

Mészáros, P. and Waxman, E. (2001). TeV Neutrinos from Successful and Choked Gamma-Ray Bursts. Phys. Rev. Lett., 87(17):171102.

Metzger, B. D. (2017). Kilonovae. Living Reviews in Relativity, 20:3.

Metzger, B. D. (2019). Kilonovae. Living Reviews in Relativity, 23(1):1.

Metzger, B. D., Bauswein, A., Goriely, S., and Kasen, D. (2015). Neutron-powered precursors of kilonovae. MNRAS, 446:1115–1120.

Metzger, B. D. and Berger, E. (2012). What is the Most Promising Electromagnetic Counterpart of a Neutron Star Binary Merger? ApJ, 746(1):48.

Metzger, B. D. and Bower, G. C. (2014). Constraints on long-lived remnants of neutron star binary mergers from late-time radio observations of short duration gamma-ray bursts. MNRAS, 437(2):1821–1827.

Metzger, B. D. and Fernández, R. (2014). Red or blue? A potential kilonova imprint of the delay until black hole formation following a neutron star merger. MNRAS, 441(4):3444–3453.

Metzger, B. D., Martínez-Pinedo, G., Darbha, S., Quataert, E., Arcones, A., Kasen, D., Thomas, R., Nugent, P., Panov, I. V., and Zinner, N. T. (2010). Electromagnetic counterparts of compact object mergers powered by the radioactive decay of r-process nuclei. MNRAS, 406:2650–2662.

Metzger, B. D., Quataert, E., and Thompson, T. A. (2008). Short-duration gamma-ray bursts with extended emission from protomagnetar spin-down. MNRAS, 385(3):1455–1460.

Miller, J. M., Ryan, B. R., Dolence, J. C., Burrows, A., Fontes, C. J., Fryer, C. L., Korobkin, O., Lippuner, J., Mumpower, M. R., and Wollaeger, R. T. (2019). Full transport model of GW170817-like disk produces a blue kilonova. Phys. Rev. D, 100(2):023008.

Modjaz, M., Bianco, F. B., Siwek, M., Huang, S., Perley, D. A., Fierroz, D., Liu, Y.-Q., Arcavi, I., Gal-Yam, A., Filippenko, A. V., Blagorodnova, N., Cenko, B. S., Kasliwal, M., Kulkarni, S., Schulze, S., Taggart, K., and Zheng, W. (2020). Host Galaxies of Type Ic and Broad-lined Type Ic Supernovae from the Palomar Transient Factory: Implications for Jet Production. ApJ, 892(2):153.

Mooley, K. P., Deller, A. T., Gottlieb, O., Nakar, E., Hallinan, G., Bourke, S., Frail, D. A., Horesh, A., Corsi, A., and Hotokezaka, K. (2018a). Superluminal motion of a relativistic jet in the neutron-star merger GW170817. Nature, 561:355–359.

Mooley, K. P., Nakar, E., Hotokezaka, K., Hallinan, G., Corsi, A., Frail, D. A., and et al. (2018b). A mildly relativistic wide-angle outflow in the neutron-star merger event GW170817. Nature, 554(7691):207–210.

Moriya, T. J. and Tominaga, N. (2012). Diversity of luminous supernovae from non-steady mass loss. ApJ, 747:118–124.

Murguia-Berthier, A., Montes, G., Ramirez-Ruiz, E., De Colle, F., and Lee, W. H. (2014). Necessary Conditions for Short Gamma-Ray Burst Production in Binary Neutron Star Mergers. ApJ, 788:L8.

Nagakura, H., Hotokezaka, K., Sekiguchi, Y., Shibata, M., and Ioka, K. (2014). Jet Collimation in the Ejecta of Double Neutron Star Mergers: A New Canonical Picture of Short Gamma-Ray Bursts. ApJ, 784:L28.

Nakar, E. and Piran, T. (2017). The Observable Signatures of GRB Cocoons. ApJ, 834(1):28.

Nicholl, M., Berger, E., Kasen, D., Metzger, B. D., Elias, J., Briceño, C., and et al. (2017). The Electromagnetic Counterpart of the Binary Neutron Star Merger LIGO/Virgo GW170817. III. Optical and UV Spectra of a Blue Kilonova from Fast Polar Ejecta. ApJ, 848(2):L18.

Nicholl, M., Blanchard, P. K., Berger, E., Chornock, R., Margutti, R., Gomez, S., and et al. (2020). An extremely energetic supernova from a very massive star in a dense medium. Nature Astronomy.

Norris, J. P. and Bonnell, J. T. (2006). Short Gamma-Ray Bursts with Extended Emission. ApJ, 643:266–275.

Panaitescu, A. and Kumar, P. (2000). Analytic Light Curves of Gamma-Ray Burst Afterglows: Homogeneous versus Wind External Media. ApJ, 543:66–76.

Perego, A., Rosswog, S., Cabezón, R. M., Korobkin, O., Käppeli, R., Arcones, A., and Liebendörfer, M. (2014). Neutrino-driven winds from neutron star merger remnants. MNRAS, 443(4):3134–3156.

Piran, T., Nakar, E., and Rosswog, S. (2013). The electromagnetic signals of compact binary mergers. MNRAS, 430:2121–2136.

Planck Collaboration, Ade, P. A. R., Aghanim, N., Arnaud, M., Ashdown, M., Aumont, J., and et al. (2016). Planck 2015 results. XIII. Cosmological parameters. A&A, 594:A13.

Popham, R., Woosley, S. E., and Fryer, C. (1999). Hyperaccreting Black Holes and Gamma-Ray Bursts. ApJ, 518(1):356–374.

Ramirez-Ruiz, E., García-Segura, G., Salmonson, J. D., and Pérez-Rendón, B. (2005). The State of the Circumstellar Medium Surrounding Gamma-Ray Burst Sources and Its Effect on the Afterglow Appearance. ApJ, 631(1):435–445.

Rosswog, S. (2005). Mergers of Neutron Star-Black Hole Binaries with Small Mass Ratios: Nucleosynthesis, Gamma-Ray Bursts, and Electromagnetic Transients. ApJ, 634:1202–1213.

Rosswog, S., Korobkin, O., Arcones, A., Thielemann, F. K., and Piran, T. (2014). The long-term evolution of neutron star merger remnants - I. The impact of r-process nucleosynthesis. MNRAS, 439(1):744–756.

Rosswog, S., Liebendörfer, M., Thielemann, F. K., Davies, M. B., Benz, W., and Piran, T. (1999). Mass ejection in neutron star mergers. A&A, 341:499–526.

Ruffert, M., Janka, H. T., Takahashi, K., and Schaefer, G. (1997). Coalescing neutron stars - a step towards physical models. II. Neutrino emission, neutron tori, and gamma-ray bursts. A&A, 319:122–153.

Sari, R. and Esin, A. A. (2001). On the Synchrotron Self-Compton Emission from Relativistic Shocks and Its Implications for Gamma-Ray Burst Afterglows. ApJ, 548:787–799.

Sari, R. and Mészáros, P. (2000). Impulsive and Varying Injection in Gamma-Ray Burst Afterglows. ApJ, 535(1):L33–L37.

Savchenko, V., Ferrigno, C., Kuulkers, E., Bazzano, A., Bozzo, E., Brandt, S., and et al. (2017). INTEGRAL Detection of the First Prompt Gamma-Ray Signal Coincident with the Gravitational-wave Event GW170817. ApJ, 848:L15.

Schroeder, G., Margalit, B., Fong, W.-f., Metzger, B. D., Williams, P. K. G., Paterson, K., Alexander, K. D., Laskar, T., Goyal, A. V., and Berger, E. (2020). A Late-time Radio Survey of Short GRBs at $z < 0.5$: New Constraints on the Remnants of Neutron Star Mergers. arXiv e-prints, page arXiv:2006.07434.

Shibata, M. and Taniguchi, K. (2006). Merger of binary neutron stars to a black hole: Disk mass, short gamma-ray bursts, and quasinormal mode ringing. Phys. Rev. D, 73(6):064027.

Siegel, D. M. and Metzger, B. D. (2017). Three-Dimensional General-Relativistic Magnetohydrodynamic Simulations of Remnant Accretion Disks from Neutron Star Mergers: Outflows and r -Process Nucleosynthesis. Phys. Rev. Lett., 119(23):231102.

Sironi, L. and Giannios, D. (2013). A Late-time Flattening of Light Curves in Gamma-Ray Burst Afterglows. ApJ, 778(2):107.

Smartt, S. J., Chen, T. W., Jerkstrand, A., Coughlin, M., Kankare, E., Sim, S. A., and et al. (2017). A kilonova as the electromagnetic counterpart to a gravitational-wave source. Nature, 551(7678):75–79.

Soares-Santos, M., Holz, D. E., Annis, J., Chornock, R., Herner, K., Berger, E., and Dark Energy Camera GW-EM Collaboration (2017). The Electromagnetic Counterpart of the Binary Neutron Star Merger LIGO/Virgo GW170817. I. Discovery of the Optical Counterpart Using the Dark Energy Camera. ApJ, 848(2):L16.

Sobacchi, E., Granot, J., Bromberg, O., and Sormani, M. C. (2017). A common central engine for long gamma-ray bursts and Type Ib/c supernovae. MNRAS, 472(1):616–627.

Soderberg, A. M., Chevalier, R. A., Kulkarni, S. R., and Frail, D. A. (2006). The radio and X-ray luminous SN 2003bg and the circumstellar density variation around radio supernovae. ApJ, 651:1005–1018.

Surman, R., McLaughlin, G. C., Ruffert, M., Janka, H. T., and Hix, W. R. (2008). r-Process Nucleosynthesis in Hot Accretion Disk Flows from Black Hole-Neutron Star Mergers. ApJ, 679(2):L117.

Tan, J. C., Matzner, C. D., and McKee, C. F. (2001). Trans-Relativistic Blast Waves in Supernovae as Gamma-Ray Burst Progenitors. ApJ, 551:946–972.

Tanvir, N. R., Levan, A. J., Fruchter, A. S., Hjorth, J., Hounsell, R. A., Wiersema, K., and Tunnicliffe, R. L. (2013). A 'kilonova' associated with the short-duration γ-ray burst GRB 130603B. Nature, 500:547–549.

Tanvir, N. R., Levan, A. J., González-Fernández, C., Korobkin, O., Mandel, I., Rosswog, S., and et al. (2017). The Emergence of a Lanthanide-rich Kilonova Following the Merger of Two Neutron Stars. ApJ, 848(2):L27.

Totani, T. (2003). A Failed Gamma-Ray Burst with Dirty Energetic Jets Spirited Away? New Implications for the Gamma-Ray Burst-Supernova Connection from SN 2002ap. ApJ, 598(2):1151–1162.

Troja, E., Castro-Tirado, A. J., Becerra González, J., Hu, Y., Ryan, G. S., Cenko, S. B., and et al. (2019). The afterglow and kilonova of the short GRB 160821B. MNRAS, 489(2):2104–2116.

Troja, E., Lipunov, V. M., Mundell, C. G., and et al. (2017a). Significant and variable linear polarization during the prompt optical flash of GRB 160625B. Nature, 547:425–427.

Troja, E., Piro, L., Ryan, G., van Eerten, H., and Zhang, B. (2020a). GW170817: Continued X-ray emission detected with Chandra at 940 days post-merger. GRB Coordinates Network, 27411:1.

Troja, E., Piro, L., van Eerten, H., Wollaeger, R. T., Im, M., Fox, O. D., and et al. (2017b). The X-ray counterpart to the gravitational-wave event GW170817. Nature, 551(7678):71–74.

Troja, E., van Eerten, H., Zhang, B., Ryan, G., Piro, L., Ricci, R., O'Connor, B., Wieringa, M. H., Cenko, S. B., and Sakamoto, T. (2020b). A thousand days after the merger: continued X-ray emission from GW170817. arXiv e-prints, page arXiv:2006.01150.

14

Valenti, S., Benetti, S., Cappellaro, E., Patat, F., Mazzali, P., Turatto, M., Hurley, K., Maeda, K., Gal-Yam, A., Foley, R. J., Filippenko, A. V., Pastorello, A., Challis, P., Frontera, F., Harutyunyan, A., Iye, M., Kawabata, K., Kirshner, R. P., Li, W., Lipkin, Y. M., Matheson, T., Nomoto, K., Ofek, E. O., Ohyama, Y., Pian, E., Poznanski, D., Salvo, M., Sauer, D. N., Schmidt, B. P., Soderberg, A., and Zampieri, L. (2008). The broad-lined Type Ic supernova 2003jd. MNRAS, 383(4):1485–1500.

van Marle, A. J., Langer, N., Achterberg, A., and García-Segura, G. (2006). Forming a constant density medium close to long gamma-ray bursts. A&A, 460(1):105–116.

Vieira, N., Ruan, J. J., Haggard, D., Drout, M. R., Nynka, M. C., Boyce, H., Spekkens, K., Safi-Harb, S., Carlberg, R. G., Fernández, R., Piro, A. L., Afsariardchi, N., and Moon, D.-S. (2020). A Deep CFHT Optical Search for a Counterpart to the Possible Neutron Star – Black Hole Merger GW190814. arXiv e-prints, page arXiv:2003.09437.

Wanajo, S., Sekiguchi, Y., Nishimura, N., Kiuchi, K., Kyutoku, K., and Shibata, M. (2014). Production of All the r-process Nuclides in the Dynamical Ejecta of Neutron Star Mergers. ApJ, 789(2):L39.

Watson, A. M., Butler, N. R., Lee, W. H., Becerra, R. L., Pereyra, M., Angeles, F., Farah, A., Figueroa, L., Gónzalez-Buitrago, D., Quirós, F., Ruíz-Díaz-Soto, J., Tejada de Vargas, C., Tinoco, S. J., and Wolfram, T. (2020). Limits on the electromagnetic counterpart to S190814bv. MNRAS, 492(4):5916–5921.

Weinberg, S. (1972). Gravitation and Cosmology.

Wijers, R. A. M. J., Rees, M. J., and Meszaros, P. (1997). Shocked by GRB 970228: the afterglow of a cosmological fireball. MNRAS, 288:L51–L56.

Woosley, S. and Janka, T. (2005). The physics of core-collapse supernovae. Nature Physics, 1(3):147–154.

Woosley, S. E. (1993). Gamma-Ray Bursts from Stellar Mass Accretion Disks around Black Holes. ApJ, 405:273.

Woosley, S. E. and Bloom, J. S. (2006). The Supernova Gamma-Ray Burst Connection. ARA&A, 44:507–556.

Yamazaki, R., Toma, K., Ioka, K., and Nakamura, T. (2006). Tail emission of prompt gamma-ray burst jets. MNRAS, 369:311–316.

Yang, B., Jin, Z.-P., Li, X., Covino, S., Zheng, X.-Z., Hotokezaka, and et al. (2015). A possible macronova in the late afterglow of the long-short burst GRB 060614. Nature Communications, 6:7323.

Yi, S.-X., Wu, X.-F., and Dai, Z.-G. (2013). Early Afterglows of Gamma-Ray Bursts in a Stratified Medium with a Power-law Density Distribution. ApJ, 776(2):120.

Zhang, B. and Mészáros, P. (2001). High-Energy Spectral Components in Gamma-Ray Burst Afterglows. ApJ, 559:110–122.

TABLE 1
THE RELEVANT TERMS OF THE FREE-COASTING AND DECELERATION PHASES.

	k = 0	k = 1.0	k = 1.5	k = 2.0	k = 2.5
A_k	$1\,\mathrm{cm}^{-3}$	$1.5 \times 10^{19}\,\mathrm{cm}^{-2}$	$2.7 \times 10^{28}\,\mathrm{cm}^{-\frac{3}{2}}$	$3 \times 10^{36}\,\mathrm{cm}^{-1}$	$1.3 \times 10^{45}\,\mathrm{cm}^{-\frac{1}{2}}$
Coasting Phase					
$r^0\,(\times 10^{17}\,\mathrm{cm})$	2.2	1.8	1.5	1.3	1.1
γ_m^0	12.4	12.4	12.4	12.4	12.4
$\gamma_\mathrm{c}^0\,(\times 10^3)$	3.1×10^2	1.8	0.3	0.8	0.5
$\nu_{\mathrm{a},1}^{\mathrm{syn},0}\,(\mathrm{Hz})$	2.9×10^9	1.3×10^{11}	5.5×10^{11}	2.9×10^{11}	6.4×10^{11}
$\nu_{\mathrm{a},2}^{\mathrm{syn},0}\,(\mathrm{Hz})$	1.0×10^8	2.5×10^9	8.1×10^9	4.7×10^9	7.7×10^9
$\nu_{\mathrm{a},3}^{\mathrm{syn},0}\,(\mathrm{Hz})$	1.5×10^6	6.5×10^9	9.3×10^{10}	2.6×10^{10}	7.5×10^{10}
$\nu_\mathrm{m}^{\mathrm{syn},0}\,(\mathrm{Hz})$	3.5×10^6	4.6×10^7	1.1×10^8	6.8×10^7	8.3×10^7
$\nu_\mathrm{c}^{\mathrm{syn},0}\,(\mathrm{Hz})$	2.9×10^{16}	7.3×10^{12}	2.8×10^{11}	1.7×10^{12}	8.2×10^{11}
$F_{\nu,\mathrm{max}}^{\mathrm{syn},0}\,(\mathrm{mJy})$	1.1×10^2	6.5×10^4	5.5×10^5	8.1×10^4	1.1×10^5
$\nu_{\mathrm{mm}}^{\mathrm{ssc},0}\,(\mathrm{eV})$	7.0×10^{-7}	9.2×10^{-6}	2.3×10^{-5}	1.4×10^{-5}	1.7×10^{-5}
$\nu_{\mathrm{cc}}^{\mathrm{ssc},0}\,(\mathrm{MeV})$	3.8×10^6	3.2×10^{-2}	3.4×10^{-5}	1.5×10^{-3}	3.2×10^{-4}
$\nu_{\mathrm{ma},1}^{\mathrm{ssc},0}\,(\mathrm{eV})$	5.8×10^{-4}	2.6×10^{-2}	0.1	6.0×10^{-2}	0.1
$\nu_{\mathrm{mc},1}^{\mathrm{ssc},0}\,(\mathrm{eV})$	5.9×10^3	1.5	5.7×10^{-2}	0.3	0.2
$\nu_{\mathrm{ma},2}^{\mathrm{ssc},0}\,(\mathrm{eV})$	2.1×10^{-5}	5.1×10^{-4}	1.6×10^{-3}	9.5×10^{-4}	1.6×10^{-3}
$\nu_{\mathrm{mc},2}^{\mathrm{ssc},0}\,(\mathrm{eV})$	5.9×10^3	1.5	5.7×10^{-2}	0.3	0.2
$\nu_{\mathrm{ca},2}^{\mathrm{ssc},0}\,(\mathrm{eV})$	1.3×10^4	11.1	1.0	4.1	3.0
$\nu_{\mathrm{ca},3}^{\mathrm{ssc},0}\,(\mathrm{eV})$	1.9×10^2	28.4	11.4	22.9	29.3
$\nu_{\mathrm{cm},3}^{\mathrm{ssc},0}\,(\mathrm{eV})$	4.5×10^2	0.2	1.4×10^{-2}	5.9×10^{-2}	3.2×10^{-2}
$F_{\nu,\mathrm{max}}^{\mathrm{ssc},0}\,(\mathrm{mJy})$	5.8×10^{-5}	2.3	89.0	4.4	9.6
Deceleration					
$t^0\,(\times 10^3\,\mathrm{day})$	1.2	1.1	1.4	28.4	7.0×10^3
$r^0\,(\times 10^{17}\,\mathrm{cm})$	7.2	4.1	3.2	3.2	2.6
$\gamma_\mathrm{m}^0\,(\times 10^1)$	13.2	6.8	5.2	7.3	6.7
$\gamma_\mathrm{c}^0\,(\times 10^4)$	3.0	0.2	0.05	0.2	0.1
$\nu_{\mathrm{a},1}^{\mathrm{syn},0}\,(\mathrm{Hz})$	8.8×10^8	2.5×10^{10}	9.5×10^{10}	2.5×10^{10}	4.6×10^{10}
$\nu_{\mathrm{a},2}^{\mathrm{syn},0}\,(\mathrm{Hz})$	1.1×10^9	6.1×10^9	1.2×10^{10}	6.4×10^9	8.4×10^9
$\nu_{\mathrm{a},3}^{\mathrm{syn},0}\,(\mathrm{Hz})$	3.2×10^7	4.3×10^9	2.9×10^{10}	4.2×10^9	8.5×10^9
$\nu_\mathrm{m}^{\mathrm{syn},0}\,(\mathrm{Hz})$	1.3×10^9	1.5×10^9	1.5×10^9	1.6×10^9	1.5×10^9
$\nu_\mathrm{c}^{\mathrm{syn},0}\,(\mathrm{Hz})$	5.2×10^{14}	3.2×10^{12}	4.0×10^{11}	4.2×10^{12}	2.8×10^{12}
$F_{\nu,\mathrm{max}}^{\mathrm{syn},0}\,(\mathrm{mJy})$	1.3×10^4	3.8×10^5	1.3×10^6	1.3×10^5	1.0×10^5
$\nu_{\mathrm{mm}}^{\mathrm{ssc},0}\,(\mathrm{eV})$	2.9×10^{-2}	8.8×10^{-3}	5.5×10^{-3}	1.1×10^{-2}	8.7×10^{-3}
$\nu_{\mathrm{cc}}^{\mathrm{ssc},0}\,(\mathrm{MeV})$	6.0×10^2	1.0×10^{-2}	1.3×10^{-4}	1.8×10^{-2}	7.7×10^{-3}
$\nu_{\mathrm{ma},1}^{\mathrm{ssc},0}\,(\mathrm{MeV})$	2.0×10^{-2}	0.1	0.3	0.2	0.3
$\nu_{\mathrm{mc},1}^{\mathrm{ssc},0}\,(\mathrm{MeV})$	1.2×10^4	19.3	1.4	29.6	16.3
$\nu_{\mathrm{ma},2}^{\mathrm{ssc},0}\,(\mathrm{MeV})$	2.4×10^{-2}	3.7×10^{-2}	4.4×10^{-2}	4.5×10^{-2}	4.9×10^{-2}
$\nu_{\mathrm{mc},2}^{\mathrm{ssc},0}\,(\mathrm{MeV})$	1.2×10^4	19.3	1.4	29.6	16.3
$\nu_{\mathrm{ca},2}^{\mathrm{ssc},0}\,(\mathrm{MeV})$	1.2×10^3	19.6	4.0	28.2	23.2
$\nu_{\mathrm{ca},3}^{\mathrm{ssc},0}\,(\mathrm{MeV})$	36.7	14.0	9.2	18.5	23.4
$\nu_{\mathrm{cm},3}^{\mathrm{ssc},0}\,(\mathrm{MeV})$	1.6×10^3	10.2	0.9	7.0	2.2
$F_{\nu,\mathrm{max}}^{\mathrm{ssc},0}\,(\mathrm{mJy})$	2.1×10^{-2}	13.7	1.4×10^2	2.9	2.5

TABLE 2
THE LATEST DATA POINTS FROM CHANDRA AFTERGLOW OBSERVATIONS OF GRB 170817A.

δt	$F_{\rm X}$ (0.3 - 10 keV)	F_ν (1 keV)	$\Gamma_{\rm X}$
(days)	$(\times 10^{15} \, {\rm erg \, cm^{-2} \, s^{-1}})$	$(\times 10^{-7} {\rm mJy})$	
358.6	$7.75^{+2.70}_{-0.73}$	$6.77^{+2.36}_{-0.64}$	$1.69^{+0.49}_{-0.34}$
582.2	$3.25^{+0.85}_{-1.03}$	$2.76^{+0.72}_{-0.88}$	1.57
741.9	$2.21^{+0.85}_{-0.79}$	$1.88^{+0.72}_{-0.67}$	1.57
940	$1.10^{+0.60}_{-0.60}$	$0.95^{+0.52}_{-0.52}$	1.585

The data points in $\rm erg \, cm^{-2} \, s^{-1}$ are taken from Hajela et al. (2019) and Troja et al. (2020a).

APPENDIX

LIGHT CURVES OF SSC EMISSION

The free-coasting phase

The corresponding SSC break frequencies during the free-coasting phase are given by

$$
h\nu_{\rm mm}^{\rm ssc} = \nu_{\rm mm}^{\rm ssc,0}\, g^4(p) \left(\frac{1+z}{1.022}\right)^{\frac{k-2}{2}} \epsilon_{\rm e,-1}^4\, \epsilon_{\rm B,-2}^{\frac{1}{2}} A_{\rm k}^{\frac{1}{2}} \beta_{-0.5}^{\frac{18-k}{2}} t_6^{-\frac{k}{2}}
$$
$$
h\nu_{\rm cc}^{\rm ssc} = \nu_{\rm cc}^{\rm ssc,0} \left(\frac{1+z}{1.022}\right)^{\frac{6-7k}{2}} (1+Y)^{-4}\, \epsilon_{\rm B,-2}^{-\frac{7}{2}} A_{\rm k}^{-\frac{7}{2}} \beta_{-0.5}^{\frac{7(k-2)}{2}} t_6^{\frac{7k-8}{2}} . \tag{A1}
$$

For the case $\nu_{\rm a,1}^{\rm syn} \le \nu_{\rm m}^{\rm syn} \le \nu_{\rm c}^{\rm syn}$, the SSC break frequencies are

$$
h\nu_{\rm ma,1}^{\rm ssc} = \nu_{\rm ma,1}^{\rm ssc,0}\, g(p) \left(\frac{1+z}{1.022}\right)^{\frac{4(k-2)}{5}} \epsilon_{\rm e,-1}\, \epsilon_{\rm B,-2}^{\frac{1}{5}} A_{\rm k}^{\frac{4}{5}} \beta_{-0.5}^{-\frac{4k-15}{5}} t_6^{\frac{3-4k}{5}}
$$
$$
h\nu_{\rm mc,1}^{\rm ssc} = \nu_{\rm mc,1}^{\rm ssc,0}\, g^2(p) \left(\frac{1+z}{1.022}\right)^{\frac{2-3k}{2}} (1+Y)^{-2}\, \epsilon_{\rm e,-1}^2\, \epsilon_{\rm B,-2}^{-\frac{3}{2}} A_{\rm k}^{-\frac{3}{2}} \beta_{-0.5}^{\frac{3k+2}{2}} t_6^{\frac{3k-4}{2}} . \tag{A2}
$$

For the case $\nu_{\rm m}^{\rm syn} \le \nu_{\rm a,2}^{\rm syn} \le \nu_{\rm c}^{\rm syn}$, the SSC break frequencies are

$$
h\nu_{\rm ma,2}^{\rm ssc} = \nu_{\rm ma,2}^{\rm ssc,0}\, g(p)^{\frac{2(2p+3)}{p+4}} \left(\frac{1+z}{1.022}\right)^{\frac{(k-2)(p+6)}{2(p+4)}} \epsilon_{\rm e,-1}^{\frac{2(2p+3)}{p+4}}\, \epsilon_{\rm B,-2}^{\frac{p+2}{2(p+4)}} A_{\rm k}^{\frac{p+6}{2(p+4)}} \beta_{-0.5}^{\frac{18p-kp-6k+32}{2(p+4)}} t_6^{\frac{4-kp-6k}{2(p+4)}}
$$
$$
h\nu_{\rm mc,2}^{\rm ssc} = \nu_{\rm mc,2}^{\rm ssc,0}\, g^2(p) \left(\frac{1+z}{1.022}\right)^{\frac{2-3k}{2}} (1+Y)^{-2}\, \epsilon_{\rm e,-1}^2\, \epsilon_{\rm B,-2}^{-\frac{3}{2}} A_{\rm k}^{-\frac{3}{2}} \beta_{-0.5}^{\frac{3k+2}{2}} t_6^{\frac{3k-4}{2}}
$$
$$
h\nu_{\rm ca,2}^{\rm ssc} = \nu_{\rm ca,2}^{\rm ssc,0}\, g(p)^{\frac{2(p-1)}{p+4}} \left(\frac{1+z}{1.022}\right)^{\frac{4-10k+2p-3kp}{2(p+4)}} (1+Y)^{-2}\, \epsilon_{\rm e,-1}^{\frac{2(p-1)}{p+4}}\, \epsilon_{\rm B,-2}^{-\frac{3p+14}{2(p+4)}} A_{\rm k}^{-\frac{3p+10}{2(p+4)}} \beta_{-0.5}^{\frac{3kp+10k+2p-32}{2(p+4)}} t_6^{\frac{10k-4p+3kp-12}{2(p+4)}} , \tag{A3}
$$

and for $\nu_{\rm a,3}^{\rm syn} \le \nu_{\rm c}^{\rm syn} \le \nu_{\rm m}^{\rm syn}$, they are

$$
h\nu_{\rm ca,3}^{\rm ssc} = \nu_{\rm ca,3}^{\rm ssc,0} \left(\frac{1+z}{1.022}\right)^{-\frac{k+3}{5}} (1+Y)^{-1}\, \epsilon_{\rm B,-2}^{-\frac{4}{5}} A_{\rm k}^{-\frac{1}{5}} \beta_{-0.5}^{\frac{k-5}{5}} t_6^{\frac{k-2}{5}}
$$
$$
h\nu_{\rm cm,3}^{\rm ssc} = \nu_{\rm cm,3}^{\rm ssc,0}\, g^2(p) \left(\frac{1+z}{1.022}\right)^{\frac{2-3k}{2}} (1+Y)^{-2}\, \epsilon_{\rm e,-1}^2\, \epsilon_{\rm B,-2}^{-\frac{3}{2}} A_{\rm k}^{-\frac{3}{2}} \beta_{-0.5}^{\frac{3k+2}{2}} t_6^{\frac{3k-4}{2}} . \tag{A4}
$$

The spectral peak flux density of SSC emission $F_{\rm max}^{\rm ssc} \sim \frac{4}{3} g(p)^{-1} \sigma_T A_{\rm k} r^{1-k} F_{\rm max}^{\rm syn}$, with σ_T the Thomson cross section is given by

$$
F_{\nu,\rm max}^{\rm ssc} = F_{\nu,\rm max}^{\rm ssc,0}\, g(p)^{-1} \left(\frac{1+z}{1.022}\right)^{\frac{5k-6}{2}} \epsilon_{\rm B,-2}^{\frac{1}{2}} d_{\rm z,26.5}^{-2} A_{\rm k}^{\frac{5}{2}} \beta_{-0.5}^{\frac{5(2-k)}{2}} t_6^{\frac{8-5k}{2}} . \tag{A5}
$$

The terms of $\nu_{\rm mm}^{\rm ssc,0}$, $\nu_{\rm cc}^{\rm ssc,0}$, $\nu_{\rm ma,1}^{\rm ssc,0}$, $\nu_{\rm mc,1}^{\rm ssc,0}$, $\nu_{\rm ma,2}^{\rm ssc,0}$, $\nu_{\rm mc,2}^{\rm ssc,0}$, $\nu_{\rm ca,2}^{\rm ssc,0}$, $\nu_{\rm ma,3}^{\rm ssc,0}$, $\nu_{\rm mc,3}^{\rm ssc,0}$ and $F_{\nu,\rm max}^{\rm ssc,0}$ are given in Table 1 for k = 0, 1, 1.5, 2 and 2.5. Using the SSC break frequencies (eqs. A1, A2, A3 and A4) and the spectral peak flux density (eq. A5), the SSC light curves in the fast- and slow-cooling regime evolve as

$$
F_\nu^{\rm ssc} \propto \begin{cases}
t^{\frac{28-19k}{5}} \nu, & \nu < \nu_{\rm ca,3}^{\rm ssc}, \\
t^{\frac{16-11k}{3}} \nu^{\frac{1}{3}}, & \nu_{\rm ca,3}^{\rm ssc} < \nu < \nu_{\rm cc}^{\rm ssc}, \\
t^{\frac{8-3k}{4}} \left(C_{\rm cf,11} + C_{\rm cf,12} \ln\left[t^{\frac{8-7k}{2}}\nu\right]\right) \nu^{-\frac{1}{2}}, & \nu_{\rm cc}^{\rm ssc} < \nu < \nu_{\rm cm,3}^{\rm ssc}, \\
t^{\frac{8-3k}{4}} \left(C_{\rm cf,21} + C_{\rm cf,22} \ln\left[t^{-\frac{k}{2}}\nu^{-1}\right]\right) \nu^{-\frac{1}{2}}, & \nu_{\rm cm,3}^{\rm ssc} < \nu < \nu_{\rm mm}^{\rm ssc}, \\
t^{\frac{8-k(p+2)}{4}} \left(C_{\rm cf,31} + C_{\rm cf,32} \ln\left[t^{\frac{k}{2}}\nu\right]\right) \nu^{-\frac{p}{2}}, & \nu_{\rm mm}^{\rm ssc} < \nu,
\end{cases} \tag{A6}
$$

and

$$
F_\nu^{\rm ssc} \propto \begin{cases}
t^{-\frac{9(k-2)}{5}} \nu, & \nu < \nu_{\rm ma,1}^{\rm ssc}, \\
t^{\frac{12-7k}{3}} \nu^{\frac{1}{3}}, & \nu_{\rm ma,1}^{\rm ssc} < \nu < \nu_{\rm mm}^{\rm ssc}, \\
t^{\frac{16-9k-kp}{4}} \left(C_{\rm cs1,11} + C_{\rm cs1,12} \ln\left[t^{\frac{k}{2}}\nu\right]\right) \nu^{\frac{1-p}{2}}, & \nu_{\rm mm}^{\rm ssc} < \nu < \nu_{\rm mc,1}^{\rm ssc}, \\
t^{\frac{16-9k-kp}{4}} \left(C_{\rm cs1,21} + C_{\rm cs1,22} \ln\left[t^{\frac{7k-8}{2}}\nu^{-1}\right]\right) \nu^{\frac{1-p}{2}}, & \nu_{\rm mc,1}^{\rm ssc} < \nu < \nu_{\rm cc}^{\rm ssc}, \\
t^{\frac{8-2k-kp}{4}} \left(C_{\rm cs1,31} + C_{\rm cs1,32} \ln\left[t^{\frac{8-7k}{2}}\nu\right]\right) \nu^{-\frac{p}{2}}, & \nu_{\rm cc}^{\rm ssc} < \nu,
\end{cases} \tag{A7}
$$

$$F_\nu^{\rm ssc} \propto \begin{cases} t^{-\frac{3(k-2)(p+5)}{2(p+4)}} \nu, & \nu < \nu_{\rm ma,2}^{\rm ssc}, \\ t^{\frac{16-9k-kp}{4}} \left(C_{\rm cs2,11} + C_{\rm cs2,12} \ln\left[t^{\frac{k(p+6)-4}{2(p+4)}} \nu \right] \right) \nu^{\frac{1-p}{2}}, & \nu_{\rm ma,2}^{\rm ssc} < \nu < \nu_{\rm mc,2}^{\rm ssc}, \\ t^{\frac{16-9k-kp}{4}} \left(C_{\rm cs2,21} + C_{\rm cs2,22} \ln\left[t^{\frac{k(2p+9)-2(p+5)}{p+4}} \right] \right) \nu^{\frac{1-p}{2}}, & \nu_{\rm mc,2}^{\rm ssc} < \nu < \nu_{\rm ca,2}^{\rm ssc}, \\ t^{\frac{16-9k-kp}{4}} \left(C_{\rm cs2,31} + C_{\rm cs2,32} \ln\left[t^{\frac{7k-8}{2}} \nu^{-1} \right] \right) \nu^{\frac{1-p}{2}}, & \nu_{\rm ca,2}^{\rm ssc} < \nu < \nu_{\rm cc}^{\rm ssc}, \\ t^{\frac{8-2k-kp}{4}} \left(C_{\rm cs2,41} + C_{\rm cs2,42} \ln\left[t^{\frac{8-7k}{2}} \nu \right] \right) \nu^{-\frac{p}{2}}, & \nu_{\rm cc}^{\rm ssc} < \nu, \end{cases} \qquad (A8)$$

respectively. The parameters $C_{\rm cf}$, $C_{\rm cs,1}$ and $C_{\rm cs,2}$ do not evolve with time.

The deceleration phase

The PL indices $m_{\rm ij}$ for i, j =1, 2 and 3 are $m_{11} = -\frac{55+8\alpha-k(21+4\alpha)}{5(\alpha+5-k)}$, $m_{12} = \frac{-2p(\alpha-10)+kp(\alpha-6)+6k(\alpha+4)-12(\alpha+5)}{2(p+4)(\alpha+5-k)}$, $m_{13} = \frac{k(16+9\alpha)-13\alpha-20}{5(\alpha+5-k)}$, $m_{21} = \frac{3\alpha-16k+30-4k\alpha}{5(\alpha+5-k)}$, $m_{22} = \frac{4\alpha-6k\alpha-\alpha kp+8kp-30p-16k+20}{2(p+4)(\alpha+5-k)}$ and $m_{23} = \frac{8\alpha-9k\alpha-11k-5}{5(\alpha+5-k)}$. The corresponding SSC break frequencies during the deceleration phase are given by

$$h\nu_{\rm mm}^{\rm ssc} = \nu_{\rm mm}^{\rm ssc,0} \left(\frac{1+z}{1.022} \right)^{\frac{44+k(\alpha-14)-2\alpha}{2(\alpha+5-k)}} g(p)^4 \epsilon_{\rm e,-1}^4 \epsilon_{\rm B,-2}^{\frac{1}{2}} A_{\rm k}^{\frac{\alpha-13}{2(\alpha+5-k)}} \tilde{E}_{51}^{\frac{18-k}{2(\alpha+5-k)}} t_7^{-\frac{54+k(\alpha-16)}{2(\alpha+5-k)}}$$

$$h\nu_{\rm cc}^{\rm ssc} = \nu_{\rm cc}^{\rm ssc,0} \left(\frac{1+z}{1.022} \right)^{\frac{6\alpha-7k\alpha-6k-12}{2(\alpha+5-k)}} \epsilon_{\rm B,-2}^{-\frac{7}{2}} (1+Y)^{-4} A_{\rm k}^{-\frac{7(\alpha+3)}{2(\alpha+5-k)}} \tilde{E}_{51}^{\frac{7(k-2)}{2(\alpha+5-k)}} t_7^{\frac{2+8k-8\alpha+7k\alpha}{2(\alpha+5-k)}} \qquad (A9)$$

For the case $\nu_{\rm a,1}^{\rm syn} \leq \nu_{\rm m}^{\rm syn} \leq \nu_{\rm c}^{\rm syn}$, the SSC break frequencies are

$$h\nu_{\rm ma,1}^{\rm ssc} = \nu_{\rm ma,1}^{\rm ssc,0} g(p) \left(\frac{1+z}{1.022} \right)^{\frac{5+k-8\alpha+4k\alpha}{5(\alpha+5-k)}} \epsilon_{\rm e,-1} \epsilon_{\rm B,-2}^{\frac{1}{5}} A_{\rm k}^{\frac{4\alpha+5}{5(\alpha+5-k)}} \tilde{E}_{51}^{\frac{15-4k}{5(\alpha+5-k)}} t_7^{\frac{3\alpha-30+4k(1-\alpha)}{5(\alpha+5-k)}}$$

$$h\nu_{\rm mc,1}^{\rm ssc} = \nu_{\rm mc,1}^{\rm ssc,0} g^2(p) \left(\frac{1+z}{1.022} \right)^{\frac{16-10k+2\alpha-3k\alpha}{2(\alpha+5-k)}} (1+Y)^{-2} \epsilon_{\rm e,-1}^2 \epsilon_{\rm B,-2}^{-\frac{3}{2}} A_{\rm k}^{-\frac{3\alpha+17}{2(\alpha+5-k)}} \tilde{E}_{51}^{\frac{3k+2}{2(\alpha+5-k)}} t_7^{-\frac{26+4\alpha-3k(\alpha+4)}{2(\alpha+5-k)}} \qquad (A10)$$

For the case $\nu_{\rm m}^{\rm syn} \leq \nu_{\rm a,2}^{\rm syn} \leq \nu_{\rm c}^{\rm syn}$, the SSC break frequencies are

$$h\nu_{\rm ma,2}^{\rm ssc} = \nu_{\rm ma,2}^{\rm ssc,0} g(p)^{\frac{2(2p+3)}{p+4}} \left(\frac{1+z}{1.022} \right)^{\frac{36+44p-12\alpha-2p\alpha+k(6\alpha-8+p(\alpha-14))}{2(p+4)(\alpha+5-k)}} \epsilon_{\rm e,-1}^{\frac{2(2p+3)}{p+4}} \epsilon_{\rm B,-2}^{\frac{p+2}{2(p+4)}} A_{\rm k}^{\frac{6\alpha-2+p(\alpha-13)}{2(p+4)(\alpha+5-k)}}$$

$$\times \tilde{E}_{51}^{-\frac{k(p+6)-2(9p+16)}{2(p+4)(\alpha+5-k)}} t_7^{-\frac{76+54p-4\alpha+k(6\alpha-16+p(\alpha-16))}{2(p+4)(\alpha+5-k)}}$$

$$h\nu_{\rm mc,2}^{\rm ssc} = \nu_{\rm mc,2}^{\rm ssc,0} g^2(p) \left(\frac{1+z}{1.022} \right)^{\frac{16-10k+2\alpha-3k\alpha}{2(\alpha+5-k)}} (1+Y)^{-2} \epsilon_{\rm e,-1}^2 \epsilon_{\rm B,-2}^{-\frac{3}{2}} A_{\rm k}^{-\frac{17+3\alpha}{2(\alpha+5-k)}} \tilde{E}_{51}^{\frac{3k+2}{2(\alpha+5-k)}} t_7^{-\frac{26+4\alpha-3k(\alpha+4)}{2(\alpha+5-k)}}$$

$$h\nu_{\rm ca,2}^{\rm ssc} = \nu_{\rm ca,2}^{\rm ssc,0} g(p)^{\frac{2(p-1)}{p+4}} \left(\frac{1+z}{1.022} \right)^{\frac{2(2(\alpha-19)+p(\alpha+8))-k(10\alpha-8+p(3\alpha+10))}{2(p+4)(\alpha+5-k)}} (1+Y)^{-2} \epsilon_{\rm e,-1}^{\frac{2(p-1)}{p+4}} \epsilon_{\rm B,-2}^{-\frac{3p+14}{2(p+4)}} A_{\rm k}^{-\frac{18+17p+10\alpha+3p\alpha}{2(p+4)(\alpha+5-k)}}$$

$$\times \tilde{E}_{51}^{\frac{10k-32+2p+3kp}{2(p+4)(\alpha+5-k)}} t_7^{\frac{36+2(5k-6)\alpha+p(3k(\alpha+4)-26)-4\alpha}{2(p+4)(\alpha+5-k)}} \qquad (A11)$$

and for $\nu_{\rm a,3}^{\rm syn} \leq \nu_{\rm c}^{\rm syn} \leq \nu_{\rm m}^{\rm syn}$, they are

$$h\nu_{\rm ca,3}^{\rm ssc} = \nu_{\rm ca,3}^{\rm ssc,0} \left(\frac{1+z}{1.022} \right)^{-\frac{k(\alpha-6)+3(\alpha+10)}{5(\alpha+5-k)}} (1+Y)^{-1} \epsilon_{\rm B,-2}^{\frac{4}{5}} A_{\rm k}^{-\frac{\alpha}{5(\alpha+5-k)}} \tilde{E}_{51}^{\frac{k-5}{5(\alpha+5-k)}} t_7^{\frac{5-k-2\alpha+k\alpha}{5(\alpha+5-k)}}$$

$$h\nu_{\rm cm,3}^{\rm ssc} = \nu_{\rm cm,3}^{\rm ssc,0} g^2(p) \left(\frac{1+z}{1.022} \right)^{\frac{16-10k+2\alpha-3k\alpha}{2(\alpha+5-k)}} (1+Y)^{-2} \epsilon_{\rm e,-1}^2 \epsilon_{\rm B,-2}^{-\frac{3}{2}} A_{\rm k}^{-\frac{3\alpha+17}{2(\alpha+5-k)}} \tilde{E}_{51}^{\frac{3k+2}{2(\alpha+5-k)}} t_7^{\frac{3k(\alpha+4)-26-4\alpha}{2(\alpha+5-k)}} \qquad (A12)$$

The terms of $\nu_{\rm mm}^{\rm ssc,0}$, $\nu_{\rm cc}^{\rm ssc,0}$, $\nu_{\rm ma,1}^{\rm ssc,0}$, $\nu_{\rm mc,1}^{\rm ssc,0}$, $\nu_{\rm ma,2}^{\rm ssc,0}$, $\nu_{\rm mc,2}^{\rm ssc,0}$, $\nu_{\rm ca,2}^{\rm ssc,0}$, $\nu_{\rm ma,3}^{\rm ssc,0}$, $\nu_{\rm mc,3}^{\rm ssc,0}$ and $F_{\nu,\max}^{\rm ssc,0}$ are given in Table 1 for k = 0, 1, 1.5, 2 and 2.5. The spectral peak flux density of SSC emission

$$F_{\nu,\max}^{\rm ssc} = F_{\nu,\max}^{\rm ssc,0} g(p)^{-1} \left(\frac{1+z}{1.022} \right)^{\frac{6k-6\alpha+5k\alpha}{2(\alpha+5-k)}} \epsilon_{\rm B,-2}^{\frac{1}{2}} d_{z,26.5}^{-2} A_{\rm k}^{\frac{5(\alpha+3)}{2(\alpha+5-k)}} \tilde{E}_{51}^{\frac{5(2-k)}{2(\alpha+5-k)}} t_7^{\frac{10-8k+8\alpha-5k\alpha}{2(\alpha+5-k)}} . \qquad (A13)$$

Using the SSC break frequencies (eqs. A9, A10, A11 and A12) and the spectral peak flux density (eq. A13), the SSC light curves in the fast- and slow-cooling regime are

$$
F_\nu^{\rm ssc} \propto \begin{cases}
t^{\frac{20-26k+28\alpha-19k\alpha}{5(\alpha+5-k)}}\,\nu, & \nu < \nu_{\rm ca,3}^{\rm ssc}, \\[2mm]
t^{\frac{14-16k+16\alpha-11k\alpha}{3(\alpha+5-k)}}\,\nu^{\frac{1}{3}}, & \nu_{\rm ca,3}^{\rm ssc} < \nu < \nu_{\rm cc}^{\rm ssc}, \\[2mm]
t^{\frac{22-8k+8\alpha-3k\alpha}{4(\alpha+5-k)}}\left(C_{\rm df,11}+C_{\rm df,12}\ln\left[t^{\frac{8\alpha-2-k(8+7\alpha)}{2(\alpha+5-k)}}\,\nu\right]\right)\nu^{-\frac{1}{2}}, & \nu_{\rm cc}^{\rm ssc} < \nu < \nu_{\rm cm,3}^{\rm ssc}, \\[2mm]
t^{\frac{22-8k+8\alpha-3k\alpha}{4(\alpha+5-k)}}\left(C_{\rm df,21}+C_{\rm df,22}\ln\left[t^{-\frac{54+k(\alpha-16)}{2(\alpha+5-k)}}\,\nu^{-1}\right]\right)\nu^{-\frac{1}{2}}, & \nu_{\rm cm,3}^{\rm ssc} < \nu < \nu_{\rm mm}^{\rm ssc}, \\[2mm]
t^{\frac{76-54p-kp(\alpha-16)+8\alpha-2k(\alpha+12)}{4(\alpha+5-k)}}\left(C_{\rm df,31}+C_{\rm df,32}\ln\left[t^{\frac{54+k(\alpha-16)}{2(\alpha+5-k)}}\,\nu\right]\right)\nu^{-\frac{p}{2}}, & \nu_{\rm mm}^{\rm ssc} < \nu,
\end{cases}
\tag{A14}
$$

$$
F_\nu^{\rm ssc} \propto \begin{cases}
t^{\frac{9(2(\alpha+5)-k(\alpha+4))}{5(\alpha+5-k)}}\,\nu, & \nu < \nu_{\rm ma,1}^{\rm ssc}, \\[2mm]
t^{\frac{42-20k+12\alpha-7k\alpha}{3(\alpha+5-k)}}\,\nu^{\frac{1}{3}}, & \nu_{\rm ma,1}^{\rm ssc} < \nu < \nu_{\rm mm}^{\rm ssc}, \\[2mm]
t^{\frac{74-54p+16\alpha-k(32+p(\alpha-16)+9\alpha)}{4(\alpha+5-k)}}\left(C_{\rm ds1,11}+C_{\rm ds1,12}\ln\left[t^{\frac{54+k(\alpha-16)}{2(\alpha+5-k)}}\,\nu\right]\right)\nu^{\frac{1-p}{2}}, & \nu_{\rm mm}^{\rm ssc} < \nu < \nu_{\rm mc,1}^{\rm ssc}, \\[2mm]
t^{\frac{74-54p+16\alpha-k(32+p(\alpha-16)+9\alpha)}{4(\alpha+5-k)}}\left(C_{\rm ds1,21}+C_{\rm ds1,22}\ln\left[t^{\frac{2+8k-8\alpha+7k\alpha}{2(\alpha+5-k)}}\,\nu^{-1}\right]\right)\nu^{\frac{1-p}{2}}, & \nu_{\rm mc,1}^{\rm ssc} < \nu < \nu_{\rm cc}^{\rm ssc}, \\[2mm]
t^{\frac{76-54p-kp(\alpha-16)+8\alpha-2k(\alpha+12)}{4(\alpha+5-k)}}\left(C_{\rm ds1,31}+C_{\rm ds1,32}\ln\left[t^{\frac{8\alpha-2-k(7\alpha+8)}{2(\alpha+5-k)}}\,\nu\right]\right)\nu^{-\frac{p}{2}}, & \nu_{\rm cc}^{\rm ssc} < \nu,
\end{cases}
\tag{A15}
$$

and

$$
F_\nu^{\rm ssc} \propto \begin{cases}
t^{\frac{6(31+p(\alpha-1)+5\alpha)-3k(24+\alpha(p+5))}{2(p+4)(\alpha+5-k)}}\,\nu, & \nu < \nu_{\rm ma,2}^{\rm ssc}, \\[2mm]
t^{\frac{74-54p+16\alpha-k(32+p(\alpha-16)+9\alpha)}{4(\alpha+5-k)}}\left(C_{\rm ds2,11}+C_{\rm ds2,12}\ln\left[t^{\frac{76+54p-4\alpha+k(6\alpha-16+p(\alpha-16))}{2(p+4)(\alpha+5-k)}}\,\nu\right]\right)\nu^{\frac{1-p}{2}}, & \nu_{\rm ma,2}^{\rm ssc} < \nu < \nu_{\rm mc,2}^{\rm ssc}, \\[2mm]
t^{\frac{74-54p+16\alpha-k(32+p(\alpha-16)+9\alpha)}{4(\alpha+5-k)}}\left(C_{\rm ds2,21}+C_{\rm ds2,22}\ln\left[t^{\frac{k(16+2p(\alpha-1)+9\alpha)-2(7+p(\alpha-7)+5\alpha)}{(p+4)(\alpha+5-k)}}\,\nu\right]\right)\nu^{\frac{1-p}{2}}, & \nu_{\rm mc,2}^{\rm ssc} < \nu < \nu_{\rm ca,2}^{\rm ssc}, \\[2mm]
t^{\frac{74-54p+16\alpha-k(32+p(\alpha-16)+9\alpha)}{4(\alpha+5-k)}}\left(C_{\rm ds2,31}+C_{\rm ds2,32}\ln\left[t^{\frac{2+8k-8\alpha+7k\alpha}{2(\alpha+5-k)}}\,\nu^{-1}\right]\right)\nu^{\frac{1-p}{2}}, & \nu_{\rm ca,2}^{\rm ssc} < \nu < \nu_{\rm cc}^{\rm ssc}, \\[2mm]
t^{\frac{76-54p-kp(\alpha-16)+8\alpha-2k(\alpha+12)}{4(\alpha+5-k)}}\left(C_{\rm ds2,41}+C_{\rm ds2,42}\ln\left[t^{\frac{8\alpha-2-k(7\alpha+8)}{2(\alpha+5-k)}}\,\nu\right]\right)\nu^{-\frac{p}{2}}, & \nu_{\rm cc}^{\rm ssc} < \nu,
\end{cases}
\tag{A16}
$$

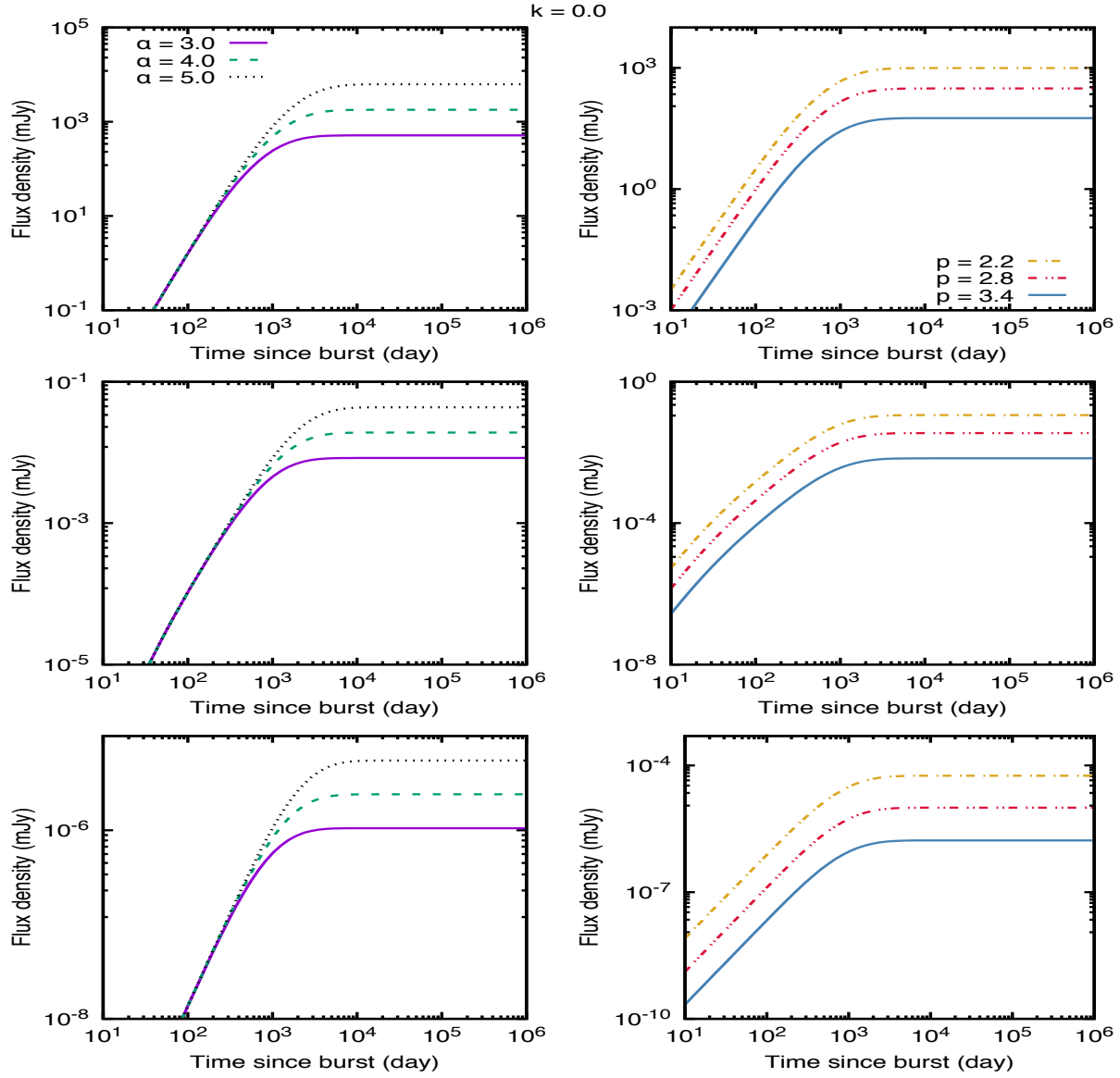respectively. The parameters $C_{\rm df}$, $C_{\rm ds,1}$ and $C_{\rm ds,2}$ do not evolve with time.

FIG. 1.— Synchrotron light curves generated by the deceleration of the non-relativistic ejecta for $k = 0$. Panels from top to bottom correspond to radio (1.6 GHz), optical (1 eV) and X-ray (1 keV) bands, respectively. The left-hand panels show the light curves for $p = 2.6$ with $\alpha = 3$, 4 and 5, and the right-hand panels show the light curves for $\alpha = 3$ with $p = 2.2$, 2.8 and 3.4. The following parameters $\tilde{E} = 10^{51}$ erg, $A_0 = 1\,\mathrm{cm}^{-3}$, $\epsilon_B = 10^{-2}$, $\epsilon_B = 10^{-1}$ and $d = 100\,\mathrm{Mpc}$ are used.
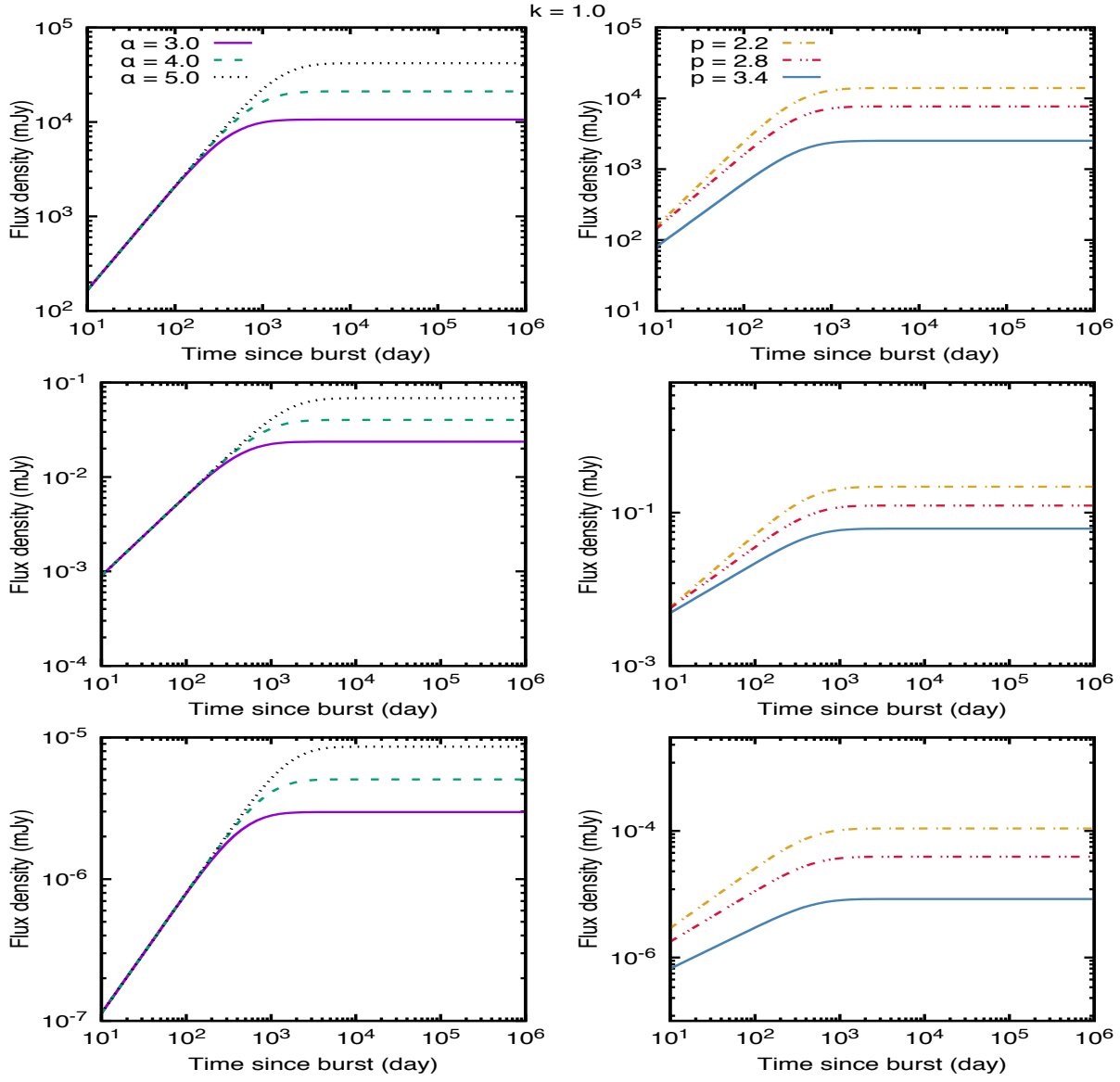
FIG. 2.— The same as Figure 1, but for $k = 1.0$ with $A_1 = 1.5 \times 10^{19}$ cm^{-2}.
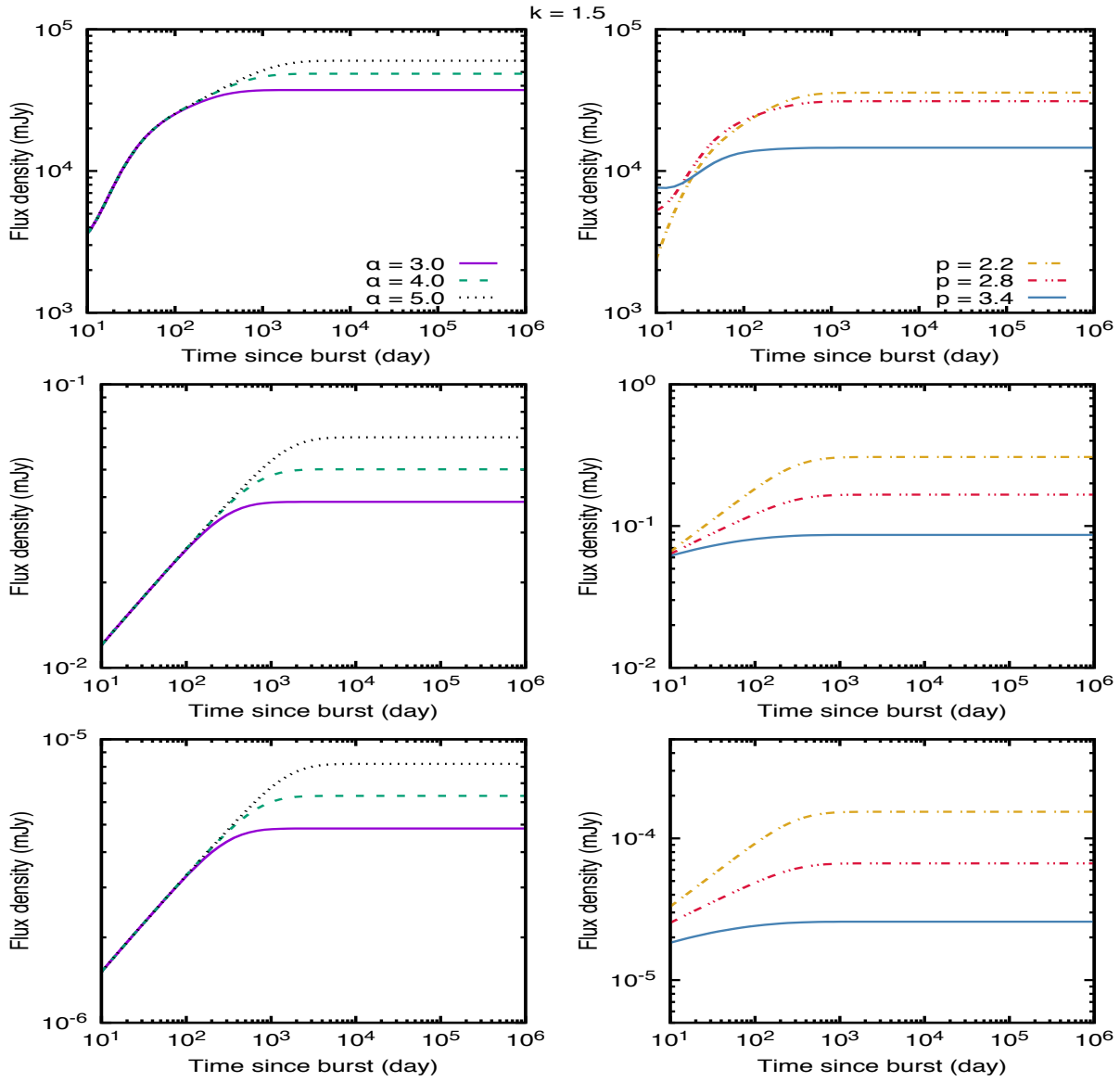
FIG. 3.— The same as Figure 1, but for $k = 1.5$ with $A_{1.5} = 2.7 \times 10^{28} \, \mathrm{cm}^{-\frac{3}{2}}$.
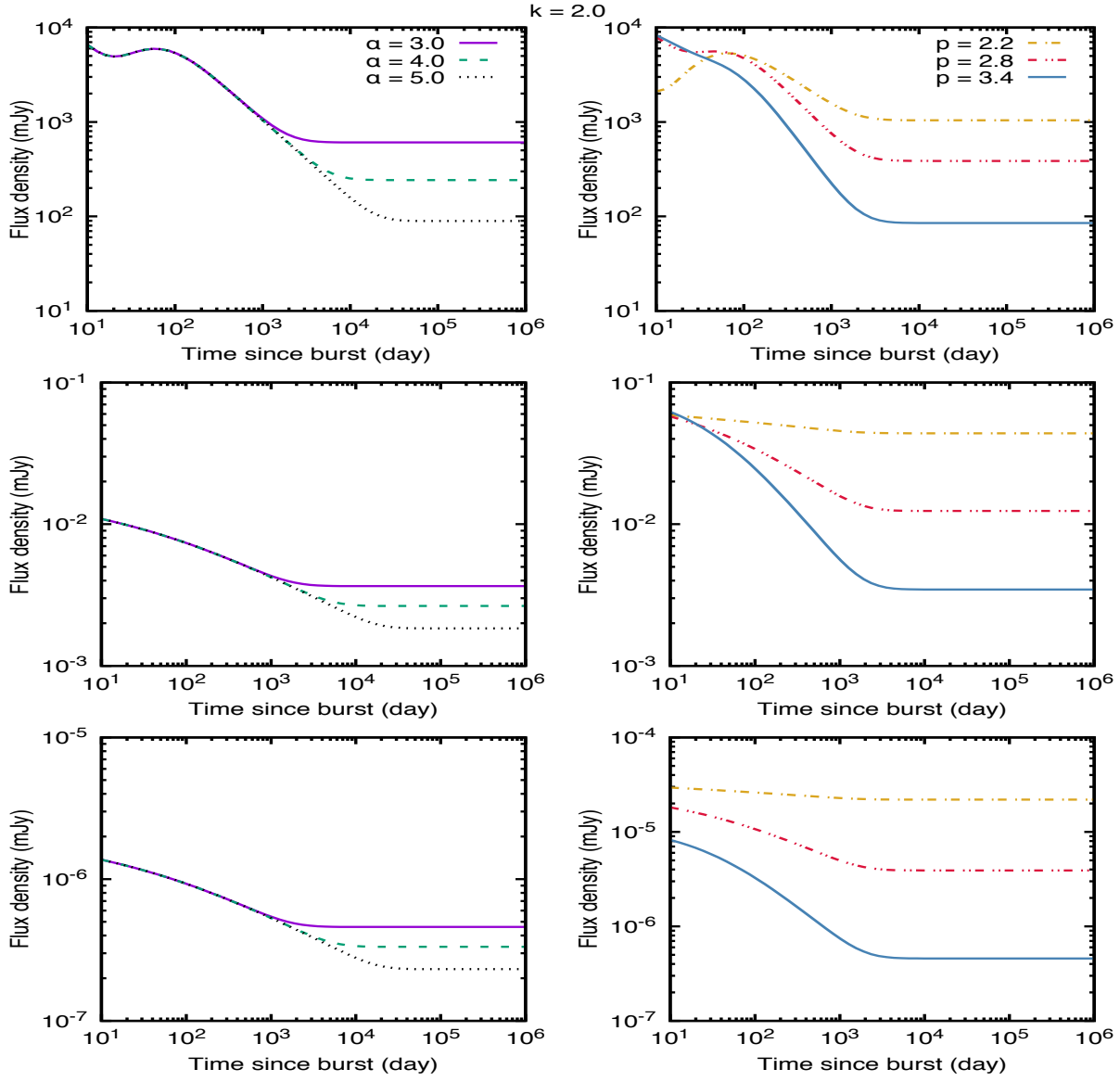
FIG. 4.— The same as Figure 1, but for $k = 2.0$ with $A_2 = 3 \times 10^{36}$ cm^{-1}.

24
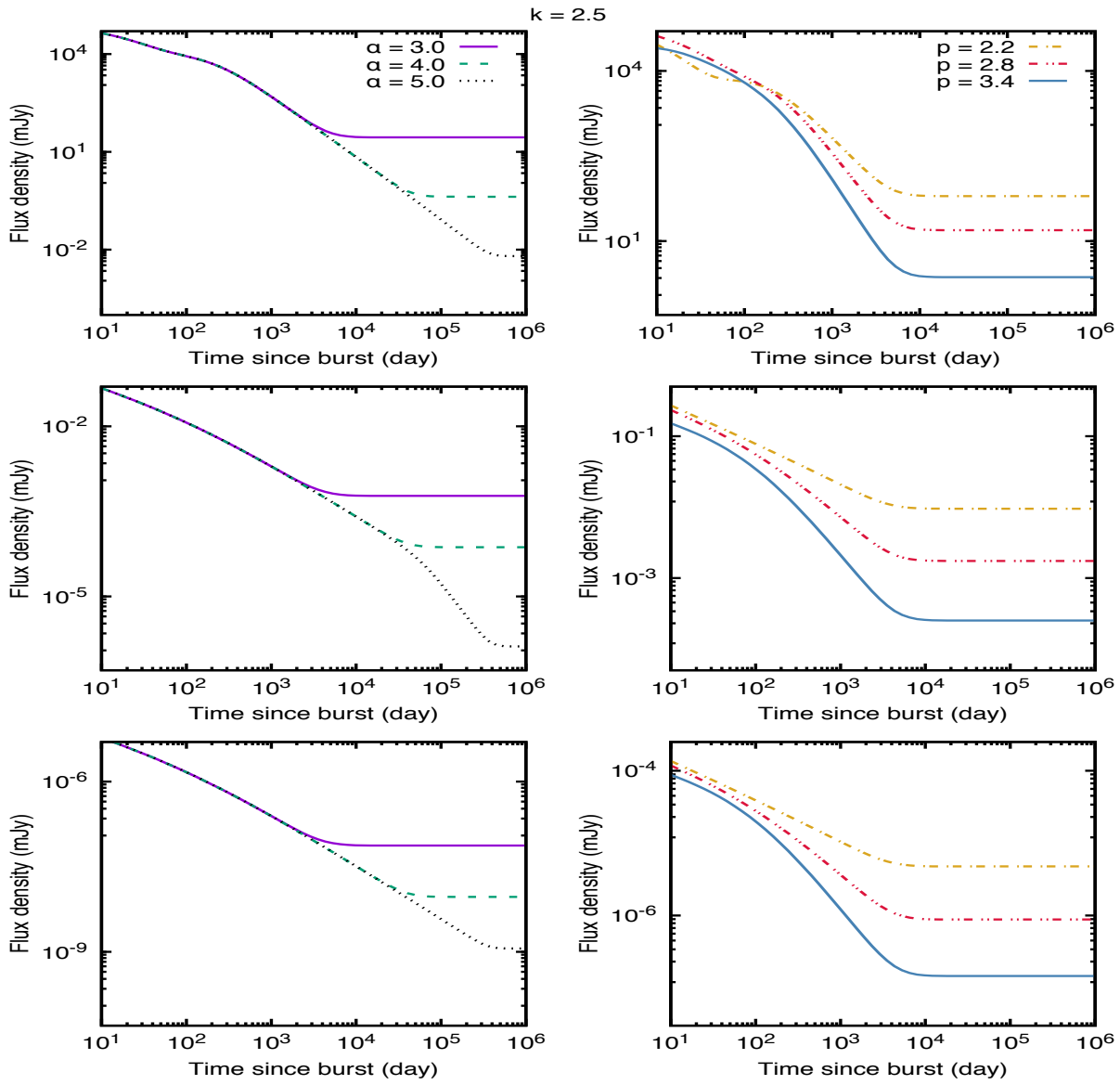
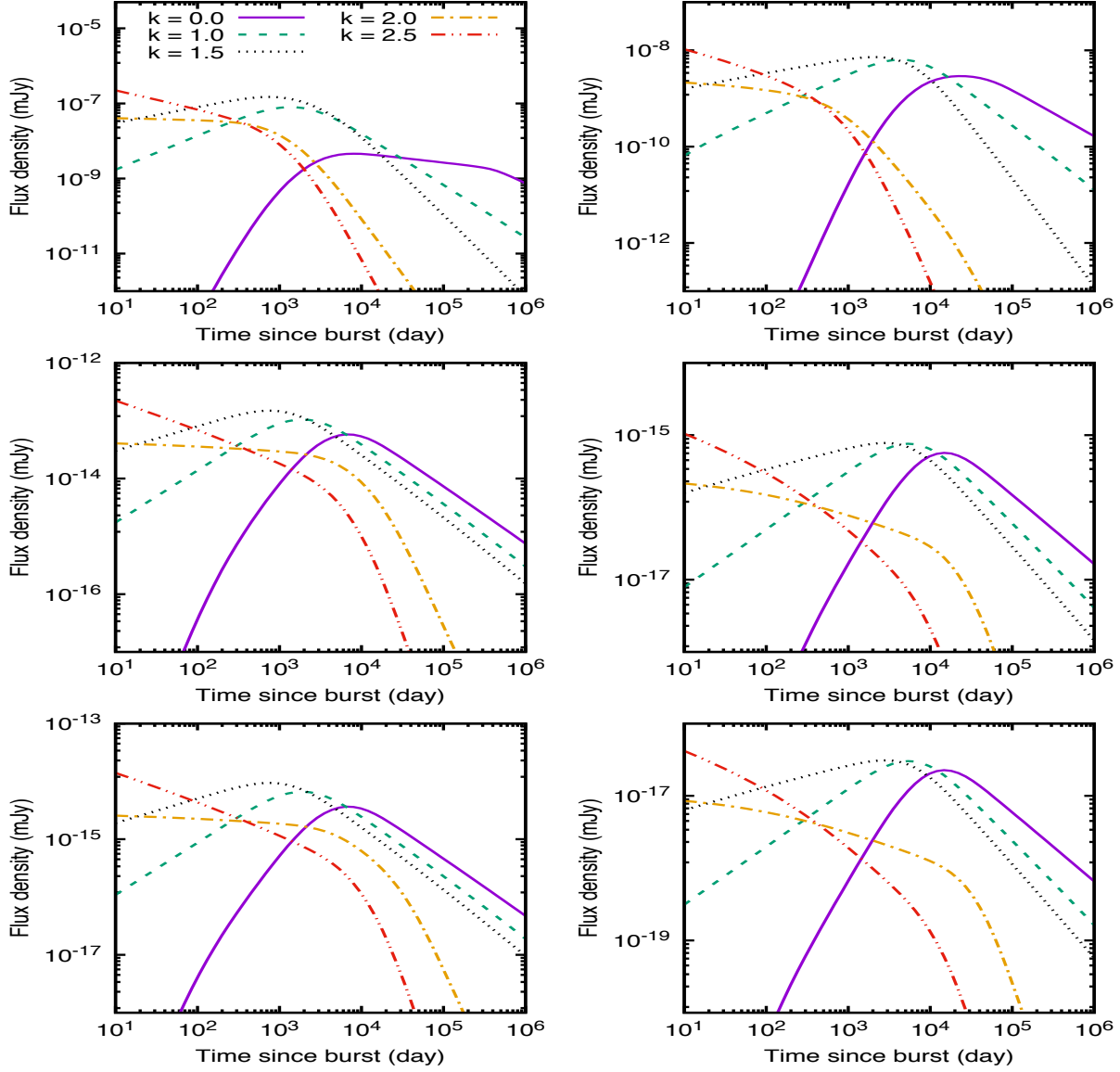FIG. 5.— The same as Figure 1, but for $k = 2.5$ with $A_{2.5} = 1.3 \times 10^{45}$ cm$^{-\frac{1}{2}}$.

FIG. 6.— SSC light curves generated by the deceleration of the non-relativistic ejecta for $k = 0$, 1, 1.5, 2 and 2.5. Panels from top to bottom correspond to gamma-ray fluxes at 100 keV, 10 GeV and 100 GeV, respectively. The left-hand panels show the light curves for $p = 2.4$ and $\alpha = 3.0$, and the right-hand panels for $p = 2.8$ and $\alpha = 5.0$. We use the same typical values that were used for the synchrotron light curves.
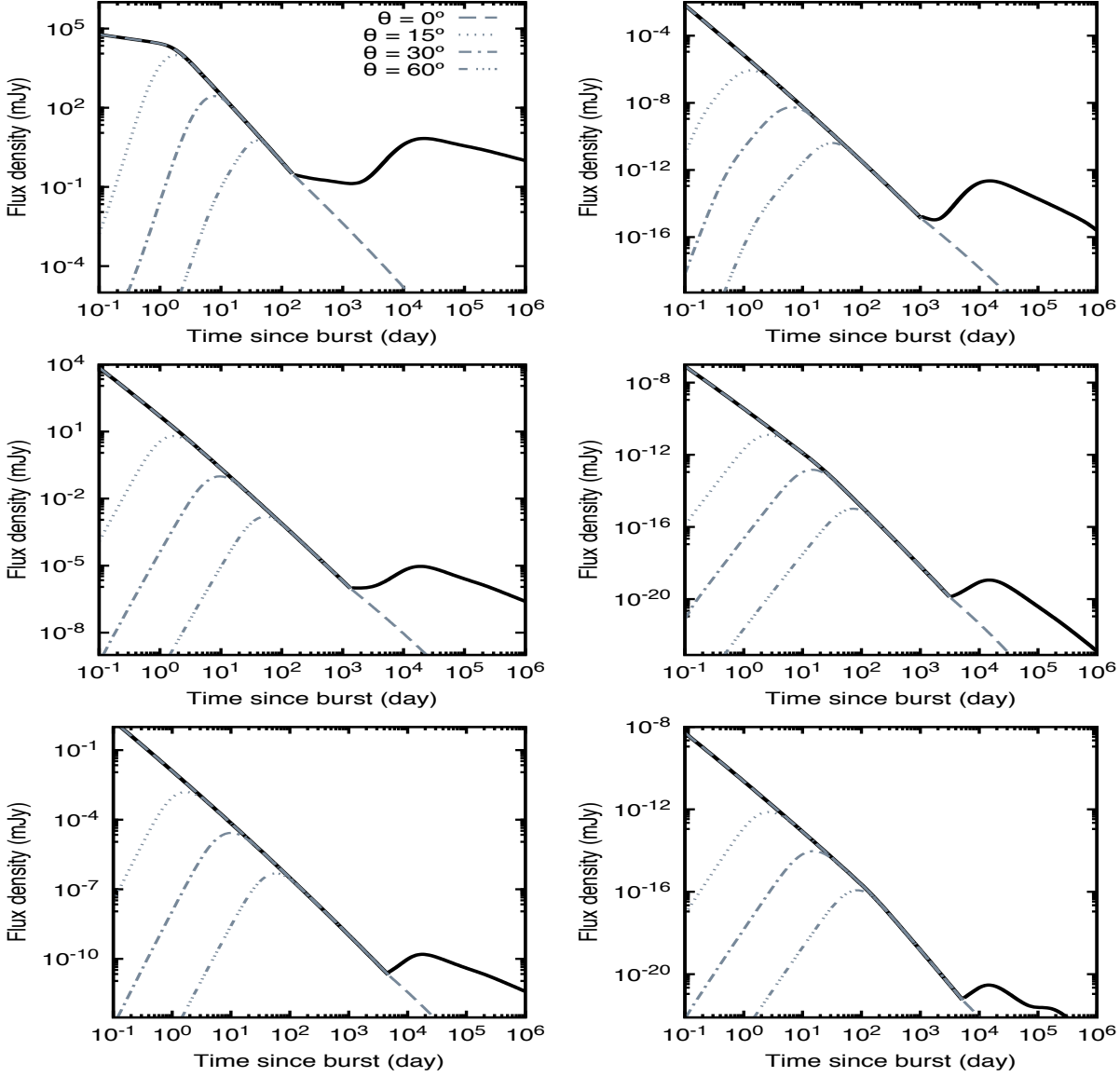
FIG. 7.— SSC and synchrotron light curves generated by the non-relativistic masses ejected from NS mergers such as the dynamical ejecta, the cocoon, the shock breakout and the wind. The left-hand panels show the synchrotron light curves which correspond to (from top to bottom) radio (1.6 GHz), optical (1 eV) and X-ray (1 keV) bands, respectively, and the right-hand panels show the SSC light curves which correspond to (from top to bottom) gamma-ray fluxes at 100 keV, 10 GeV and 100 GeV, respectively. The following parameters $A_0 = 1\,\mathrm{cm}^{-3}$, $p = 2.6$, $\alpha = 3.0$, $\epsilon_B = 10^{-1}$, $\epsilon_B = 10^{-1}$ and $d = 100\,\mathrm{Mpc}$ are used. The gray solid lines correspond to an on-axis and off-axis relativistic jet with viewing angles of $\theta = 15°$, $30°$ and $60°$. The black solid line represents the total contribution from the relativistic jet and the non-relativistic masses ejected from NS mergers. The expected fluxes from the relativistic jet are obtained in accordance with the afterglow model introduced in Fraija et al. (2019d).
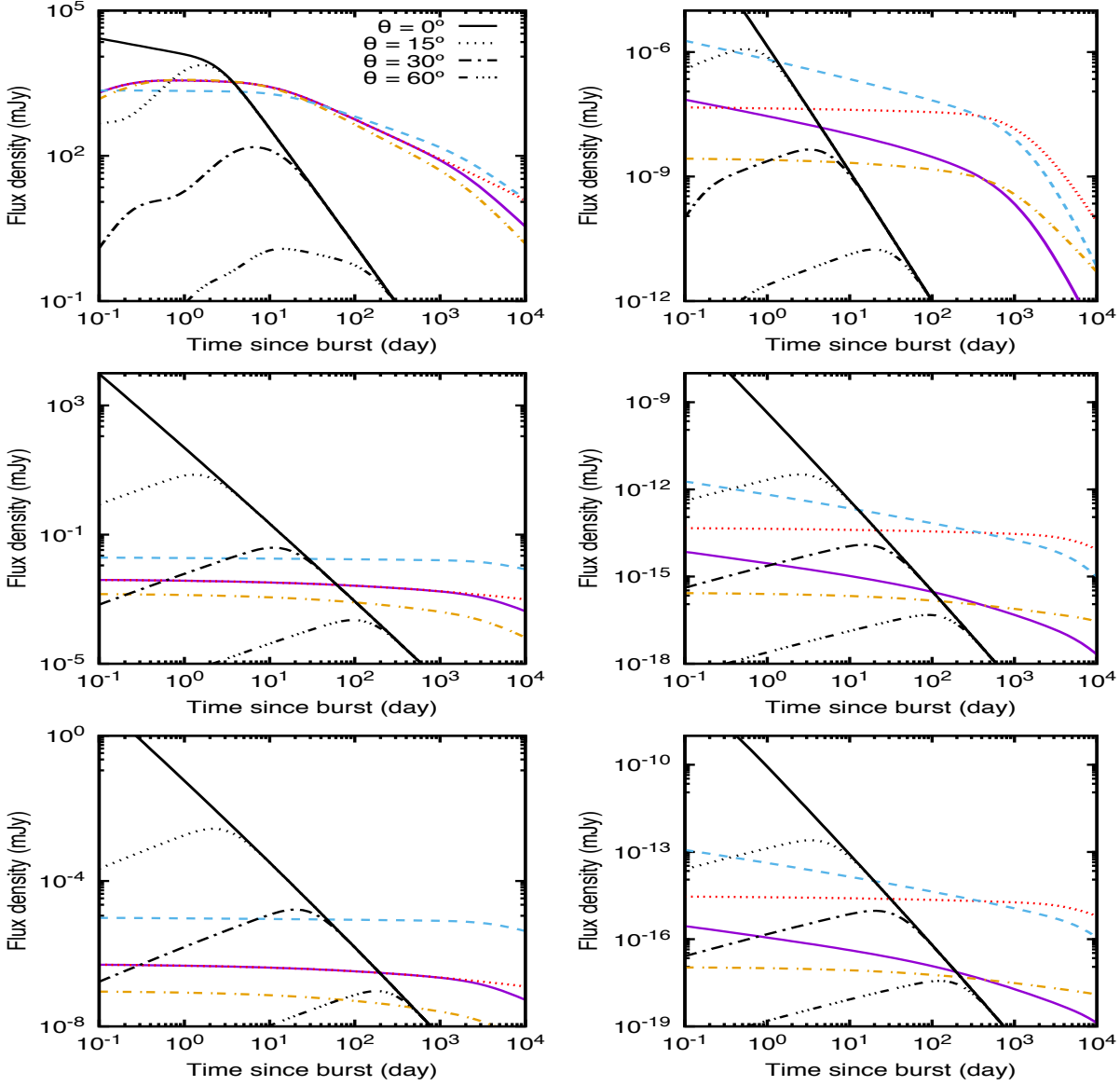
FIG. 8.— SSC and synchrotron light curves generated by the deceleration of non-relativistic masses ejected in a stellar wind medium. The left-hand panels show the synchrotron light curves which correspond to (from top to bottom) radio (1.6 GHz), optical (1 eV) and X-ray (1 keV) bands, respectively, and the right-hand panels show the SSC light curves which correspond to (from top to bottom) gamma-ray fluxes at 100 keV, 10 GeV and 100 GeV, respectively. The solid purple line is for $\alpha = 3$, $p = 2.6$, the dashed blue line is for $\alpha = 5$, $p = 2.6$, the dotted-dashed yellow line is for $\alpha = 3.5$, $p = 2.2$ and the dotted red line is for $\alpha = 3.5$, $p = 2.8$. The following parameters $\tilde{E} = 10^{51}$ erg, $A_2 = 3 \times 10^{36}$ cm^{-1}, $\epsilon_B = 10^{-2}$, $\epsilon_B = 10^{-1}$ and $d = 100$ Mpc are used.
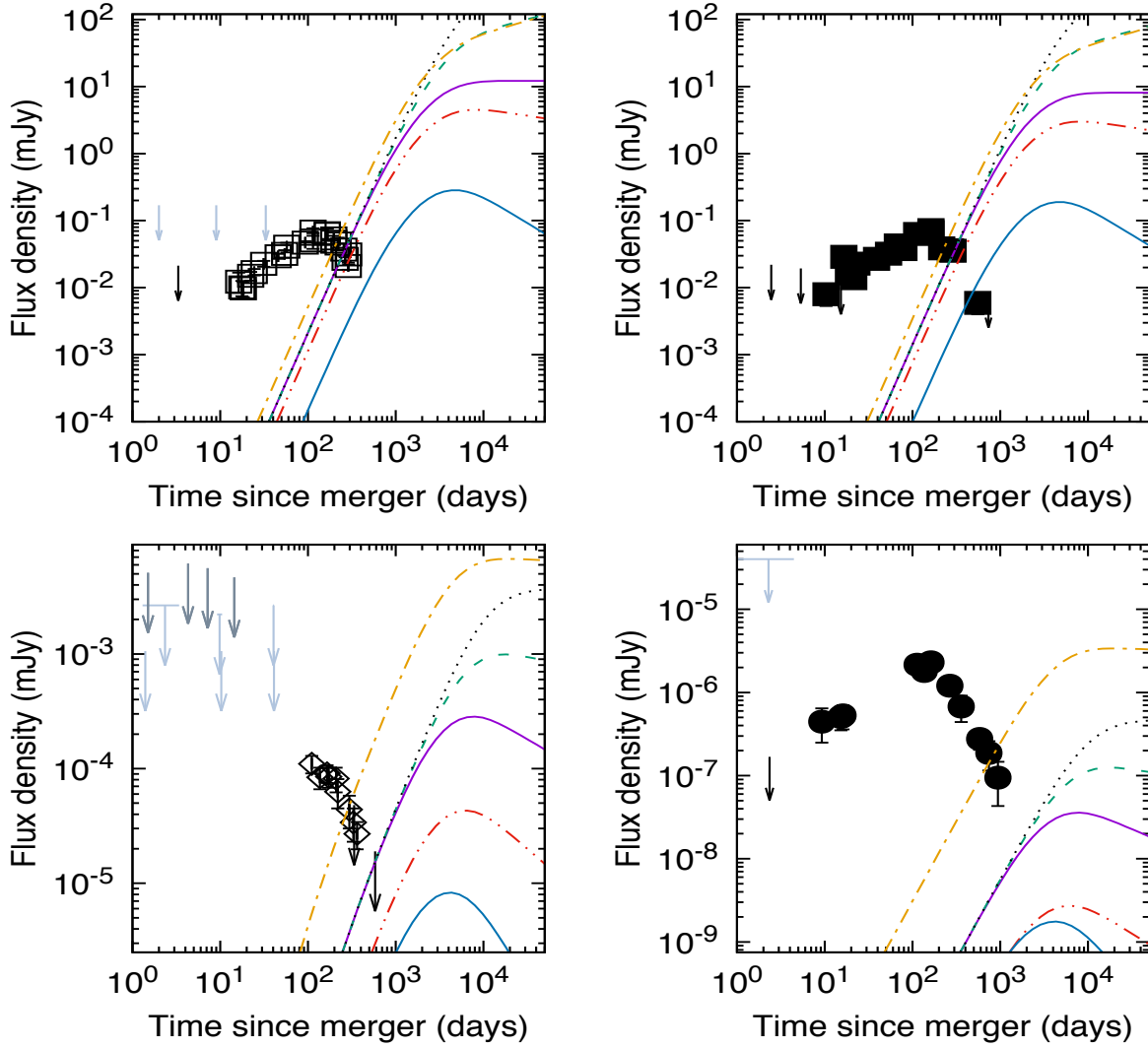
FIG. 9.— The multi-wavelength observations and upper limits of GRB 170817A and S190814bv at the radio, optical and X-ray bands with the synchrotron light curves generated by the deceleration of the non-relativistic ejecta for $k = 0$ (see Figure 1). The upper panels show the radio observations at 3 GHz (left) and 6 GHz (right), and the lower panels show the observations at the F606W filter (left) and 1 keV (right). The solid curves in blue for optical and X-ray are multiplied by 60 and 1.6×10^3, respectively, to be illustrated in each panel. The data points of GRB 170817A are taken from Fong et al. (2019); Fraija et al. (2019d); Hajela et al. (2019); Troja et al. (2020a), and upper limits of S190814bv are taken from Dobie et al. (2019); Ackley et al. (2020); Evans et al. (2019). The data conversion of the latest Chandra afterglow observations between $\mathrm{erg\,cm^{-2}\,s^{-1}}$ (0.3 - 10 keV) and mJy normalized at 1 keV is reported in Table 2.
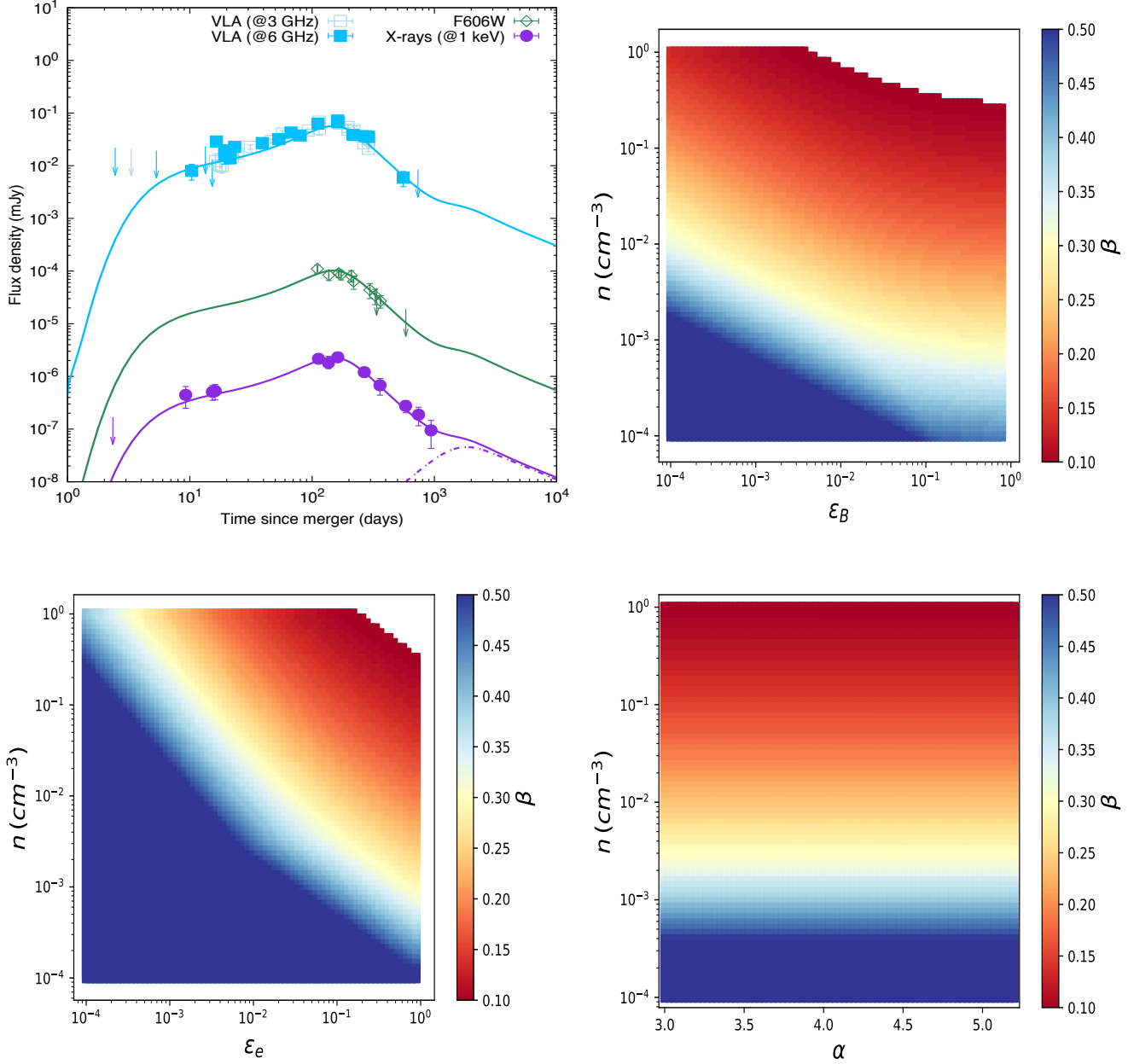
FIG. 10.— The upper left-hand panel shows the multi-wavelength data points of GRB 170817A with the best-fit curves obtained with the structure jet model presented in Fraija et al. (2019d) and a possible synchrotron light curve from the deceleration of the non-relativistic ejecta. The upper right-hand and lower panels show the allowed parameter space of the uniform density of the circumstellar medium (n), the velocity of the non-relativistic ejecta (β) and the microphysical parameter (ϵ_e and ϵ_B) for the fiducial energy $E = 10^{49}$ erg, $\alpha = 3.0$ and the spectral index $p = 2.15$. The value of the microphysical parameter $\epsilon_e = 10^{-1}$ is used in the left-hand panel, and $\epsilon_B = 10^{-3}$ in the right-hand panel.
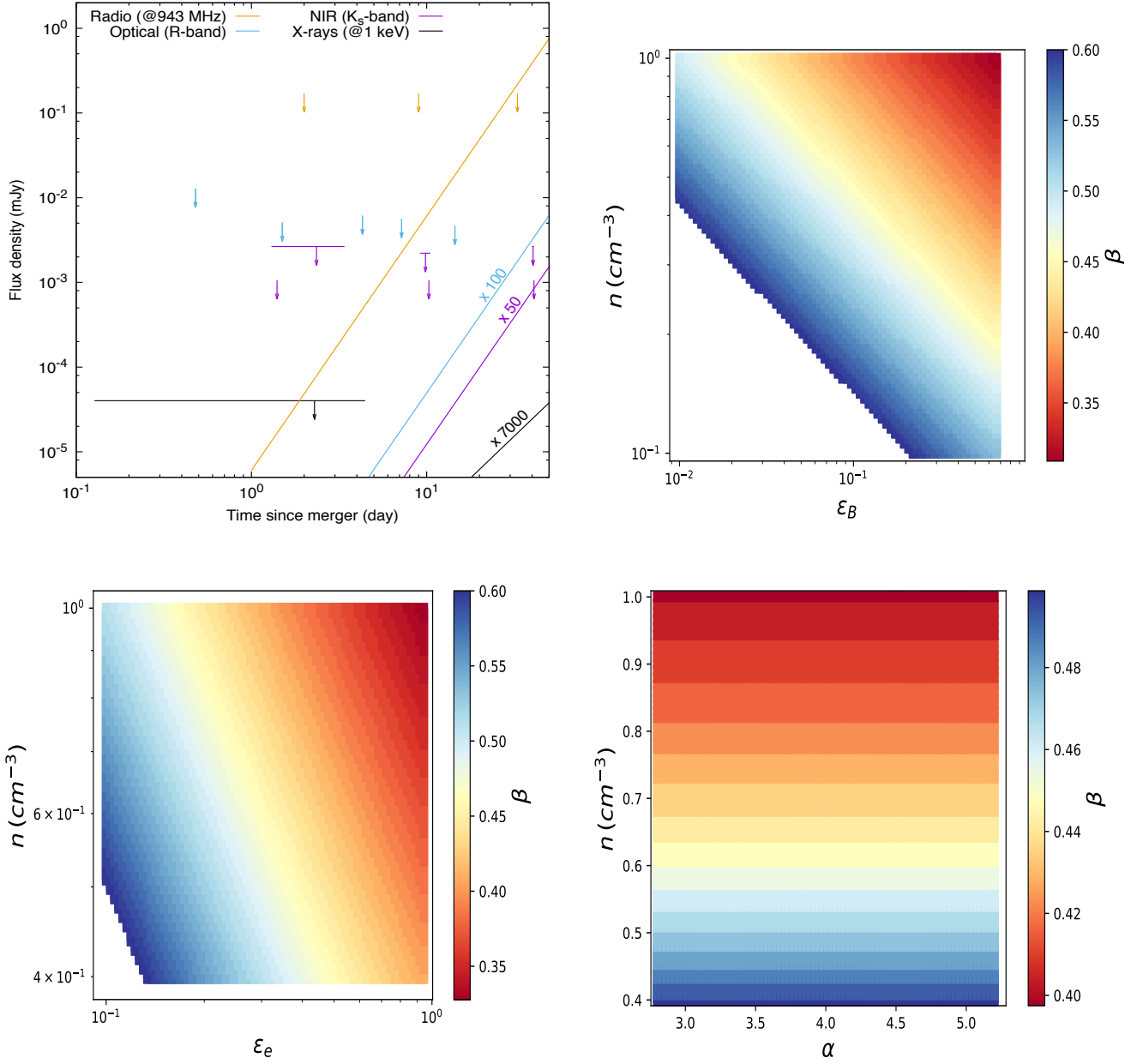
FIG. 11.— The upper left-hand panel shows the multi-wavelength upper limits of S190814bv and the parameter space ruled out with the synchrotron model presented in this work. The upper right-hand and lower panels show the parameter space of the uniform density of the circumstellar medium (n), the velocity of the non-relativistic ejecta (β) and the microphysical parameter (ϵ_e and ϵ_B) which is ruled out in our model for the fiducial energy $E = 10^{50}$ erg, $\alpha = 3.0$ and the spectral index $p = 2.6$. The value of the microphysical parameter $\epsilon_e = 10^{-1}$ is used in the left-hand panel, and $\epsilon_B = 10^{-2}$ in the right-hand panel.